Dissertation

submitted to the
Combined Faculties of the Natural Sciences and Mathematics
of the Ruperto-Carola-University of Heidelberg, Germany,
for the degree of
Doctor of Natural Sciences

Put forward by
Johannes Esser
born in Lippstadt, Germany

Oral examination: May 18th, 2020

PHYSICAL PROPERTIES OF THE CIRCUMNUCLEAR CLOUD DISTRIBUTION IN ACTIVE GALACTIC NUCLEI

Johannes Esser

Referees:	**Prof. Dr. Hans-Walter Rix**
	Prof. Dr. Jochen Heidt

Abstract

In this thesis the structure of the broad line region (BLR) and the inner dust torus of Active Galactic Nuclei (AGN) is studied. In a first project we have carried out a multiwavelength reverberation mapping campaign of hot dust in AGN for a sample of 25 nearby AGN with redshifts below 0.2. Reverberation mapping allows to measure the radius of the dust torus which, in relation to the accretion disk (AD) luminosity, can be used as a cosmological standard candle. Despite the radius the multiwavelength approach allows for the investigation of other dust properties like the temperature. An influence of dust temperatures on the relation between the dust radius and the AD luminosity is expected, as hotter dust should be located closer to the heating source at smaller radii. We were able to determine 14 reliable dust radii and 20 reliable dust temperatures for our AGN. This is the largest sample of homogeneously reverberation mapped inner dust tori using a multiwavelength approach and among the largest dust reverberation mapping samples overall. We got tighter constraints on the luminosity radius relation when a novel temperature normalization was applied. Especially the slope of the relation is only in good agreement with the expected value of 0.5 if the temperature normalization is taken into account. Additionally we can determine the surface area of the dust only when the temperature is known. We found that the radial extend of the dust torus behaves comparable to the delay with respect to luminosity.

In the second project we compare concurrent changes of the dust radius to shape variations of broad emission lines (BELs) for NGC 4151 observed from 2004 to 2006. These simultaneous changes are discussed in a variety of dust and BEL formation schemes. Furthermore we use the shape variations to assess possible (especially azimuthal) cloud distributions, which could be responsible for the observed variations. A dust inflated AD provides the framework best suited to explain our findings. The changes in the BELs suggest that this dusty cloud formation happens in spatially confined areas on rather short timescales.

Zusammenfassung

In dieser Doktorarbeit werden wir die Struktur der Broad Line Region (BLR) und des Staubtorus untersuchen. Zunächst haben wir ein Reverberation Mapping Projekt für 25 nahe Aktive Galaktische Kerne (AGN) mit Rotverschiebungen unter 0.2 durchgeführt. Dabei wurden im Vergleich zu ähnlichen Projekten mehr als zwei Breitbandfilter verwendet. Reverberation Mapping erlaubt es den Radius des Staubtorus zu bestimmen, der in Relation zur Leuchtkraft der Akkretionsscheibe als kosmologische Standardkerze verwendet werden kann. Abgesehen vom Radius erlaubt uns die Verwendung von mehreren Breitbandfiltern die Bestimmung weiterer Staubparameter, wie beispielsweise die Temperatur. Ein Einfluss der Staubtemperaturen auf die Relation zwischen Staubradius und Leuchtkraft der Akkretionsscheibe wird erwartet, da wärmerer Staub näher an der Heizquelle und damit bei kleineren Radien liegen sollte. Wir konnten 14 verlässliche Staubradien sowie 20 Staubtemperaturen für unsere AGN bestimmen. Damit ist dies die größte Stichprobe von Staubradien, die homogen unter Verwendung mehrerer Breitbandfilter bestimmt wurden. Auch innerhalb der allgemeinen Reverberation Mapping Programme ist dies eines der größeren. Die Einschränkungen für die Leuchtkraft Radius Relation waren deutlich enger unter Verwendung einer von uns entwickelten Normalisierung mit der Temperatur. Besonders die Steigung der Relation nimmt nur den erwarteten Wert von 0.5 an, wenn die Normalisierung mit der Temperatur durchgeführt wird. Darüber hinaus können wir die Stauboberfläche bestimmen und so zeigen, dass sich die radiale Ausdehnung des Staubtorus relativ zur Leuchtkraft der Akkretionsscheibe ähnlich verhält wie der Radius.

Im zweiten Projekt vergleichen wir die gleichzeitigen Änderungen des Staubradius und Veränderungen der Form der breiten Emissionslinien (BELs), die für NGC 4151 zwischen 2004 und 2006 beobachtet wurden. Diese simultanen Veränderungen werden innerhalb verschiedener Theorien zur Staub- und BEL-Entstehung diskutiert. Des Weiteren nutzen wir die Veränderungen der Form der BELs um mögliche Wolkenverteilungen, besonders in azimuthaler Richtung, zu finden, die die beobachteten Veränderungen erklären können. Eine durch Staubentstehung aufgeblähte Akkretionsscheibe ist das theoretische Gerüst, mit dem unsere Beobachtungen bestmöglich erklärt werden können. Die Veränderungen der BELs legen nahe, dass sich diese staubige Wolkenentstehung in räumlich begrenzten Bereichen und auf relativ kurzen Zeitskalen ereignet.

Für meine Familie.

Contents

List of Figures I

List of Tables III

1 Context and Theoretical Background 1

- 1.1 Typology of AGN 3
  - 1.1.1 Radio-quiet AGN 4
  - 1.1.2 Radio-loud AGN 4
- 1.2 AGN unification model 6
- 1.3 Dust in AGN 9
  - 1.3.1 The dust torus 10
  - 1.3.2 Polar dust 11
- 1.4 The Broad Line Region 12
- 1.5 The Accretion Disk 14
  - 1.5.1 The Eddington luminosity 14
  - 1.5.2 Thin accretion disks 15
  - 1.5.3 Thick accretion disks 16
- 1.6 The radius luminosity relation 18
  - 1.6.1 Using the radius luminosity relation as a standard candle 20
- 1.7 Formation of dust torus and BLR 23
  - 1.7.1 Dust production outside AGN 23
  - 1.7.2 Dusty outflow model 23
- 1.8 Structure of this thesis 26

2 Measuring structure sizes in AGN 27

- 2.1 Reverberation mapping 29
  - 2.1.1 Results for the BLR 32
  - 2.1.2 Results for the Dust torus 33
  - 2.1.3 Results for the Accretion Disk 34
- 2.2 Interferometry 35

  2.2.1 Results for the BLR 37
  2.2.2 Results for the dust torus 37
  2.2.3 Results for the Accretion Disk 37

3 Multiwavelength dust reverberation mapping 39
3.1 Introduction 41
3.2 Observations 42
3.3 Data reduction 45
3.4 Model for reverberation mapping 48
  3.4.1 Accretion disk and dust model 48
  3.4.2 Interpolation of the accretion disk signal 49
  3.4.3 Implementation of model 51
3.5 Reverberation mapping results 52
  3.5.1 Sample results 52
  3.5.2 Individual sources 61
  3.5.3 Comparison to results from interferometry 64
3.6 Discussion 66
  3.6.1 Radius luminosity relation 66
  3.6.2 Radiating dust surface area 71
3.7 Summary and conclusions 77

4 Analyzing temporal variations of AGN emission line profiles 79
4.1 Introduction 81
4.2 Data reduction 83
4.3 BEL shape variation 86
  4.3.1 Testing the temporal stability of the BEL profile 86
  4.3.2 Time evolution of the BEL profile 90
4.4 Modeling BELs 93
4.5 Discussion 102
  4.5.1 Dust production 102
  4.5.2 Kinematic features and possible origin of additional clouds . . 105
4.6 Summary and conclusions 107

5 Summary and Outlook 109
5.1 Summary 111
5.2 Outlook 113
  5.2.1 Improvements to reverberation mapping campaigns 113
  5.2.2 Direct imaging of BLR and dust torus with interferometry . . 114

Glossary **117**

Publications of J. Esser **119**

Bibliography **121**

Acknowledgements **129**

List of Figures

1.1 AGN unification scheme. 7

1.2 State-of-the-art view of AGN structures. 9

1.3 Early depiction of optical BELs of the Seyfert 1 galaxy Mrk 106. 13

1.4 Luminosity radius relation for BLR, dust torus and NGC 4151 19

1.5 Hubble diagram with simulated VEILS data. 21

1.6 Sketch of the dusty outflow model. 24

1.7 Dust survival and vertical structure above the AD of the BLR and dust torus. 25

2.1 Schematic view of the isodelay surfaces as representation of the BLR or dust torus. 31

2.2 Interference pattern for interferometers using one or multiple baselines. 35

3.1 Nuclear fluxes of NGC 3783 between May 2014 and March 2016, derived with GALFIT (Peng et al. 2002). 46

3.2 The fit of the power law structure function needed for the interpolation of the AD signal for the showcase AGN NGC 3783. 50

3.3 Interpolation of the g' band lightcurve using the method of Rybicki & Press (1992) and Press et al. (1992) for NGC 3783. 50

3.4 Observed fluxes and fit according to our model (compare Eq. 3.1) for epochs four to seven of NGC 3783 as an example for an AGN without reddening due to dust in the host galaxy. 55

3.5 Corner plot for model parameters (given in Eq. 3.1) in the case of NGC3783 as an example of an AGN without reddening due to dust in the host galaxy. 56

3.6 Observed fluxes and fit according to our model (compare Eq. 3.1) for the epochs two to five of Mrk 1239 as an example of an AGN with host extinction. 57

3.7 Corner plot for model parameters (given in Eq. 3.1) in the case of Mrk 1239 as an example of an AGN with reddening due to dust in the host galaxy. 58

3.8 Histograms for the model parameters T, τ, α and F_{var}. 59

3.9 Observed fluxes and fit according to our model (compare Eq. 3.1) and an additional blackbody due to the increased flux in the K band. 63
3.10 Dust delay τ plotted against the optical luminosity in the V filter L_V with the dust temperatures indicated by the colors. 66
3.11 Residual between τ_{norm} and the best fit power law from the lower part of Fig. 3.10 against the subclass of the Seyfert type (compare Table 3.2). 70
3.12 Surface area of the dust $C_{2\ \text{surface}}$ plotted against the dust delay τ with the color coding indicating the dust temperatures T. 72
3.13 Normalized dust surface area $C_{2\ \text{norm}}$ as a function of the dust temperature T. 75

4.1 Environment around the Paβ line in each spectrum. 82
4.2 Paβ BEL for our seven observation epochs. 86
4.3 Same as Fig. 4.2 for the O I 844 nm BEL. 87
4.4 Same as Fig. 4.2 for the Brγ BEL. 87
4.5 Mean and rms profile of the Paβ lines. 88
4.6 Paβ BELs normalized with the fit parameters from the rms minimization. 90
4.7 Ratio of fluxes in different velocity bins over the total flux from the Paβ BEL. 92
4.8 Same as Fig. 4.7 but for the sum of the ratios of the O I 844 nm and the Brγ BELs. 93
4.9 Dependence of the shape of BELs on the velocity dispersion and the radial density profile of the BLR clouds. 94
4.10 Parameter space of BEL modelling compared to the January 2006 Paβ line. 98
4.11 Distribution of additional clouds in the BLR in azimuthal direction. . . . 99
4.12 Radial distribution of line emission at the location of additional clouds. . 100
4.13 Dust temperatures for NGC 4151 at smallest dust radius. 103

List of Tables

3.1 Overview of the Gamma-Ray Optical and Near-Infrared Detector (GROND) observations of the AGN in our sample. 43
3.2 Overview of the fit parameters for our single blackbody model (Eq. 3.1). 53
3.3 Comparison of our dust delays for 3C273 and NGC 3783 to the results from GRAVITY Collaboration et al. (2019) using interferometry in the K band. 65
3.4 Expected dust delays of the AGN without estimates of delays or only lower limits determined with reverberation mapping but with the dust temperature determined (compare Table 3.5.1). 73
3.5 Radial extend of the dust torus in units of the measured dust radius for each AGN. The measured delay was assumed to coincide with the inner radius of the dust torus for this. 76

4.1 Journal of observations for our InfraRed Telescope Facility (IRTF) SpeX spectra. 85
4.2 Overview of the fit parameters obtained by the minimization of the rms profile. 91
4.3 Summary of the parameter space of our BEL modeling. 96

CHAPTER 1

Context and Theoretical Background

An Active Galactic Nucleus (AGN) is an extremely bright and extremely compact region located at the center of galaxies. Its strong radiation extends all the way from radio to X-rays and is too a large degree non-thermal. The first observations of the emission lines of AGN were made as early as 1908 by Fath (1909) on NGC 1068. Later more galactic nuclei with similar emission lines were discovered by Seyfert (1943) and later the first quasi-stellar objects (QSOs) were found in the first radio surveys (e.g. Bolton et al. 1949). Schmidt (1963) measured the redshift of a QSO for the first time revealing its extragalactic nature.

AGN play an important role in many aspects of astronomy and physics. Due to their extremely high brightness they are often used to test the early universe and they are assumed to be important for the evolution of galaxies. The relation between the radius of their dust torus or BLR and their luminosity can be used as a cosmological standard candle, which is even brighter than supernovae type Ia. Additionally, AGN are an ideal laboratory of extreme physics (high energy and strong gravity). For many of these applications of AGN a thorough understanding of the structure and the underlying physics in the inner parts of AGN is needed. This inner structure will be explored in this work.

1.1 Typology of AGN

The luminosity of most AGN is higher than the luminosity of all stars of its host galaxy making them the most luminous non-transient objects in the universe. Most of the emission originates in a region smaller than 1 pc. Therefore mechanisms like nuclear fusion are not able to produce the luminosities observed in AGN and only the infall of matter into the gravitational potential of a supermassive black holes (SMBHs) through an AD is able to do so (Salpeter 1964; Zel'dovich 1964). Lynden-Bell (1969) proposed that these SMBHs reside at the center of nearby galaxies and became very massive through earlier accretion episodes. Most AGN show variable emission throughout their spectral energy distribution (SED). The timescales of these variations depends on both the AGN luminosity and wavelength. The wavelength dependence of the variability can be explained by the sizes of the regions dominating the emission at that wavelength.

AGN are divided into different types according to differences of their SEDs. A first major difference is the amount of radio emission. The radio loudness is connected to the presence of a relativistic jet launched close to the SMBH. If a jet is present the amount of radio emission is significantly higher and those AGN are called radio loud while AGN without a jet are called radio quiet. It has to be mentioned that a small jet is present in some radio-quiet AGN. However the radio emission of those jets is too small to define them as radio-loud. The main reference for the description of the typology of AGN is Peterson (1997).

1.1.1 Radio-quiet AGN

Different types of radio-quiet AGN are distinguished dependent on their luminosity. The relatively radio quiet AGN are the so called Seyfert galaxies studied in this work. They show luminous ultraviolet (UV) emission originating from the AD and prominent emission lines in the optical and UV. A further classification of Seyfert galaxies is done using the properties of these emission lines. In the SEDs of Seyfert 1 AGN both narrow emission lines (NELs) with widths of a few 100 km s^{-1} and BELs with widths up to a few 10^4 km s^{-1} are observed while Seyfert 2 AGN only posses NELs. Seyfert galaxies are usually early type spiral galaxies and their bolometric luminosities typically range from $\sim 10^{41}$ erg s^{-1} up to $\sim 10^{45}$ erg s^{-1}.

Radio-quiet quasars (RQQs) are very similar to Seyfert 1 galaxies also showing BELs and NELs. The main difference is that their host galaxies can also be elliptical galaxies and their higher luminosities up to $\sim 10^{48}$ erg s^{-1} (Wolf et al. 2018). Due to their brightness their host galaxies did not show up in early optical surveys and they appeared as point sources. Hence they were called quasi-stellar or short quasars. RQQs without BELs were only relatively recently discovered in X-ray surveys (Martínez-Sansigre et al. 2006a,b) due to their lack of strong optical and radio emission.

1.1.2 Radio-loud AGN

The SEDs of radio-loud quasars (RLQs) are in principle very similar to those of RQQs with the addition of synchrotron emission from a jet. Thus nuclear and especially extended radio emission is added to the SEDs.

Blazars are characterized by only very weak emission lines. While optically violent QSOs only show very weak emission lines, BL Lac do not show any emission lines at all. Their emission is in agreement with pure synchrotron emission originating from a highly relativistic radio jet.

Radio galaxies as the last class of radio-loud AGN show only weak emission lines and also a weak UV access. Their X-ray and optical emission could be produced by a jet only. This could be explained as AGN with only very low accretion rates.

The host galaxies of most of the radio-loud AGN are elliptical galaxies with only very few exceptions. Possible explanations for this are that only SMBHs with the highest masses can power these most luminous jets or that the cold gas in spiral galaxies disrupts the jet formation (Smith et al. 1986).

1.2 AGN unification model

A large step to the understanding of AGN was to explain the different types of AGN mentioned above in Section 1.1 with one common model. This was achieved with the unification model of AGN developed by Antonucci (1993) and Urry & Padovani (1995) and the following section describing this model will be based on those works.

In principle there are two different explanations for the lack of the UV and optical continuum and the BELs in type 2 AGN: Either these structures are not present at all or they are obscured. The first mention of obscuration being responsible for different types of AGN dates back to Rowan-Robinson (1977) because of the excess of infra-red (IR) emssion observed in type 2 AGN. However this view was contradicted by the existence of type 2 Seyferts with weak optical continuum emission with only a low amount of reddening (Koski 1978). A major breakthrough was the discovery of hidden BLRs in the polarized emission of type 2 AGN by Antonucci (1984) for 3C234 and Antonucci & Miller (1985) for NGC 1068. The orientation of the polarization perpendicular to the radio jet axis of 3C234 gives additional evidence to the existence of an obscuring material of dust and gas clouds with the same axis as the radio jet.

With these findings a unification model based on orientation was build. At the center of the AGN accretion to a SMBH is responsible for the UV and optical continuum which illuminates its surroundings. Gas clouds orbiting the SMBH at high velocities are located in the BLR. Surrounding both the AD and BLR is a dusty torus responsible for both the obscuration of these two components depending on the viewing angle and the reflection and thus polarization of their emission. Located further outside are more gas clouds in the narrow line region (NLR) orbiting the AGN at lower velocities. Due to this larger distance the NLR can not be obscured and is therefore visible in type 1 and type 2 AGN. An illustration of this model is given in Fig. 1.1.

This unification model can largely explain the common phenomena seen in radio-quiet AGN but there are still questions about some of the properties of radio-loud AGN and which mechanisms are important for the existence of the radio jet. At first the different host galaxy types and thus the differences in environment of AGN was used as an explanation by Smith et al. (1986). The existence of a jet might thus be connected to the amount of gas in the host galaxy. Later the black hole (BH) spin was added as a possible explanation. Blandford et al. (1990) and Wilson & Colbert (1995) claimed that a high BH spin is needed for the formation of powerful radio jets. It was later shown that the radio-loudness is not connected

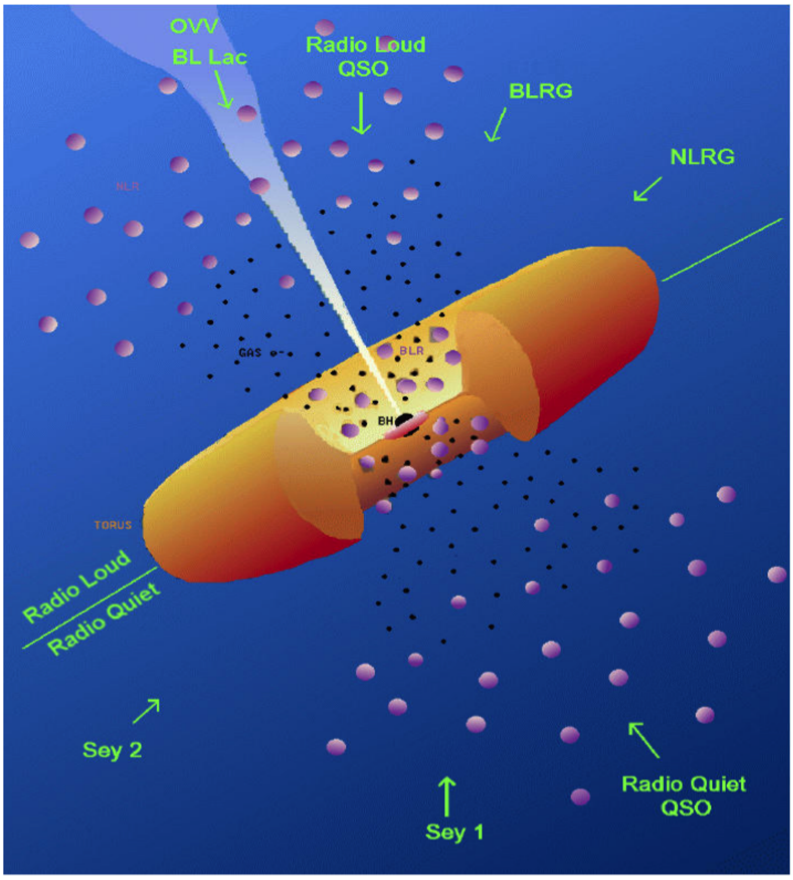

Figure 1.1 Illustration of both the radio loud and radio quiet unification of AGN depending on viewing angle as developed by Antonucci (1993) and Urry & Padovani (1995) (Figure Credit: Southampton Gamma Ray Astrophysics Group).

to properties like the accretion rate and thus a connection to the BH spin is likely (e.g. Sikora et al. 2007). This also suggests that elliptical galaxies generally inhibit SMBHs with a larger spin than spiral galaxies.

The unification of radio-loud AGN follows the same chain of argument as for the radio-quiet AGN and the different appearance can be connected to different viewing angles. The SEDs of BL Lac objects without any emission lines can be explained with the radio jet being directed exactly in the line of sight. This way the emission from other AGN components is completely swamped by the radio jet emission. The viewing angles of all the mentioned types of AGN is shown in Fig. 1.1.

Despite the success to describe most AGN phenomena to date, there have been and are some challenges to the described unification models. Some Seyfert type 2 galaxies have been found to be "true" type 2s possessing not even a hidden BLR (Veilleux et al. 1997; Tran 2001). This could be explained with low accretion rates at which no (detectable) BLR is formed (e.g. Nicastro et al. 2003; Bianchi et al. 2008; Baskin & Laor 2018).

More recently "changing-look" AGN have been brought into focus. After a first detection of an AGN "loosing" its BELs and thus changing from type 1 to type 2 by Cohen et al. (1986) more of these optically changing AGN (e.g. Denney et al. 2014; LaMassa et al. 2015; McElroy et al. 2016) and AGN changing their X-ray properties from Compton-thick to Compton-thin (e.g. Ricci et al. 2016) have been found. While the changes in the X-rays are consistent with changes of obscuration, this is not the case for the changes of the emission lines. Linear polarization measurements of "changing-look" AGN suggest that the change in AGN type is not caused by obscuration and thus it is rather due to changes of the accretion rate (Hutsemékers et al. 2019). However as these changes have also been found in relatively bright sources (e.g. LaMassa et al. 2015) the vanishing BLR can not have the same reason as the true type 2 Seyferts mentioned above and it is therefore challenging to bring these "changing-look" AGN into agreement with the unification model.

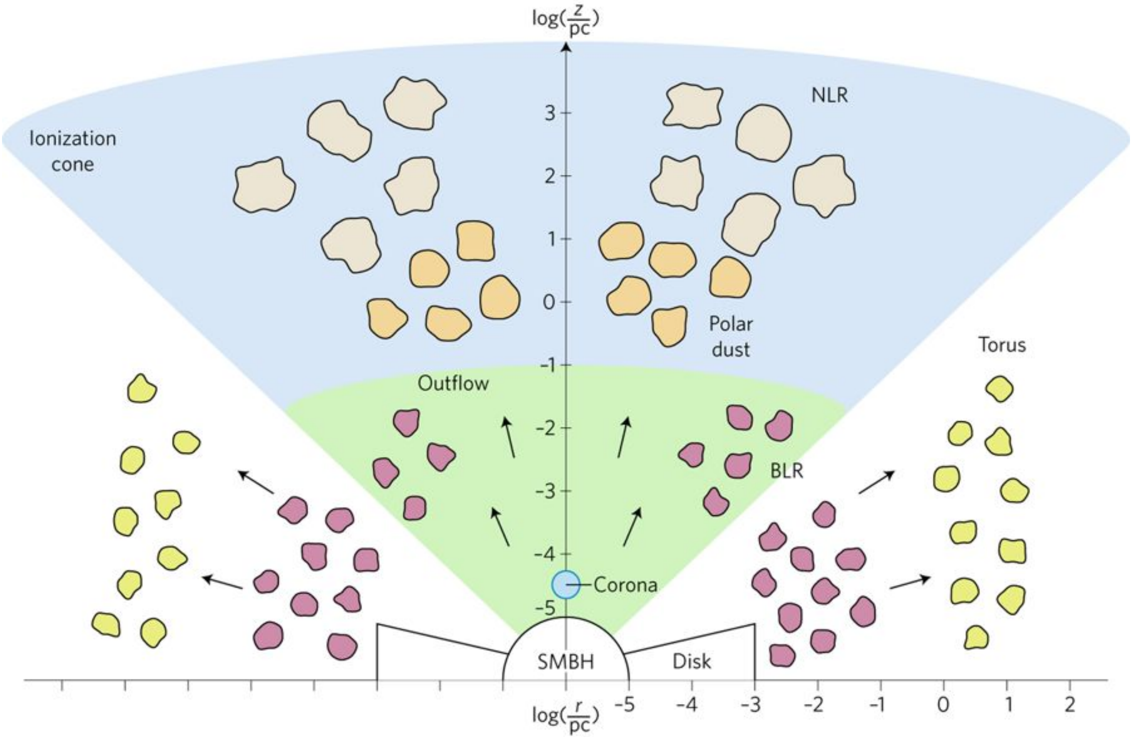

Figure 1.2 State-of-the-art view of the structure of AGN from the immediate vicinity of the SMBH to host galaxy scales. Graphic is taken from Ramos Almeida & Ricci (2017).

1.3 Dust in AGN

In the unified model of AGN described above the dust torus was assumed to be a smooth structure. While the function of the dust (obscuring the inner parts of AGN) is unchanged, the view of the dust distribution and structure have changed dramatically. In this section the current picture of the dust distribution in the dust torus and also in the polar region of AGN will be described based on the review from Ramos Almeida & Ricci (2017). In Fig. 1.2 an illustration of the state-of-the-art view of AGN structures is given.

Overall the dust structure in AGN is extremely complex and diverse. It consists of two components: A polar and an equatorial component (the torus), which will be described in this chapter. The polar structure is possibly part of an outflowing wind while the torus component is responsible for the obscuration and its structure is compact and clumpy.

1.3.1 The dust torus

First observations of hot dust close to the sublimation temperature detected a near infra-red (NIR) and mid infra-red (MIR) continuum emission, which was consistent with the reradiation of the UV and optical AD emission by a dusty torus (e.g. Storchi-Bergmann et al. 1992). Using interferometry it was possible to resolve the dust torus in the MIR for both type 1 and 2 Seyfert galaxies (e.g. Jaffe et al. 2004; Tristram et al. 2007; Burtscher et al. 2009). However it was only possible to infer the outer radii of the dust torus for nearby AGN which have scales of a few parsec for a cold dust component with temperatures around 300 K and subparsec sizes for a hot inner component with temperatures above 800 K. Later the subparsec sizes of the hot component were confirmed using NIR interferometry (e.g. Swain et al. 2003; Pott et al. 2010; Kishimoto et al. 2011; Weigelt et al. 2012).

Due to the size of the torus we are only able to measure the size of the torus directly (compare Chapter 2) but we are not resolving the inner structure (details) of the torus directly. Therefore torus models reproducing the SED of the torus are needed to give constraints on the structure and composition of the torus. Early work modeling the IR SEDs of the dust tori by Pier & Krolik (1992) and Pier & Krolik (1993) assumed a smooth distribution of dust for reasons of simplicity. However it was known even earlier that a smooth distribution of dust can not survive in an AGN (e.g. Krolik & Begelman 1988) and the dust has to be distributed into small and dense clumps. Additionally the SEDs could not be well reproduced with smooth torus models.

Therefore the simple smooth torus models were changed to clumpy torus models which either focus on physical processes such as AGN and supernova feedback and inflows (Wada & Norman 2002; Schartmann et al. 2008; Wada 2012) or on the reproduction of the observed SED using different torus geometries and dust compositions (Nenkova et al. 2008a,b; Hönig & Kishimoto 2010a; Stalevski et al. 2012; Siebenmorgen et al. 2015). In many ways the clumpy torus models have been successful. The geometrical models in particular have been very helpful performing statistical analysis of torus parameters (e.g. Ramos Almeida et al. 2011) but also modelling individual SEDs (e.g. Hönig & Kishimoto 2010b; Lira et al. 2013). SED modelling can help us understanding a wide range of torus parameters like the torus height and outer radius or the covering factor connected to the number of clouds in the line of sight. The number of clouds in the line of sight is directly dependent on the size of the clouds and the total number of clouds, unfortunately it is most likely impossible to determine these two values individually.

Despite the clumpy structure also the view of the overall shape of the torus is changed. Previously, the shape was compared to a doughnut (compare Fig. 1.1) but recent studies taking into account the anisotropic radiation of ADs contradict this view. The radiation field is smaller close to the AD (compare Fig. 1.7) and therefore dust can survive at smaller heights above the AD at lower radii. From this argument follows a bowl shaped inner dust torus (e.g. Kawaguchi & Mori 2010; Baskin & Laor 2018).

The composition of the dust in the torus depends largely on the temperature of the dust. As silicate grains sublimate at lower temperatures than graphite grains, graphite grains will dominate closer to the center of the AGN. Landt et al. (2014) find dust temperatures around 1500 K at the inner edge of the torus for most AGN. At these temperatures all silicate grains sublimate and the innermost dust should be devoid of silicate.

The diversity of the appearance of the torus becomes apparent considering the quasars without hot dust emission in the NIR found by Jiang et al. (2010) at high redshift ($z \approx 6$). They proposed the solution, that these dust poor AGN are caused by a dust-free environment. In contradiction to this explanation low redshift counterparts were found by Hao et al. (2010, 2011); Jun & Im (2013); Lyu et al. (2017). Among a variety of other explanations for these types of AGN are super-Eddington accretion rates (at high redshift), leading to thick ADs (compare Section 1.5) and the thick ADs do not allow a dust torus to form. For the local AGN extremely low accretion rates and larger opening angles of the torus are proposed, again disallowing the formation of the dust torus.

1.3.2 Polar dust

Apart from dust in the torus, dust is also found in the ionization cone of AGN. While polar dust in the NLR of AGN (at distances on scales above 100 pc from the AGN itself) was first found by Cameron et al. (1993) a nuclear polar dust component on pc scales above the AD could be observed in some Seyfert galaxies using interferometry (Hönig et al. 2012, 2013; Tristram et al. 2014; López-Gonzaga et al. 2014). The nuclear polar dust has been interpreted as an outflowing dusty wind launched in the innermost part of the dust torus close to the sublimation region and is consistent with radiation-driven hydrodynamic models (e.g. Wada 2012; Wada et al. 2016). As it is launched in the inner region of the torus its composition should be also dominated by graphite grains. The polar dust component can help explaining some NIR and MIR bumps in the SEDs of some AGN. It is still unclear whether the polar dust component is ubiquitous in AGN and the low detection rates are caused by observational limitations (Asmus et al. 2016).

1.4 The Broad Line Region

The BLR is a region within the dust torus where dust free gas clouds orbit the SMBH. These clouds are photoionized by the radiation of the AD and have temperatures around 10,000 K (e.g. Peterson 1997; Sulentic et al. 2000). It is generally assumed that the outer radius of the BLR coincides with inner radius of the dust torus (compare Fig. 1.2). The flux ratio of BELs and NELs are used as the basis to define subclasses for Seyfert galaxies (Osterbrock & Koski 1976; Osterbrock 1977). An early suggestion on the origin of the BLR was outflows from stars in the central region of the AGN. But it is not easy to provide enough gas to sustain the BLR on long enough timescales through this channel. More recently an origin in the AD is suspected (Czerny & Hryniewicz 2011; Czerny et al. 2017). A detailed description of this model for the formation of the BLR will be given in Section 1.7.2.

The BELs allow us to constrain the cloud velocities unlike the thermal continuum emission of the dusty torus. These velocities can reach up to a few 10,000 km s^{-1} depending on the mass of the SMBH and the distance to the SMBH. Thus BELs are often used to determine the masses of SMBHs. Assuming the gas is in virial equilibrium the SMBH mass (M_{BH}) can be determined using

$$M_{\mathrm{BH}} = \frac{f R_{BLR} \Delta V^2}{G}, \tag{1.1}$$

where R_{BLR} is the radius of the BLR[1], G is the gravitational constant, and ΔV is the width of the BEL. f is a factor depending on the the structure and kinematics of the BLR and those are both poorly understood and very complex, as the BLR likely consists of multiple components (e.g. Sulentic et al. 2000; Popović et al. 2004; Ilić et al. 2006; Bon et al. 2009).

The BELs alone can give only weak constraints on the structure of the BLR. A great advancement can be expected from new interferometric instruments. Most BELs have a single peaked shape (an example of typical BELs is shown in Fig. 1.3) and only for Full Width Half Maximums (FWHMs) above 10,000 km s^{-1} the shape can become double peaked (Eracleous & Halpern 2003). A double peaked BEL is indicative of a disk like BLR as the cloud velocities are dominated by Keplerian rotation.[2]

BELs show variability in both their overall flux and their shape (e.g. Sulentic et al. 2000; Shapovalova et al. 2010; Ilić et al. 2015). While the changes of flux

---

[1] The dependency between R_{BLR} and the AD luminosity is described in Section 1.6.

[2] In the left part of Fig. 4.9 the relation between velocity dispersion perpendicular to the AD plane σ and the shape of the BEL is shown (Stern et al. 2015). A larger value of σ can also be understood as a larger height of the BLR.

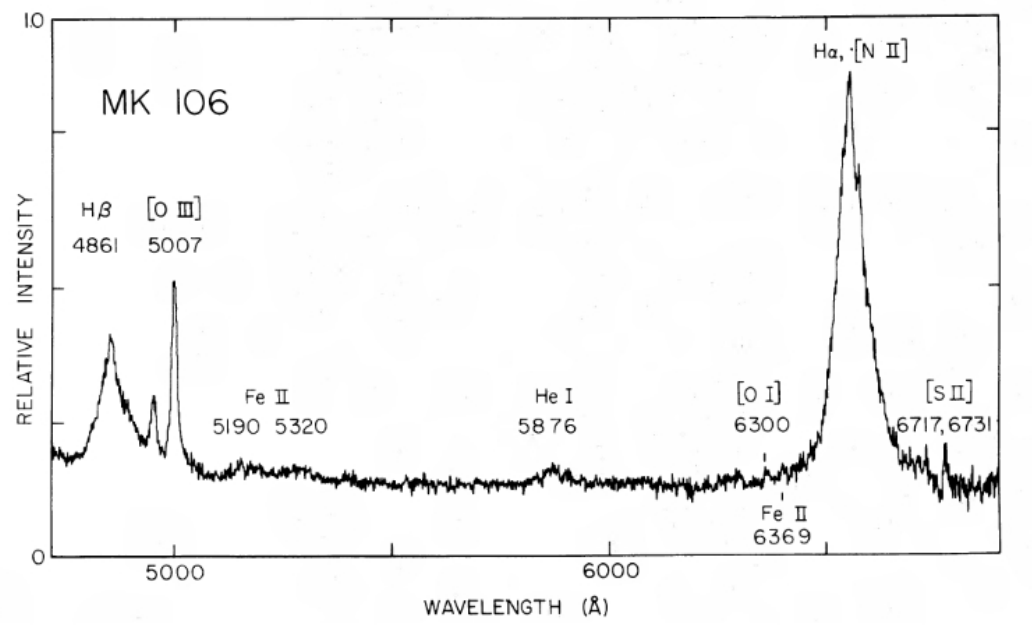

Figure 1.3 Early depiction of optical BELs of the Seyfert 1 galaxy Mrk 106. Especially Hα and Hβ are prominent although superposed by NELs (indicated by the square brackets). The figure was taken from Osterbrock (1977).

are associated with changes of the AD brightness, the shape variations have to be caused either by changes of the cloud distribution or by inflows and outflows.

Through a couple of simple arguments adapted from Peterson (2006) we can constrain the BLR cloud size (R_C) and the number of clouds (N_C) for an individual AGN. The covering factor of the BLR is proportional to $N_C R_C^2$ and can be estimated by how much of the ionizing flux is reprocessed in BEL emission. This is usually around 10 % for typical Seyfert galaxies. Additionally the total BEL flux should be proportional to $N_C R_C^3$. With this we can solve for the two values individually leading to $N_C \approx 10^7$ and $R_C \approx 10^{13}$ cm for the typical Seyfert galaxy NGC 5548. Combining this with the putative particle density $n_e \approx 10^{10}$ cm^{-3} we arrive at a column density of $N_H \approx 10^{23}$ cm^{-2}. Comparable values of the column densities were also found for measurements of the warm X ray absorbers assumed to be BLR clouds (e.g. Nandra & Pounds 1994). With the number, size and density of the BLR clouds we can also compute the total mass of the BLR. In this case this is approximately 1 $M_\odot$. It might be surprising that such a small mass can be responsible for such a prominent feature of the AGN SED but the emissivity for dense gas is proportional to n_e^2 and thus extremely effective in the BLR.

1.5 The Accretion Disk

Most mass is accreted onto a black hole by means of an AD. The interplay of turbulence within the AD and the viscosity of the AD material can move angular momentum outwards and cause material to spiral inwards. This line of argument was initially made by Shakura & Sunyaev (1973) and the α disk developed by them is to date mostly used to explain most phenomena of ADs in AGN. The following section explaining the physics behind and different appearances of ADs follows largely the line of argument of Netzer (2006).

1.5.1 The Eddington luminosity

Before moving to the AD itself the concept of the Eddington luminosity (L_{edd}) has to be introduced, because the appearance of ADs changes with the luminosity of the AD relative to its Eddington luminosity. An accretion flow is possible as long as the gravitational force of the central object is larger than the radiation pressure acting outwards on particles in the accretion flow. L_{edd} describes the luminosity at which gravitational force and radiation pressure are equal. In principle this gives an upper limit to the luminosity of the AD although we will later show how to achieve even higher luminosities and thus higher accretion rates.

In order to derive an expression for L_{edd}, we can write the gravitational force as:

$$F_{\mathrm{g}} = \frac{G M_{\mathrm{BH}} \mu m_{\mathrm{p}}}{r^2}, \tag{1.2}$$

where G is the gravitational constant, M_{BH} is the central or in our case black hole mass, μ is the mean number of protons and neutrons (in our case approximately 1.17, assuming a solar composition of the gas), m_{p} is the proton mass, and r is the distance between the BH and the particle. The radiation pressure for a fully ionized plasma (if the gas is only partly ionized F_{r} would be smaller) is defined as:

$$F_{\mathrm{r}} = \frac{\sigma_{\mathrm{T}}}{4\pi \mathrm{r}^2 \mathrm{c}} L, \tag{1.3}$$

where σ_{T} is the Thomson cross section and L is the total luminosity of the AD. With $F_{\mathrm{g}} = F_{\mathrm{r}}$ we arrive at a luminosity of:

$$L_{Edd} = \frac{4\pi \mathrm{c} \mathrm{G} \mathrm{M}_{\mathrm{BH}} \mu \mathrm{m}_{\mathrm{p}}}{\sigma_{\mathrm{T}}} \simeq 1.5 \times 10^{38} \frac{M_{\mathrm{BH}}}{M_{\odot}} \mathrm{ergs}^{-1}. \tag{1.4}$$

With the accretion rate $\dot{M} = L/\eta c^2$, where η is the efficiency converting gravitational energy into radiation, we can also define also the according Eddington accretion rate:

$$\dot{M}_{Edd} = \frac{L_{Edd}}{\eta c^2} \simeq 3 \frac{M_{\rm BH}}{10^8 M_\odot} \left(\frac{\eta}{0.1}\right)^{-1} \mathrm{M_\odot yr^{-1}}. \tag{1.5}$$

The ratio of the accretion rate of an AGN and the Eddington accretion rate is commonly used to describe the accretion of an AGN.

1.5.2 Thin accretion disks

For ADs with a luminosity of about $10^{-4}\ L_{Edd} \lesssim L \lesssim 0.3\ L_{Edd}$ one generally assumes a thin geometry for the AD (Laor & Netzer 1989), because the AD height is mainly supported by gas pressure and radiation pressure is negligible. The important physical parameters of the AD are the angular momentum at a certain radius $S(r)$, the torque acting on the particles $N(r)$ and responsible for the inward motion and the resulting radial velocity of particles in the AD v_r. It is generally assumed that the azimuthal velocity v_ϕ in ADs is significantly larger than v_r and therefore v_ϕ is approximately the Keplerian velocity at that radius. Therefore the angular momentum is:

$$S(r) = m v_K r = m\sqrt{G M_{\rm BH} r} \tag{1.6}$$

and we can write the accretion rate as:

$$\dot{M} = -2\pi r \Sigma v_r, \tag{1.7}$$

where Σ is the surface density of the AD. If we assume conservation of angular momentum, thus $N(r) - \dot{M}S(r) = const$ we can write our last parameter as $N(r) = \dot{M}\sqrt{G M_{\rm BH} r} + const$. At a radius where the relativistic angular momentum reaches a minimum this description breaks down and the orbits are not Keplerian any more. This radius marks the inner edge of the AD and depends on the rotation of the BH. An inner radius of the AD around 6 ${r_g}^3$ for a BH non rotating is found. In the case of rotating BHs the inner radius can reach values of 9 r_g for a maximal retrograde rotating BH and can decrease to values as low as 1 r_g for maximal prograde rotating BHs (Bardeen et al. 1972).

With these parameters we can calculate a few observable properties of the ADs. First we can consider that the emitted energy at some radius has to be the sum

---

[3] r_g is the gravitational radius of a BH at which $v_K = c$ and thus $r_g = G M_{\rm BH}/c^2$.

of the lost gravitational energy and the loss of energy of the angular momentum which are:

$$dL_g = -d\left(\dot{M}\frac{GM_{\mathrm{BH}}}{2r}\right), \tag{1.8}$$

as the kinetic energy at r_{in} is half of the potential energy and thus is not radiated away, and

$$dL_N = -d(N\Omega_K) = -d\left(\left(\dot{M}\frac{GM_{\mathrm{BH}}}{r}\right)\left(1-\sqrt{\frac{r_{in}}{r}}\right)\right). \tag{1.9}$$

The term to the right corrects for the fact that not all angular momentum is lost at r_{in}. In the relativistic case this term becomes more complicated and the following steps will not be trivial. We therefore stay within the non-relativistic approximation. Through derivation with respect to r we get:

$$\frac{dL}{dr} = \frac{dL_g + dL_N}{dr} = \frac{3G\dot{M}M_{\mathrm{BH}}}{2r^2}\left(1-\sqrt{\frac{r_{in}}{r}}\right) \tag{1.10}$$

for the total radiated energy at a certain radius. With this we can determine the total energy of the AD $L = 0.5GM_{\mathrm{BH}}\dot{M}r_{in}^{-1}$ (half of the total gravitational energy) and the temperature as a function of r. From Eq. 1.10 we can get the emissivity per unit area:

$$D(r) = \frac{3G\dot{M}M_{\mathrm{BH}}}{8\pi r^3}\left(1-\sqrt{\frac{r_{in}}{r}}\right) \tag{1.11}$$

and assuming that locally the emission can be described by a blackbody with temperature T so that $D = \sigma T^4$ we get

$$T(r) = \left(\frac{3G\dot{M}M_{\mathrm{BH}}}{8\pi\sigma r^3}\left(1-\sqrt{\frac{r_{in}}{r}}\right)\right)^{\frac{1}{4}}. \tag{1.12}$$

Assuming a typical mass of a SMBH around 10^8 $\mathrm{M}_\odot$ we get an estimate of the temperature at the inner edge of the AD of 10^5 K. This means that the AD emission peaks in the UV.

1.5.3 Thick accretion disks

For $L \gtrsim 0.3\ L_{Edd}$ radiation pressure starts to dominate over the gas pressure in the AD (Laor & Netzer 1989). As $P_{rad} \propto T^4$ the thickness of the AD quickly increases with higher accretion rates and we speak of thick ADs. First models of thick ADs were developed among others by Paczyńsky & Wiita (1980) and Abramowicz et al. (1980).

In this environment the timescales at which photons are able to escape the AD become larger than the timescales of the accretion flow. The photons can become trapped in the disk and the radiation efficiency becomes smaller Narayan (2005). Radiation is no longer the dominant cooling mechanism and the accretion flows become advection dominated (e.g. Narayan & Yi 1994; Abramowicz et al. 1996). Most of the energy is carried away in winds and outflows. In this way it is possible to achieve accretion rates larger than the Eddington accretion rate.

1.6 The radius luminosity relation

The radial distance of dust in AGN to the SMBH is expected to be mainly dependent on the UV luminosity of the AD as the radiation from the AD is the main heating source of the dust. If the dust temperature reaches a temperature up to 1900 K for graphite grains and 1400 K for silicate grains the dust will sublimate (e.g. Barvainis 1987; Schartmann et al. 2005; Nenkova et al. 2008a; Baskin & Laor 2018). The sublimation temperature can vary slightly, as they also depend on the density of the dusty clouds and the grain size of the dust. For dust temperatures below 1000 K on the other hand new dust can be created, as the conditions (e.g. the gas density) in the BLR and the dust torus are similar to the atmospheres of evolved stars (Groenewegen et al. 2009). The flux at the location of the dust (F_{AD}) is related to the AD luminosity (L_{AD}) and the dust radius (R_{dust}) as:

$$F_{\mathrm{AD}} = \frac{L_{\mathrm{AD}}}{4\pi R_{\mathrm{dust}}^2}. \tag{1.13}$$

F_{AD} should be similar in all AGN heating the dust to temperatures between 1000 and 1900 K. Thus we arrive at the radius luminosity relation:

$$c\tau \approx R_{\mathrm{dust}} \propto \sqrt{L_{\mathrm{AD}}}. \tag{1.14}$$

The dust radius is often written as the delay τ corresponding to the light travelling time between the SMBH and the dust torus. However the radius of the dust torus also depends on the dust temperature (T_{dust}) and the grain size of the dust (a). This dependence was described by Barvainis (1987) and later refined by Kishimoto et al. (2007):

$$R_{\mathrm{dust}} = 1.3\sqrt{\frac{L_{\mathrm{UV}}}{10^{46}\mathrm{erg/s}}}\left(\frac{T_{\mathrm{dust}}}{1500\mathrm{K}}\right)^{-2.8}\left(\frac{a}{0.05\mu\mathrm{m}}\right)^{-0.5}\mathrm{pc}. \tag{1.15}$$

The temperature dependency of this equation can be derived when assuming that the radiation absorbed and emitted by the dust is equal and the UV absorption efficiency of the dust is constant and equal to unity. Therefore

$$\frac{L_{\mathrm{UV}}}{R_{\mathrm{dust}}^2} \propto \int \nu^{\gamma} B_{\nu}(T_{\mathrm{dust}}) d\nu, \tag{1.16}$$

where $B_{\nu}(T_{\mathrm{dust}})$ is Planck's law and γ is the power law index of the NIR absorption efficiency curve. For a dust grain with a size of 0.05 μm we can assume that $\gamma \approx 1.6$. Solving the right hand side of Eq. 1.16 we get

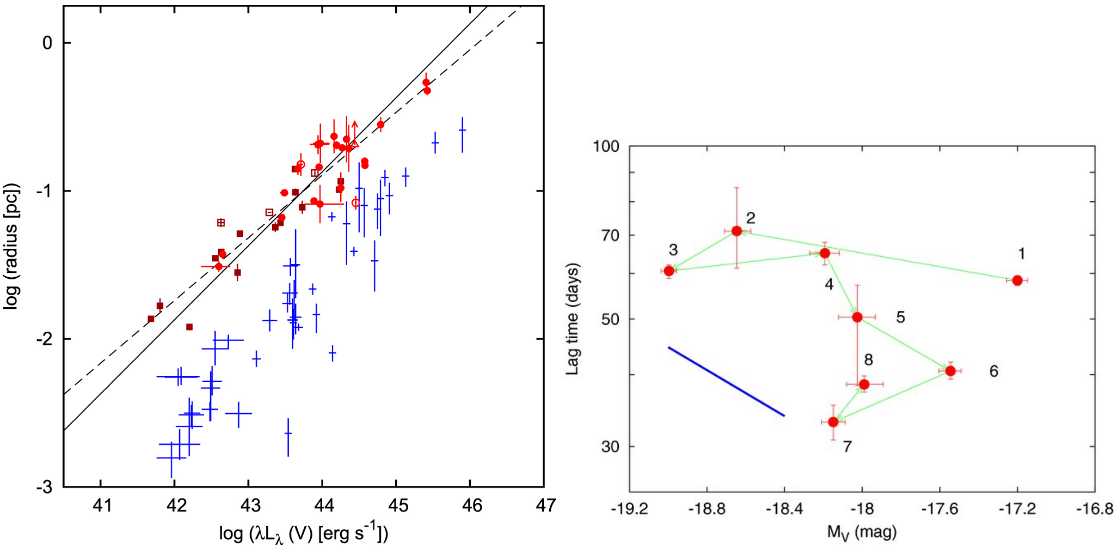

Figure 1.4 In the left figure (taken from Minezaki et al. 2019) the radius luminosity relation for the BLR (blue crosses) from Bentz et al. (2013) using Balmer emission lines and the dust torus (red symbols) from Koshida et al. (2014) and Minezaki et al. (2019) are shown. The solid line represents a fit to the dust radii with a slope fixed at 0.5 while the dashed line represents a fit with free slope. In the right figure (taken from Koshida et al. 2009) the evolution of the radius luminosity relation of NGC 4151 over six years is shown. The solid line indicates the expected $\tau \propto L^{0.5}$ relation, which is not in agreement with the data.

$$\frac{L_{\mathrm{UV}}}{R_{\mathrm{dust}}^2} \propto T_{\mathrm{dust}}^{4+\gamma} = T_{\mathrm{dust}}^{5.6} \equiv R_{\mathrm{dust}} \propto \sqrt{L_{\mathrm{UV}}} T_{\mathrm{dust}}^{-2.8}. \tag{1.17}$$

Most of the measurements of R_{dust} are done using reverberation mapping (introduced in Section 2.1). For this technique the delay between changes of the AD luminosity to changes of the dust emission is measured. Due to the atmospheric extinction of UV radiation optical fluxes (usually the V band) are used as a proxy of the AD radiation. In the NIR the K band is mostly used to measure the dust emission. In the left plot of Fig. 1.4 the dust radii determined by Koshida et al. (2014) and Minezaki et al. (2019) (red symbols) are plotted against the luminosity in the V band. While the radii roughly follow the $R_{\mathrm{dust}} \propto L_{\mathrm{UV}}^{0.5}$ relation (solid line) the slope of the fit is slightly smaller than 0.5 (dashed line). Additionally the radii are approximately a factor of three smaller than expected in Eq. 1.15. This is most likely caused by geometric effects (described in more detail in Chapter 2) and the anisotropic radiation of the AD (e.g. Kawaguchi & Mori 2010; Pozo Nuñez et al. 2014; Baskin & Laor 2018). Comparing the radii of the dust to BLR radii determined by Bentz et al. (2013) we find that the BLR is indeed located within the dust torus at radii four to five times smaller than the dust radii.

Despite the shallower slope a significant scatter can be seen for the luminosity radius relation. Part of this scatter might be caused by different viewing angles. Simulations of dust tori with different viewing angles by Kawaguchi & Mori (2011) predict larger measured lag times for larger viewing angles. The reason for this is self-occultation of clouds located towards the observer. These clouds have smaller lag times as the AD radiation travels closer to the line of sight towards them. As the emission of these clouds is reduced with higher viewing angles the lag time is overestimated. Koshida et al. (2014) looked for correlations between the Seyfert class, and thus supposedly the viewing angle, to the measured dust radii but could not find any. For Eddington ratios around and above one changes of the luminosity radius relation are expected as well (Kawaguchi & Mori 2011; Kawakatu & Ohsuga 2011). As the Eddington ratios of local AGN investigated in this work are much smaller than one this can be neglected here.

Even if we look at the evolution of the lag time for individual AGN as a function of their V band luminosity a significant scatter can be seen. An example of this can be seen in the right plot of Fig. 1.4 from Koshida et al. (2009). Time lag and optical luminosity of NGC 4151 were determined over six years and a large scatter of the $\tau \propto L^{0.5}$ relation (indicated by the solid line) can be seen as well. Also in some cases no changes of the dust radius were observed despite significant changes of the optical radiation (e.g. Pott et al. 2010). All this shows that the dependency of the dust radii on other AGN parameters is not fully understood.

1.6.1 Using the radius luminosity relation as a standard candle

The radius luminosity relation connects a distance independent quantity (the radius) to the luminosity of an AGN. This enables us to use this relation as a standard candle for measurements of the luminosity distance. Other examples for standard candles are Cepheids or Supernova type Ia. Standard candles are used to determine distances and subsequently probe cosmological models and the parameters therein, especially the ΛCDM model. It enables us to determine the scale factor or the expansion rate of space as a function of time.

The main advantage of using AGN as standard candles is their high luminosities enabling observations at high redshift. Compared to Supernovae an additional advantage is that they are not transient and therefore observations can be reproduced. It has been proposed that reverberation mapping of the BLR can be done up to a redshift of $z \sim 4$ (Watson et al. 2011; Czerny et al. 2013; King et al. 2014).

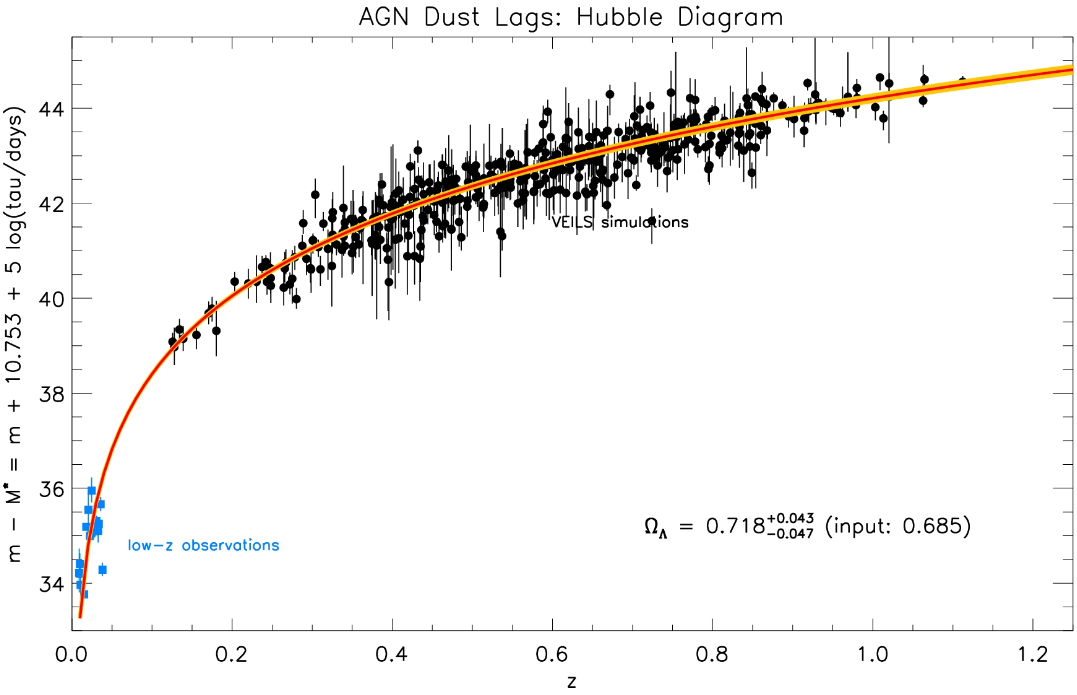

Figure 1.5 Hubble diagram with simulated VEILS data (black dots) and additional low redshift data from the literature. In the lower right corner the determined and input value of Ω_Λ. The graph was taken from Hönig et al. (2017).

In comparison, the most distant reported Supernova type Ia to date is located at a redshift of $z = 1.914$ (Jones et al. 2013). At a redshift of four we are probing a time only $\sim$ 1.5 Gyr after the Big Bang within the ΛCDM model deep into the matter-dominated era. Despite the large distance time dilation further complicates reverberation mapping at high redshifts. At a redshift of four the lag of an AGN is four times longer compared to an AGN with comparable luminosity in the local universe. Therefore reverberation mapping campaigns at high redshift take significantly longer. It is therefore advisable to use BEL reverberation mapping as the lags are shorter compared to the dust torus and the BELs are easier to observe in brighter AGN compared to the dust torus.

Lira et al. (2018) were able to determine BEL lags for 17 AGN with redshifts higher than three already close to the theoretical maximum redshift for reverberation mapping. As all of their AGN have similar (high) luminosities results from lower redshift had to be added to determine the radius luminosity relation. For all tested BELs the slope is within two sigma of the expected $r \propto L^{0.5}$ relation.

The VEILS survey is a first attempt to use dust delays as standard candles for a redshift range between 0.1 and 1.2 (Hönig et al. 2017). It is projected that the time lags for approximately 450 AGN can be determined and using these lags the Ω_Λ parameter of the ΛCDM model can be determined with the same accuracy as current Supernova samples.

The main limitation using the radius luminosity relation as standard candles is the scatter of the relation around 30 % (Suganuma et al. 2006). An additional issue are that the slopes especially for the dust torus are flatter than expected (e.g. Minezaki et al. 2019). The reasons behind both of these problems have to be understood using reverberation mapping of local AGN.

1.7 Formation of dust torus and BLR

In order to produce dust in AGN three different scenarios are possible. At first the dust could be produced outside the AGN by evolved stars and subsequently the dusty clouds fall towards the center of the AGN (Schartmann et al. 2010). The other possibility is dust production within the AGN itself. Either the dust, and thus also the clouds of the BLR, is produced as a dusty outflow from the AD or directly above the AD as soon as low enough temperatures in the BLR are reached. For the last scenario temperatures below 1000 K have to be reached as the conditions in the BLR are similar to the atmosphere of evolved stars (Groenewegen et al. 2009), as already mentioned above. However these temperatures are not found even in the dust torus (e.g. Landt et al. 2014). Therefore this scenario will not be further discussed here and we will concentrate on the two other scenarios.

1.7.1 Dust production outside AGN

The production of dust outside the AGN was motivated by the existence of young nuclear star clusters with masses aroung 10^8 $M_\odot$ (Davies et al. 2007). Especially winds from asymptotic giant branch (AGB) stars could provide the gaseous inflow to form the dust torus and the BLR.

A major subject of theoretical AGN research is the stability of the dust torus vertical structure. If the torus is only stabilized by Keplerian rotation it will soon collapse into a thin disk when gas cooling reduces the thermal pressure. This process is finished after a few rotations. However the stars of the nuclear star cluster are distributed in a vertically extended structure (Davies et al. 2007) stabilized by the random motions of the stars. The vertical extend of gas and dust in BLR and torus results naturally from the distribution of the stars according to the models of Schartmann et al. (2010). Yet this process is not strong enough to provide the geometrically thick tori needed in the AGN unification models and additional drivers of turbulence are needed.

1.7.2 Dusty outflow model

Czerny & Hryniewicz (2011) used the luminosity radius relation of the BLR from reverberation mapping and combined it with the temperature in the α disk from Shakura & Sunyaev (1973) as a function of radius (compare Eq. 1.12) to find that the inner radius of the BLR coincides with the AD radius at which a temperature

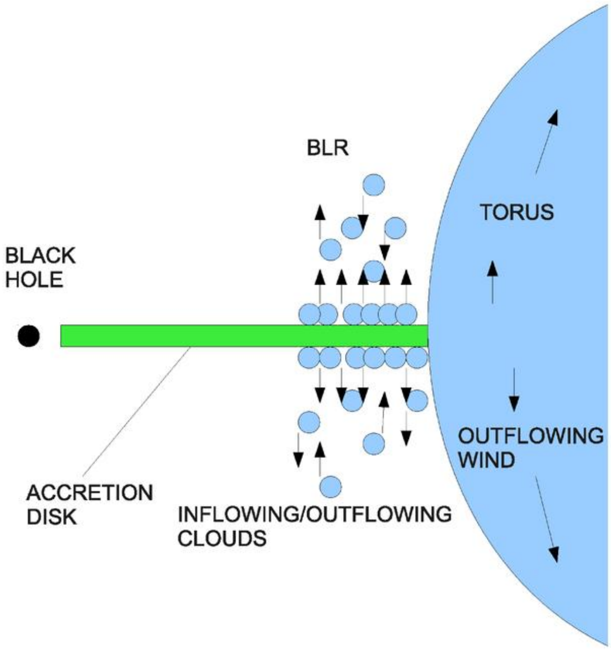

Figure 1.6 Sketch of the dusty outflow model. Dusty clouds can be formed at a distance to the SMBH where the temperature in the AD drops below 1000 K and outwards (Figure Credit: Czerny & Hryniewicz 2011).

around 1000 K is reached. This is the exactly the temperature at which dust production could be possible in this environment.

This finding lead to a model in which dust is produced within the AD. Subsequently the dusty clouds are lifted above the AD by turbulence and winds. Due to the high opacity of the dust radiation pressure from the AD leads to a vertical acceleration of the clouds. As soon as the clouds are high enough above the AD the radiation originating closer to the SMBH can sublimate the dust. Without the dust the opacity of the clouds decreases and after a while the clouds fall back towards the AD. A sketch of this model taken from Czerny & Hryniewicz (2011) is shown in Fig. 1.6.

The dusty outflow model was later refined by Czerny et al. (2017) and Baskin & Laor (2018) to incorporate the anisotropic radiation from the AD and thus providing a model of the vertical structure of the dust torus and BLR. The results of those dynamical models are shown in Fig. 1.7. In the left plot from Baskin & Laor (2018) the anisotropic radiation of the AD and the consequences on the survival of the dust are shown while in the right plot from Czerny et al. (2017) the vertical structure of the BLR and the dust torus are shown.

This enables a number of predictions about both the BLR and the dust torus, like the height of the BLR and dust torus and thus their covering factors or the inner edge of both BLR and dust torus. The inner radius of the BLR is set by the

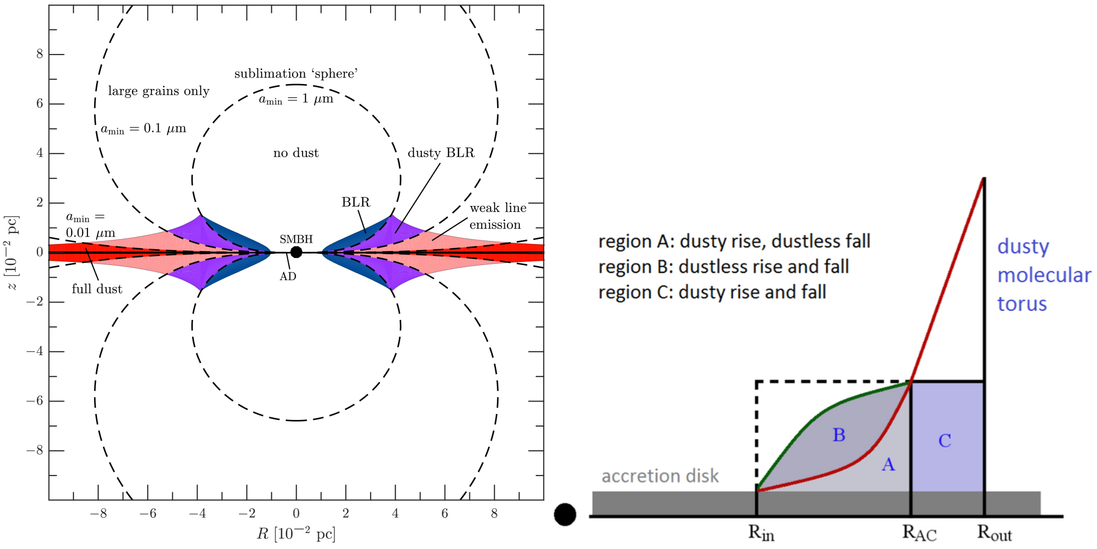
sublimation 'sphere'
$a_{\min} = 1\ \mu$m
large grains only
$a_{\min} = 0.1\ \mu$m
no dust
dusty BLR
BLR
weak line emission
$a_{\min} =$ 0.01 μm
SMBH
AD
full dust
8
6
4
2
0
−2
−4
−6
−8
z [10^{-2} pc]
R [10^{-2} pc]
region A: dusty rise, dustless fall
region B: dustless rise and fall
region C: dusty rise and fall
dusty molecular torus
B
A
C
accretion disk
R_{in}
R_{AC}
R_{out}

Figure 1.7 In the left plot, taken from Baskin & Laor (2018), the anisotropic radiation of the AD and the consequences on the dust survival depending on the grain size, radius, and height above the AD of the dust are shown. In the right plot, taken from Czerny et al. (2017), the vertical structure of the BLR and dust torus can be seen.

temperature within the AD as mentioned above and the outer radius of the BLR is set by the radius at which the dusty clouds can no longer be pushed high enough above the AD to sublimate the dust. This coincides with the inner radius of the dust torus.

Also the scale height of the BLR and the dust torus and thus their covering factors (CFs) can be constrained. Baskin & Laor (2018) arrive at a ratio of the height of the BLR to the radius of the torus of 0.23. This is about a factor of three too small to explain the CF needed to explain the Equivalent Width (EW) of BELs (Korista et al. 1997; Maiolino et al. 2001; Ruff et al. 2012; Baskin et al. 2014). To achieve the needed EW a height to radius ratio of 0.65 is necessary. Baskin & Laor (2018) propose a lower accretion radiative efficiency, meaning a lower ratio of emitted flux to accreted matter, and additional radiation pressure due to dusty clouds below the BLR to provide a greater height. A reduction of the needed CF due to either a harder ionizing SED or the ionizing SED observed is softer than the SED seen by the BLR as proposed by Laor & Netzer (1989) is also possible.

Observations deduce a height to radius ratio of the dust torus of $1/\sqrt{2}$ leading to a CF of 1/3 (Mor & Trakhtenbrot (2011); Mor & Netzer (2012)) slightly higher than the CF from BLR observations. Baskin & Laor (2018) find a similar maximum height of the dust torus. If the clouds reach greater heights above the AD they will be pushed outwards in radial direction and form a wind.

1.8 Structure of this thesis

In this thesis we study the structure of the dust torus and BLR close to the center of AGN. Our goal is a better understanding if and how these two structures are connected. Additionally formation scenarios of clouds in the dust torus and BLR will be tested.

In **Chapter 2** we describe different methodologies to determine the radii of the dust torus and BLR. We will introduce the concept of reverberation mapping, later used to determine radii of dust tori. Additionally interferometry is introduced, capable of measuring torus and BLR radii more directly. In order to illustrate the capabilities of both methods, we also highlight some results from each method.

Chapter 3 is dedicated to our multiwavelength reverberation mapping campaign. We will explore the influence of our novel temperature normalization on the radius luminosity relation. Furthermore our estimates of the surface area of the dust are used to find intrinsic differences between the dust tori. The results of this study will be published in an upcoming paper submitted to *Astronomy & Astrophysics* (Esser et al. subm.).

In **Chapter 4** shape variations of NIR BELs of NGC 4151 are analyzed. The shape variations are used to analyze possible cloud distributions, especially in azimuthal direction, which could be responsible for the observed variations. We also compare the shape variations to concurrent changes of the dust torus radius. The results of this study have been published in *Astronomy & Astrophysics* (Esser et al. 2019).

Finally we summarize our results and present some ideas for possible future projects to further improve our understanding of the dust torus and BLR in **Chapter 5**.

Throughout this thesis we assume the cosmological parameters $H_0 = 67.8 \pm 0.9$ kms^{-1}Mpc^{-1}, $\Omega_m = 0.308 \pm 0.012$, and $\Omega_\Lambda = 0.692 \pm 0.012$ from Planck Collaboration et al. (2016).

CHAPTER 2

Measuring structure sizes in AGN

There are several reasons why distance measurements in AGN are of huge importance. Among these reasons is the radius luminosity relation described in Section 1.6. But also the masses of the SMBHs can be determined using the distance between SMBH and the BLR and the width of the BEL (Eq. 1.1).

However due to the large distances of AGN and relatively small angular sizes of both dust torus and BLR, the radii of the BLR and the dust torus are not easy to determine. Even for the relatively nearby AGN the angular resolution needed to measure the inner dust radius or the BLR radius is well below 1 milliarcsecond(mas). Not even the largest single dish optical and NIR telescopes in construction or planning, like the Extremely Large Telescope (ELT), can achieve such high resolutions. In fact the diameter of a single dish telescope large enough to achieve angular resolutions below 1 mas at a wavelength of 1 μm (where the dust emission starts to dominate the AD emission) is above 200 m.

In order to still be able to resolve the BLR and the dust torus two techniques have been developed: Reverberation mapping and interferometry. The basics of both techniques will be introduced in the following chapter. Especially reverberation mapping as it will be used in Chapter 3 to determine dust radii of nearby AGN. The part about reverberation follows largely the line of argument of Peterson (1993), while the part about interferometry is based on Monnier (2003).

2.1 Reverberation mapping

The basic idea behind reverberation mapping is that the UV emission from the AD illuminates both the BLR and the dust torus. This way the changes of emission of the AD due to changes of the accretion rate are "reverberated" by BLR and dust torus. The time difference or delay between the flux changes is the light travelling time between the inner parts of the AD to the BLR or dust torus. Therefore the time lag and radius are connected through $\tau = R/c$, where c is the speed of light and R can be the radius of both BLR and dust torus.

This technique is only possible as the different components of the AGN dominate the SEDs at different wavelength and thus we are able to differentiate the variability of individual components. The AD dominates the continuum emission from the UV to the optical. It would be desirable to use the UV variability for reverberation mapping as it mainly originates closest to the SMBH, where the AD temperature is highest. Unfortunately it is impossible to observe at UV wavelength with ground based telescopes due to atmospheric absorption. Hence the variability in the optical is used as a proxy of the UV variability. This has two disadvantages:

Most of the optical flux originates from slightly larger distances to the SMBH and the UV variability could be under- or overestimated. Nonetheless being able to use ground based telescopes justifies this approximation. To determine the response of the BLR, BELs both in the optical and NIR can be used, while the dust dominates the continuum emission at wavelength longer than 1 μm.

Reverberation mapping is only possible if the delay is the dominating timescale (Peterson 1997). The dynamical timescale ($\tau_{\rm dyn} = R/v_{\rm clouds}$) on which the BLR and dust torus are changing their geometry needs to be significantly higher. An upper limit to the cloud velocities can be inferred from the width of BELs around $v_{\rm clouds} \lesssim 0.01\ c$ and therefore $\tau \ll \tau_{\rm dyn}$. Additionally the heating and cooling timescales of the dust need to be instantaneous compared to $\tau_{\rm dust}$ which is satisfied as both are on the order of seconds (Nenkova et al. 2008a). In case of the dust free BLR clouds the relevant timescales are the recombination timescales and the resonance diffusion time scale. At the density expected for BLR clouds the recombination timescale is expected on the order of minutes, while the diffusion timescale is on the order of hours (Peterson 1993). Thus all timescales are indeed significantly smaller than the delays.

Additionally the AD radiation has to originate from a region significantly smaller than the BLR or dust torus. This is certainly satisfied if the heating source is the UV emission of the AD. Lastly the radiation needs to be able to propagate freely between the AD and the outer components. This is satisfied if the AD and the BLR clouds populate only a small part of the total volume. For thin ADs (compare Section 1.5) and the opening angle of the dust torus expected in the unified model of AGN (compare Section 1.2) this is the case.

Both BLR and dust torus are extended structures both in radial direction and in their scale height above the AD plane. This complicates the response of individual clouds, described with the response function, as clouds elevated from the AD plane have a shorter delay, because the light path becomes shorter in this case (compare Fig. 2.1):

$$\tau = \frac{(1 - \sin\theta)R}{c}, \tag{2.1}$$

where θ describes the elevation above the AD plane in a spherical coordinate system. As BLR and dust torus are optically thick only the emission of clouds with positive values of θ are observed. This leads to an underestimation of the radius. The maximum value of θ can be determined using the EW of emission lines. The EW is proportional to how much of the ionizing emission is absorbed by BLR clouds. This way a value of $\theta_{max} \sim 33°$ can be constraint (Korista et al. 1997; Maiolino et al.

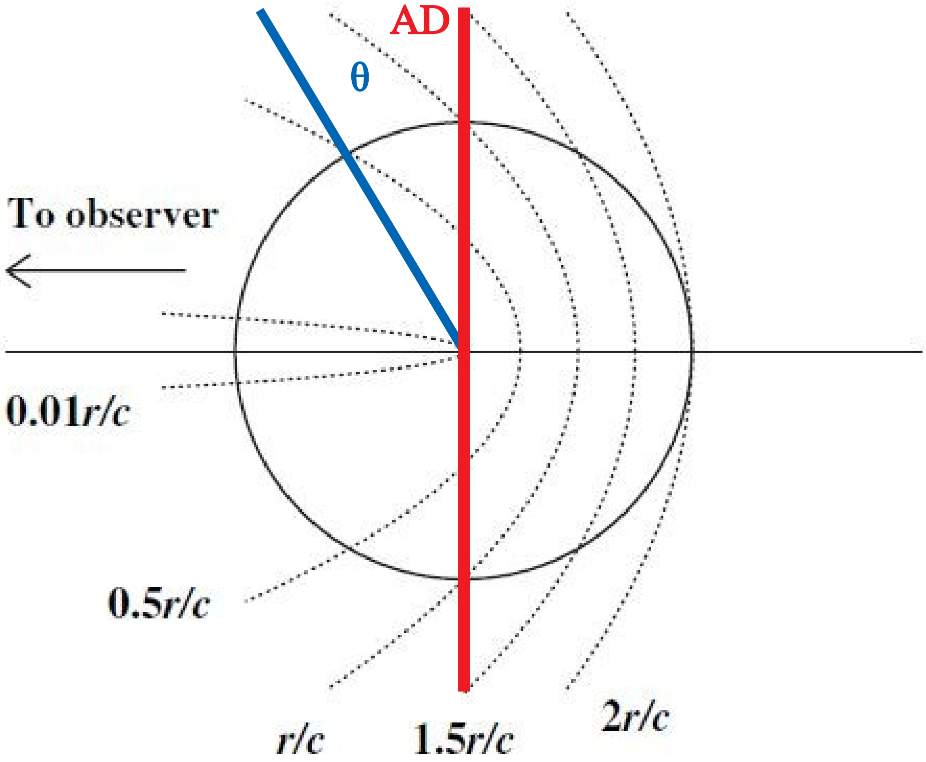

Figure 2.1 Schematic view of the isodelay surfaces (dotted lines) with the respective delays described in Eq. 2.1 as representation of the BLR or dust torus. Figure adapted from Peterson (1993).

2001; Ruff et al. 2012; Baskin et al. 2014) leading to a possible underestimation of the radius by roughly a factor of two. Thus partly explaining the underestimation of radii mentioned in Section 1.6 for the expected radius luminosity relation.

This further complicates when considering different inclinations of the AD plane with respect to the line of sight. As the inclination i increases the clouds located towards the observer will have a further reduced delay, while the delay of the clouds on the opposite side increases. Ignoring the height above the AD we get:

$$\tau = \frac{(1 - \cos\phi \sin i)R}{c}, \tag{2.2}$$

where the azimuthal angle ϕ is zero when the cloud is located towards the observer. This leads to a broadening of the transfer function describing the response of BLR and dust clouds to changes of the AD emission. We can define a transfer function, which can be written as:

$$\Psi(\tau)d\tau = 2\pi\xi Rcd\tau \tag{2.3}$$

with ξ being the responsivity per unit area. With this transfer function we can relate the AD radiation ($F_{\mathrm{AD}}(t)$) to the emission of the BLR or dust torus ($F(t)$) through

$$F(t) = \int \Psi(\tau) F_{\mathrm{AD}}(t-\tau)d\tau. \tag{2.4}$$

With this transfer function the cloud distribution could be reconstructed in principle. However data of extremely good quality with a very high cadence is needed to be able to do this. In reality this can not be achieved and the delay has to be determined by maximizing the cross correlation function

$$CCF(\tau) = \int F(t) F_{\mathrm{AD}}(t-\tau)dt, \tag{2.5}$$

giving the response-time weighted delay corresponding to a radius close to the inner edge of the torus or BLR (Koratkar & Gaskell 1989, 1991). As only discrete values for $F(t)$ and F_{AD} are available from each observation, this equation can not easily be solved. Either the error of the delay depends strongly on the cadence of observations or F_{AD} has to be interpolated to achieve shorter time gaps between values of F_{AD}. Usually the latter is the more practical approach and is used in most reverberation mapping campaigns.

A short summary of the capabilities of reverberation mapping on the BLR, dust torus and AD will be given in the following. Additionally some scientific results are highlighted.

2.1.1 Results for the BLR

Due to the strength of the BELs the first reverberation mapping studies were done with the BLRs (Clavel et al. 1991; Peterson et al. 1991; Dietrich et al. 1993; Maoz et al. 1993). BELs hold the advantage that additional information can be drawn from the shape. Cloud velocities for SMBH mass determination can be constrained from the width of the BELs and the shape of the BELs depends on the geometry and dynamics in the BLR. With velocity resolved reverberation mapping, in other words measuring the delay of only a part of the BEL, it is even possible to measure a velocity resolved delay of BELs (e.g. Bentz et al. 2008; Denney et al. 2009; Grier et al. 2013b; Du et al. 2016).

In most cases optical BELs are used and more specifically the Hα and Hβ lines. The main advantage is that the optical continuum and thus the AD emission is observed in parallel. However Landt et al. (2011b) were able to show that the AD dominates the SED up to a wavelength of $\sim\ 1\,\mu$m. Thus it is possible to do reverberation mapping with NIR spectroscopy without parallel optical observations. While the NIR part of the AD radiation probes slightly larger distances to the SMBH a number of advantages arises from this. In the NIR the emission is less affected by dust extinction due to dust in the host galaxy and the dust emission is probed simultaneously. This enables parallel studies of the BLR and the dust torus without additional observations. Furthermore some of the strongest lines of the Paschen series are less superposed by NELs of other elements compared to the Balmer series simplifying the extraction of BEL fluxes. However most reverberation campaigns on the BLR are still done with optical spectroscopy.

2.1.2 Results for the Dust torus

Slightly later reverberation mapping was applied to the dust torus (e.g. Peterson 1993, 1997; Suganuma et al. 2006). In most cases photometry of two broad bands each representing either the AD emission (usually the V band) and the dust emission (usually the K band) are used. With only two bands the observations can be done quickest but the dust radius is the only information on the dust torus directly available.

In principle the variation of dust emission depends on the temperature and the observed surface area of the dust. The changes of temperature are induced by changes of the UV emission from the AD, while the surface area depends on the geometry of the dust torus. It is therefore desirable to be able to distinguish changes of the temperature and changes of the surface area. With the changes of temperature, it is possible to measure the dust radius. Infrequent changes of the surface area on the other hand are important to understand processes such as dust sublimation or dust creation. It is possible to see when changes of the surface area appear even with only two bands as the response of the dust emission to the AD emission changes, however valuable information on the dust temperature during these changes is not accessible. Only if multiple NIR bands are used the dust temperatures can be determined directly (e.g. Schnülle et al. (2013, 2015)). This way it is possible to draw conclusions on dust properties such as sublimation temperature, composition, grain size, and density. Additionally the temperature is an important property of the radius luminosity relation as the radius is $\propto\ T^{-2.8}$ (compare Eq. 1.15).

2.1.3 Results for the Accretion Disk

It is even possible to use reverberation mapping on the AD only to probe disk models. As the AD temperature decreases with radius a delay between the lightcurves of different UV and optical filters is expected. Such delays were determined for a few AGN (e.g. Wanders et al. 1997; Collier et al. 1998; Edelson et al. 2015; Pozo Nuñez et al. 2019). However both the use of broad band filters, and thus contributions by BELs, and insufficient time sampling lead to large uncertainties. These uncertainties can be reduced using narrow-band filters and high-cadence time samplings (Pozo Nuñez et al. 2017, 2019). Still the results are largely consistent with the $\tau \propto \lambda^{4/3}$ relation expected for thin disk models introduced by Shakura & Sunyaev (1973) although the outer radii of the ADs are larger than expected. These larger AD sizes are also found using microlensing of luminous quasars (e.g. Pooley et al. 2006, 2007; Morgan et al. 2010; Chartas et al. 2016).

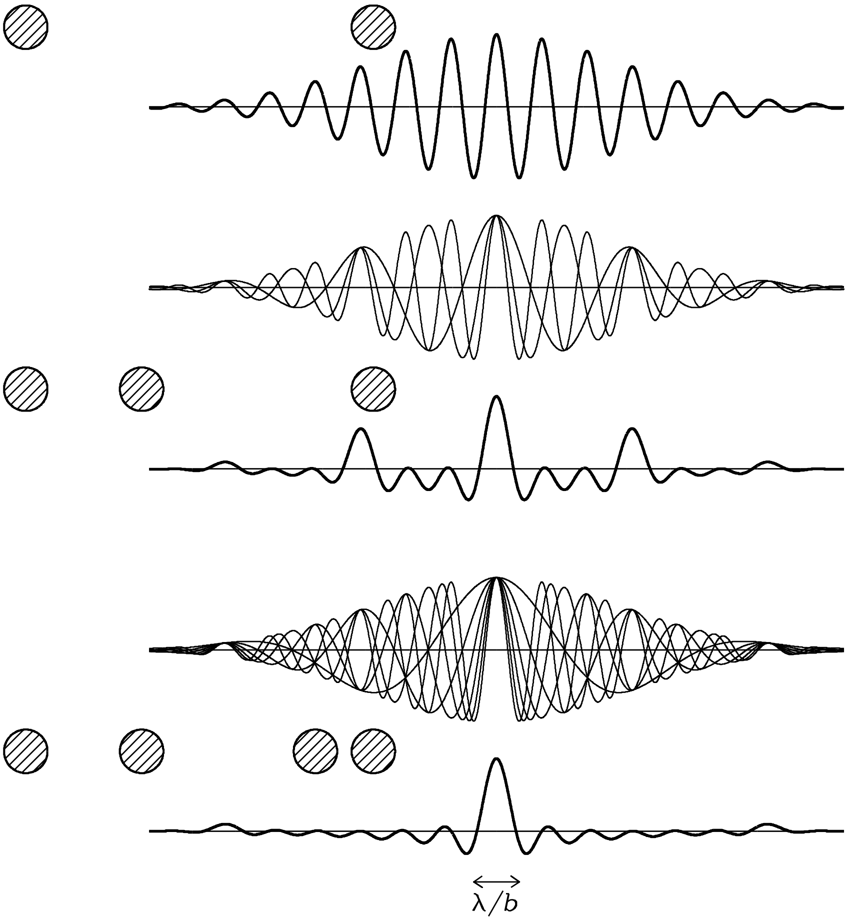

Figure 2.2 Interference patterns for interferometers using two (top), three (middle) and four (bottom) telescopes. For the cases with three and four telescopes the interference patterns for each possible baseline and the combined pattern are shown. The width of the narrow peaks is set by the size of the baseline b while the enveloping intensity pattern is set by the diameter of the telescopes. With increasing number of telescopes the main peak of the synthesized beam converges to a gaussian function with a resolution λ/b while the neighbouring peaks are suppressed. Figure Credit: NRAO.

2.2 Interferometry

The basic idea behind interferometry is to use multiple telescopes simultaneously to increase the spatial resolution. With this approach the diameter of the primary mirror of the telescope is no longer limiting the resolution but the longest baseline between telescopes. This is important as (especially optical) telescopes with huge diameters are both extremely expensive and technically difficult or even impossible to construct. To resolve the inner structures of AGN, optical and NIR interferometry is needed and we therefore will not discuss radio interferometry here.

The theoretical foundation was laid by the two-slit experiment developed by Thomas Young in 1803: If a monochromatic light source is placed in front of two slits an interference pattern will appear behind the screen due to the wave nature of light. With simple geometric considerations we can determine the distance between two points with constructive interference at $\Delta\Theta = \lambda/b$, with b the separation of the two slits. If now two point sources are put in front of the slits the interference will be destructive if the point sources are separated by $\lambda/2b$. For astronomic observations the slits of the interferometer are replaced by telescopes and thus the separation of the slits can be replaced with the maximum separation of telescopes. The definition of the spatial resolution is slightly arbitrary (as it is for single dish telescopes as well). Usually the resolution is defined somewhere between the separation for constructive (λ/b) and destructive ($\lambda/2b$) interference. Most of the time the constructive interference is used.

The first applications of interferometers in astronomy date back to the 19. century. Michelson (1891) was able to determine the angular sizes of Jupiter's moons and later to determine the angular size of a star other than the sun for the first time (Michelson & Pease 1921).

After these first results using optical interferometry it took some time until the resolution and sensitivity, needed to measure sizes of the dust torus or the BLR, could be reached. There are a number of technical problems which had to be resolved before the necessary advancements in optical interferometry could be made. Most of all the precision of the instrumentation needs to be much higher at shorter wavelength. Additionally the sensitivity is limited by turbulence in the atmosphere. Therefore the integration time and aperture size are limited by atmospheric turbulence reducing the sensitivity significantly. With the development of adaptive optics for optical telescopes it is possible to correct for the effects of atmospheric turbulence allowing the use of large telescopes and long integration times. To further increase the sensitivity, more than two telescopes and thus different baselines are used. The basic idea behind this is illustrated in Fig. 2.2. For a single baseline the intensity difference between the main peak and the neighbouring peaks is small if the baseline of the interferometer is significantly larger than the diameter of the individual telescopes. If multiple baselines are used, the main peak of the synthesized beam converges quickly to a gaussian function with a resolution of λ/b and the neighbouring peaks are suppressed.

Relatively recently it was possible to measure distances of the BLR, dust torus and even AD at the center of galaxies. These results will be shortly presented.

2.2.1 Results for the BLR

The radius of a BLR was measured for the first time using interferometry by Gravity Collaboration et al. (2018) using the Very Large Telescope Interferometer (VLTI). Photocenter offsets between the blue and red part of the broad Paβ line of the relatively nearby quasar 3C273 were determined with a spatial resolution of 10^{-5} arcseconds. Apart from the radius determination, and thus also SMBH mass determination, a number of assumptions for the unified model of AGN (compare Section 1.2) and for the mass estimations of SMBHs could be verified: The BLR clouds are orbiting the SMBH and the rotation axis aligns with the radio jet axis. Geometrically the data is well fit with a gravitationally bound thick disk model of the BLR.

2.2.2 Results for the dust torus

For the dust torus there is a larger variety of radius measurements (Swain et al. 2003; Kishimoto et al. 2009; Pott et al. 2010; Weigelt et al. 2012; Gravity Collaboration et al. 2020; GRAVITY Collaboration et al. 2019). Compared to the radii determined with reverberation mapping these are systematically larger but also show the expected behaviour of larger radius for larger AD luminosity. As reverberation mapping gives the innermost radius of the dust, while interferometry gives the radius of the peak emission, this is expected.

Apart from the dust radius, Kishimoto et al. (2009) were able to estimate a graphite dominated dust composition and grain sizes larger than $\sim 0.05\ \mu$m. Gravity Collaboration et al. (2020); GRAVITY Collaboration et al. (2019) were able to determine upper limits to the BLR sizes smaller than the dust torus sizes and additional torus parameters such as the height or inclination.

2.2.3 Results for the Accretion Disk

For completeness we also mention the first image of a SMBH at the center of M87 by Event Horizon Telescope Collaboration et al. (2019). While the main goal was the image of the SMBH, it meant also imaging the innermost part of the AD. At a wavelength of 1.3 μm a global array with telescopes in Europe, Antarctica, North and South America were used leading to a longest baseline of almost 11,000 km. Apart from determining the mass of the SMBH predictions of the general theory of relativity. It was found that the image is consistent with predictions for a rotating black hole.

CHAPTER 3

Multiwavelength dust reverberation mapping of nearby Active Galactic Nuclei

3.1 Introduction

In this chapter we present our results from a reverberation mapping campaign (theoretical background introduced in Section 2.1) based on a four year observing program between October 2012 and March 2016 of 25 AGN using multiple broad-band filters both in the optical and in the NIR. In most reverberation mapping campaigns only a single optical and IR band (mostly V and K respectively) are used to measure the delay. If multiple bands are used it is possible to constrain the lag times of the dust simultaneously with the dust temperature, allowing a temperature normalization of the radius luminosity relation introduced in Section 1.6. Furthermore, information about the dust temperature is useful to determine dust properties such as the grain size and to differentiate between grain types (Barvainis 1987; Koshida et al. 2009). In addition to the temperature it is also possible to constrain the surface area of the dust and find intrinsic differences in the geometry of dust tori.

The chapter is structured in the following way: In Section 3.2 we will describe our observational strategy and the time sampling of the different AGN. The data reduction from raw images to AGN fluxes is described in Section 3.3 followed by the introduction of our AGN model describing the AGN SED and the implementation of that model in Section 3.4. Subsequently the resulting fit parameters are described and discussed in Section 3.5 and Section 3.6 respectively. A summary of our results and some concluding remarks are given in Section 3.7.

3.2 Observations

We observed 25 type 1 AGN using the Gamma-Ray Burst Optical and Near-Infrared Detector (GROND, Greiner et al. 2008) between October 2012 and March 2016. An overview over the basic information of the targets and their observation epochs is given in Table 3.2. GROND is mounted on the MPG 2.2m telescope at ESO in La Silla and is designed to observe the afterglows of gamma-ray bursts. Therefore it is capable of simultaneous photometric observations in seven passbands in the optical and near-infrared. These simultaneous imaging capabilities are also suitable for determining the SEDs of variable objects such as AGN. In the case of our hot dust reverberation campaign the spectral range from the optical to the NIR enables us to observe both the AD (dominant in the optical) and the hot dust (dominant in the NIR) and thus differentiate between the variations of these two components of the AGN. The different photometric bands of GROND are separated using dichroics. Each of the four optical (g', r', i', z') 2048×2048 pixel detectors has a field of view of $5.4' \times 5.4'$ while the three NIR (J, H, K) 1024×1024 pixel detectors have a field of view of $10.0' \times 10.0'$.

Of the 25 targets in our sample, six were observed starting in October 2012 while the monitoring of the rest of the targets started in May 2014. Depending on the optical luminosity, and hence the expected hot dust reverberation delay, of each target the sampling for each target was scheduled between two to four weeks although the variation in the achieved sampling was often higher. Furthermore there are data gaps depending on the visibility of the AGN from La Silla.

At the beginning of our observations, we observed each target with seven dither steps of the target size. For the most extended host galaxies this step size was $3.75'$ and thus the target was not included in some of the exposures. Therefore the observing strategy was changed in May 2015. Now the median sky image was created separately in a field without extended sources close to our targets and the dither step for each of the five science and sky exposures was reduced to $18''$.

Table 3.1 Overview of the GROND observations of the AGN in our sample.

Object	RA (J2000)	DEC (J2000)	z	Class	opt. catalog	# obs.	first observation	last observation
3C273	12 29 06	+02 03 08	0.158	S1.0	SDSS	13	Feb 2013	Feb 2016
Ark 120[b]	05 16 11	-00 08 59	0.033	S1.0	SDSS	26	Oct 2012	Feb 2015
CTSJ 13.12	13 51 29	-18 13 46	0.012	S1n	GAIA	9	May 2014	Feb 2016
ESO 323-G77	13 06 26	-40 24 52	0.015	S1.2	GAIA	5	Jan 2015	Feb 2016
ESO 362-G18	05 19 35	-32 39 27	0.013	S1.5	GAIA	18	Sep 2014	Mar 2016
ESO 377-G24	11 12 33	-36 25 32	0.010	S1.0	GAIA	6	Dec 2014	Feb 2016
ESO 383-G035	13 35 53	-34 17 44	0.008	S1.5	GAIA	8	May 2014	Mar 2016
Fairall 51	18 44 53	-62 21 52	0.014	S1.5	GAIA	8	Sep 2014	Feb 2016
H 0557-385	05 58 02	-38 20 04	0.034	S1.2	GAIA	16	Sep 2014	Mar 2016
H 1934-063	19 37 33	-06 13 04	0.010	S1.5	GAIA	4	Sep 2014	Sep 2015
H 2107-097	21 09 09	-09 40 14	0.027	S1.2	SDSS	9	Sep 2014	Oct 2015
HE 1228+013	12 30 50	+01 15 22	0.118	S1n	SDSS	12	Jan 2013	Jan 2015
IC 355	03 53 46	+19 58 26	0.029	S1.0	GAIA	10	Sep 2014	Feb 2016
MCG-01.13.025	04 51 41	-03 48 33	0.013	S1.2	SDSS	10	Sep 2014	Mar 2016
Mrk 1239	09 52 19	-01 36 43	0.020	S1n	SDSS	5	Dec 2014	Mar 2016
Mrk 50	12 23 24	+02 40 44	0.023	S1.2	SDSS[a]	6	Jun 2014	Feb 2015
Mrk 590	02 14 33	-00 46 00	0.027	S1.0	SDSS	32	Oct 2012	Jan 2016
Mrk 704	09 18 25	+16 18 19	0.029	S1.2	SDSS	6	Nov 2014	Mar 2016
NGC 1019	02 38 27	+01 54 27	0.024	S1.5	SDSS	15	Sep 2014	Jan 2016

Object	RA (J2000)	DEC (J2000)	z	Class	opt. catalog	# obs.	first observation	last observation
NGC 3227[b]	10 23 30	+19 51 54	0.003	S1.5	SDSS	17	Nov 2012	Feb 2015
NGC 3783	11 39 01	-37 44 18	0.009	S1.5	GAIA	13	May 2014	Mar 2016
NGC 4235	12 17 09	+07 11 29	0.007	S1.2	SDSS	5	Jun 2014	Mar 2016
NGC 4593	12 39 39	-05 20 39	0.009	S1.0	GAIA	6	Jun 2014	Mar 2016
NGC 5548[b]	14 17 59	+25 08 12	0.017	S1.5	SDSS	6	Feb 2014	Jul 2014
UGC 3223	04 59 09	+04 58 30	0.018	S1.5	GAIA	8	Sep 2014	Dec 2015

Notes. Given are the object names, coordinates, redshift, AGN class (from Véron-Cetty & Véron 2010), the catalog used for the flux calibration, number of observation epochs, and the beginning and end of the observations. Fluxes could not be determined during every epoch in every filter due to malfunctions in the specific detector.

[a] In the case of Mrk 50 the i' band magnitude of one of the reference stars is wrong in Sloan Digital Sky Survey (SDSS). For this star the i' band magnitude was determined using GAIA.

[b] AGN already included in Schnülle (2017).

3.3 Data reduction

All images were reduced using the pipelines developed by R. Decarli and G. De Rosa (cited in Morganson et al. 2012) which make use of IRAF routines. In the first steps the bias/dark was subtracted and subsequently a flatfield correction was applied to every image. Thereupon a median sky image was subtracted which was created by stacking dithered images without realignment. In the setup used until the May 2015 (described in Section 3.2) the dithersteps had to be larger than the size of the host galaxies of our targets. Therefore from May 2015 separate sky exposures were taken without any extended sources and the size of the dithersteps could be reduced to 18″. Afterwards the science exposures were realigned and combined.

The AGN fluxes were than extracted for each filter and epoch using GALFIT described by Peng et al. (2002). GALFIT enables us to separate the various host galaxy components and the point spread function (PSF) of the AGN emission. There are two main issues which can arise in the AGN flux extraction using GALFIT: First if the AGN is very bright our images are sometimes not deep enough to detect the disk or bulge component as otherwise we would have saturation effects for the AGN component. However in this case the flux of the AGN dominates the other galaxy components so the error of the AGN fluxes arising from this is small. A second problem can arise if the effective radius of bulge components is smaller than approximately a couple of pixels leading to degeneracies between the bulge and AGN components. This can happen either for galaxies with very small bulges or for the more distant of our galaxies. Again the AGN flux should dominate in both cases either because the bulge fluxes are low or for the more distant galaxies the AGN fluxes are relatively high for our sample.

Simultaneously to the extraction of the AGN flux, fluxes of reference stars were determined by fitting a PSF model in GALFIT to nearby stars. For the absolute flux calibration in the NIR JHK, we used bands the Two Micros All Sky Survey (2MASS) (Skrutskie et al. 2006). In the optical $g'r'i'z'$ bands, the SDSS (Alam et al. 2015) was used if our target was located within the sky coverage of SDSS. Otherwise photometric data from Gaia DR2 (Gaia Collaboration et al. 2016, 2018; Evans et al. 2018) was used as indicated in Table 3.2. The magnitudes from Gaia were converted to the SDSS $g'r'i'$ bands using the conversion relations as provided by Evans et al. (2018). In the case of one reference star (J122326.82+024004.5) used for Mrk 50 the i' band flux given by SDSS had to be corrected probably due to an error in SDSS. While in SDSS an i' band magnitude of 14.776 mag are given both the SED from the rest of the SDSS magnitudes and the Gaia DR2 results agree

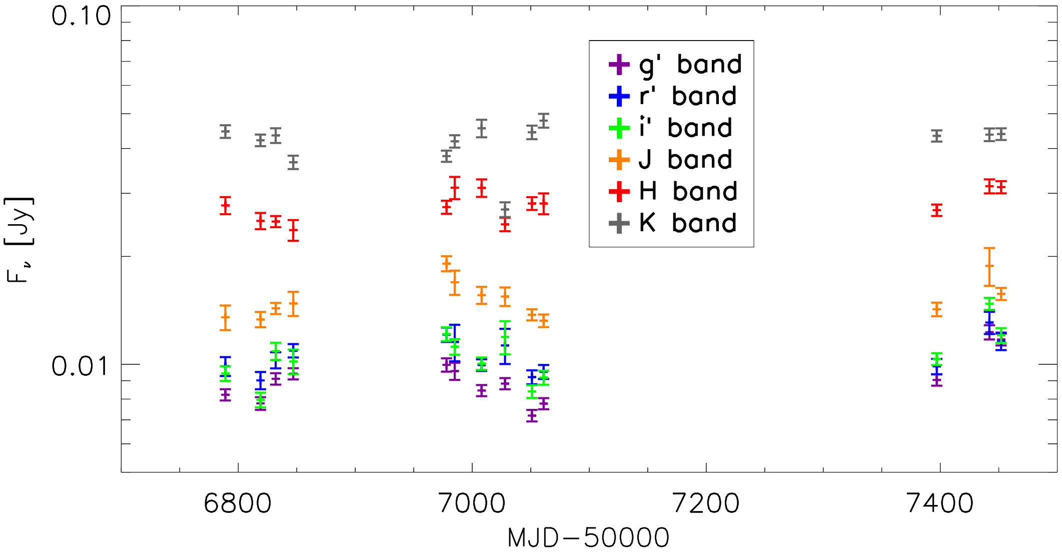

Figure 3.1 Nuclear fluxes of NGC 3783 between May 2014 and March 2016, derived with GALFIT (Peng et al. 2002).

very well with a value of 13.000 mag. We decided not to make an interpolation to the z' band using a blackbody fit of the reference stars. The temperature parameter in the later model is highly dependent on the z' band flux and therefore errors made in the interpolation can have a significant influence on the measured temperature.

Furthermore the measured fluxes had to be corrected for foreground Galactic extinction due to dust within the line of sight in our Galaxy. This was done using the Schlafly & Finkbeiner (2011) recalibration of the Schlegel et al. (1998) dust map as provided by the NASA/IPAC Extragalactic Database (NED).

In a next step we have to correct our fluxes for the contamination of emission lines mainly arising in the BLR and NLR of AGN. As there are no spectra available for most of our AGN we have to use the equivalent width of typical AGN emission lines in the optical, which were derived using a composite spectrum of many AGN by Blandford et al. (1990). These corrections are: $g' \approx 20\%$, $r' \approx 25\%$, $i' \approx 0\%$, and $z' \approx 3\%$. In the NIR we used the corrections derived for NGC 4151 by Schnülle et al. (2013) of $J \approx 15\%$, H and K $\approx 2\%$. The resulting fluxes of NGC 3227 are shown in Fig. 3.1. It can be seen that all optical and the J band flux are dominated by the AD radiation as they follow the same time evolution, while the H and K band do not follow this time evolution as they are dominated by radiation originating from the dust (compare the SEDs of NGC 3783 in Fig. 3.4). The resulting AGN fluxes for each source will be made available electronically.

Some of our AGN are affected by dust extinction most likely due to dust within the host galaxy. This dust extinction results in an optical SED which differs from the usual power law arising from the AD. In these cases we apply a dereddening factor in our model (described later in more detail in Section 3.4). The effect of this correction is very prominent in the SEDs in Fig. 3.6 for Mrk 1239 where the gray squares indicate the reddened flux while the green squares show the flux resulting from our host extinction correction. Whether this correction had to be made for a specific AGN and the degree of reddening can be seen in Table 3.5.1. As the reddening is strongly correlated with most model parameters, especially those of the AD since dust extinction is stronger at optical wavelength, we make a Markov Chain Monte Carlo (MCMC) run with dust reddening correction and afterwards do a second run with a fixed best fit value of B-V.

3.4 Model for reverberation mapping

Reverberation mapping in general is used to derive the delay of the response of outer parts of the AGN, such as BLR or dust torus, to flux changes (caused by changes of the accretion rate) in inner parts like the AD and thus derive the spatial scales of AGN structures. In our case, we use changes of the flux at optical wavelength as a proxy for the AD luminosity (although the main heating source of the dust is the UV radiation of the AD) and relate this to changes in the NIR, where the hot dust dominates the SED. The distance between the hot dust and AD will be given as the light travelling time between those two components. This delay translates into a radial distance by the relation $\tau = R_{\mathrm{dust}}/c$ where R_{dust} is defined as the radial distance to the innermost part of the AD and c is the speed of light. All timescales in this chapter will be given in units of days if not stated otherwise.

In this section, we will describe the model used in this chapter and how we implement it. First the model itself will be described, followed by a description of the interpolation of the AD signal, and finally the implementation of the model in the MCMC.

3.4.1 Accretion disk and dust model

We use a very simple two component model. The AD radiation is described by a powerlaw with $F \propto \lambda^{-\alpha}$ with $\alpha > 0$ and the hot dust emission is described by single blackbody function:

$$F_\lambda(t,\vec{x}) = C_1 \cdot F_g(t) \cdot \left(\frac{\lambda}{\lambda_0}\right)^{-\alpha} + C_2 \cdot BB_\lambda(T(\nu,t)). \tag{3.1}$$

$\vec{x}$ denotes our full set of model parameters. The AD radiation (left hand side of Eq. 3.1) is scaled by the constant C_1 and the flux $F_g(t)$ in the g' band and $\lambda_0 = 1$ μm. The blackbody function on the right hand side of Eq. 3.1 has the form:

$$BB_\lambda(T) = \frac{2hc^2}{\lambda^5}\frac{1}{e^{hc/\lambda k_{\mathrm{B}}T} - 1}, \tag{3.2}$$

where T is the blackbody temperature and C_2 the blackbody constant, a mixture of the emissivity and surface area of the hot dust. In order to describe the time evolution of the hot dust temperature, we use the g' band signal again to approximate the changes of the AD radiation. The increase of the AD luminosity heats up the dust after the time lag τ and therefore, the starting temperature $T_0 = T(\tau)$ evolves for $t > \tau$ as

$$\mathrm{dT(t)/T(t)} = \nu \cdot \frac{1}{4} \cdot \mathrm{dF_g(t-\tau)/F_g(t-\tau)}. \tag{3.3}$$

The temperature evolution can be derived within the blackbody limit and an absorption efficiency $Q_{\mathrm{eff}} = 1$ from the Stefan-Boltzmann law. The variability factor ν takes into account that not all changes of the g' band signal might be reprocessed by the hot dust (Hönig & Kishimoto 2011) and therefore the variability factor would be smaller than 1. Furthermore values of $\nu \neq 1$ might indicate that the changes of the g' band signal under- or overestimate the changes in the UV, which is more important for the heating of the hot dust as mentioned above. The variation of T is started at $t > \tau$. Observations with $t < \tau$ the NIR fluxes are not included in the MCMC.

Thus the parameter vector consists of six parameters: $\vec{x} = (C_1, C_2, T_0, \tau, \alpha, \nu)$. In general degeneracies are only seen between parameters describing the same component (C_1 and α the AD and C_2 and T_0 the hot dust).

3.4.2 Interpolation of the accretion disk signal

In order to calculate a continuous $T(t)$ using Eq. 3.3 for any dust delay τ an interpolation of the g' band signal is needed. This is done using the method for interpolation, realization, and reconstruction of noisy irregularly sampled data developed by Rybicki & Press (1992). Within this methodology the AD signal is described as a stochastic process which is characterized by two parameters of a structure function:

$$V(\tau) = A^2 \cdot \left(\frac{\tau}{1\mathrm{yr}}\right)^{\gamma}. \tag{3.4}$$

A describes the average flux variation on a one year timescale and γ is the gradient of the variability of the AD. In Fig. 3.2, this structure function is shown for NGC 3783. The flux difference between flux measurements in the g' band $\sqrt{v_{ij}}$ is plotted against the time difference between the corresponding measurements τ_{ij}. For NGC 3783 we have 13 observations leading to 78 values for v_{ij}. For better visibility in Fig. 3.2 we binned those 78 values into 15 bins with an equal width of τ_{ij}. The best fit values for the structure function (solid green line) are $A = 0.0014 \pm 0.0002$ Jy and $\gamma = 0.45 \pm 0.17$ in the particular case of NGC 3783.

Making use of the above parameters we can estimate the g' band lightcurve. The result of the interpolation is shown in Fig. 3.3 (blue solid line) along with the estimated uncertainty (gray area). A more detailed description of the methodology used for the interpolation is given by Schnülle et al. (2015).

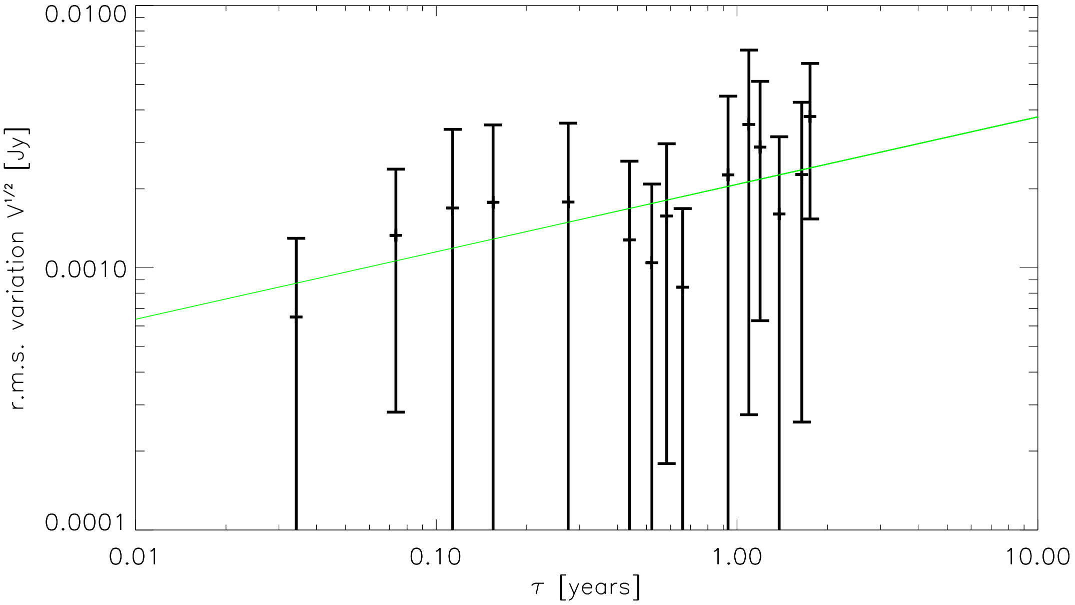

Figure 3.2 Plotted are rebinned flux differences $(v_{ij})^{1/2}$ against time differences τ_{ij} (black crosses) calculated from our g' band data from NGC 3783. The power law structure function as given in Eq. 3.4 is shown as the green solid line with the best fit parameters $A = 0.0014 \pm 0.0002$ Jy and $\gamma = 0.45 \pm 0.17$.

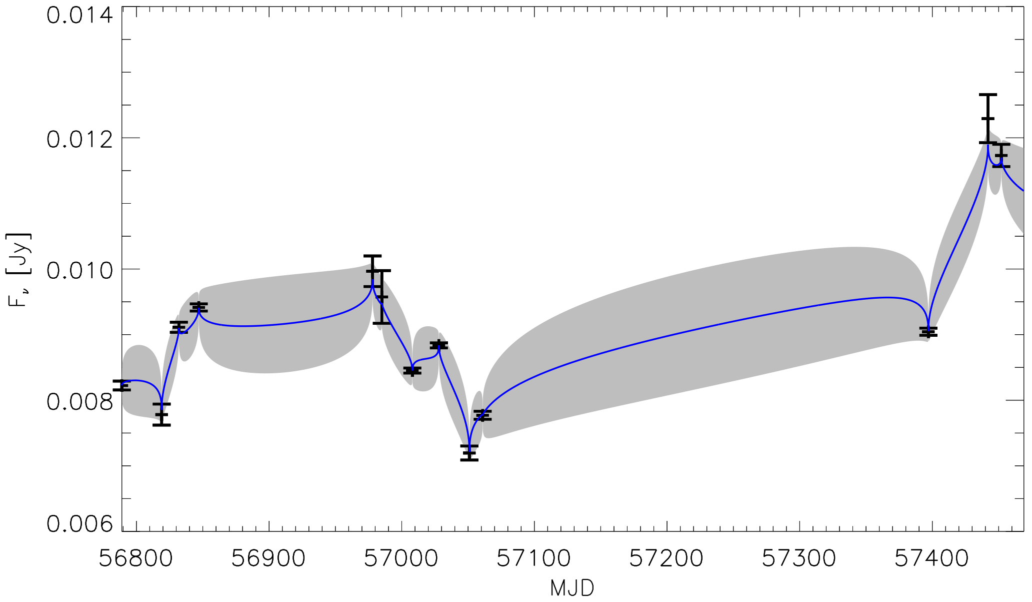

Figure 3.3 Interpolation of the g' band lightcurve using the method of Rybicki & Press (1992) and Press et al. (1992) for NGC 3783. The black crosses indicate our measured g' band fluxes with their uncertainties, the blue solid line the interpolated lightcurve and the gray area the estimated uncertainty of the interpolation.

3.4.3 Implementation of model

In order to fit the model described in Section 3.4.1 and 3.4.2 to the lightcurves of our AGN a Differential Evolution Markov Chain (DE-MC) algorithm developed by Ter Braak (2006). DE-MC is in principle a population MCMC algorithm but runs multiple chains in parallel. After every iteration step the algorithm evaluates the posterior probability density function for every chain,

$$\vec{p}(\vec{x}|\vec{y}) \propto \vec{p}(\vec{x}) \cdot \exp\left(-\frac{1}{2}\sum_{k=1}^{N}\left(\frac{m_k - y_k}{\sigma_k}\right)^2\right). \tag{3.5}$$

In this equation $\vec{x}$ is the parameter vector from Section 3.4.1, $\vec{y}$ the data, m_k the value of the model for the kth data point, y_k the value of the kth data point, and σ_k the uncertainty of the corresponding photometric error. N refers to the number of data points of the specific AGN in the optical and NIR which is up to seven times the number of observations of the AGN as given in Table 3.2. We use priors $\vec{p}(\vec{x})$ to exclude unphysical parameter ranges. This way end up with a posterior probability density function for every parameter in our model ($\vec{p}(\vec{x}|\vec{y})$). More details on this algorithm are given by Ter Braak (2006) and Schnülle et al. (2015).

3.5 Reverberation mapping results

In this chapter we will describe our reverberation mapping results. First in Section 3.5.1 we will show the outcome of our very simple model described in Chapter 3.4. In general our model describes the signal very well in the optical, it shows higher values of χ^2 in the NIR. As the model does not include effects like changes of the dust radius or the dust surface area this is not surprising. At least in the BLR such changes in the geometry were found and are likely present in the dust torus as well (see also Chapter 4).

Additionally there are some issues with individual AGN which are commented on in Section 3.5.2. Mostly these sources have NIR fluxes which are not well fit by our model or the cadence and distribution of observations of that particular AGN does not allow the determination of some parameters. In Section 3.5.3 our measured delays will be compared to the radii determined using interferometry.

3.5.1 Sample results

Our sample of AGN can be divided into two major categories by their optical SEDs. Some clearly show a power law behaviour in the optical as expected for radiation from an AD. However for approximately half of our AGN we do not see this power law. This is most likely caused by dust within the host galaxy absorbing parts of the radiation. For these sources we add a reddening correction to our model as described in Section 3.3. The value of the reddening correction B-V is listed in Table 3.5.1 along with the other model parameters. In the following these two groups will be described and compared.

AGN without host extinction

In Fig. 3.4 SEDs of NGC 3783 are shown as an example of an AGN without host extinction (green squares). The chosen observing epochs are the fourth to the seventh, which are the first epochs for which the time difference to the first epoch is larger than the determined time lag of the dust ($t > \tau$). Therefore these are the first observing epochs with a varying dust temperature. For the first three epochs we cannot determine a variation of the temperature as we do not have the according information of the AD flux variation. The SEDs can be fit very well with a power law in the optical (blue line) and a blackbody function (red line) in the NIR to get a proper total fit of our data (black line). At the top of each plot in Fig. 3.4 the dust temperature of the epoch ($T(t)$) is shown.

Table 3.2 Overview of the fit parameters for our single blackbody model (Eq. 3.1), the host extinction correction B-V, and the variability of the AD signal F_{var}.

Object	$C_1 \cdot F_g(0)$	C_2	$\langle T \rangle$	τ	α	ν	B-V	F_{var}[a]
	10^{-13} $\mathrm{Wm^{-2}\mu m^{-1}}$	10^{-18} sr	K	days				
AGN with full set of parameters (cf. Section 3.5.1 and 3.5.2)								
3C273	$0.091^{+0.005}_{-0.005}$	$0.38^{+0.05}_{-0.04}$	1932^{+50}_{-49}	702^{+110}_{-104}	$2.70^{+0.07}_{-0.07}$	1.0	< 0.3	0.10
Ark 120	$0.25^{+0.01}_{-0.01}$	$0.51^{+0.02}_{-0.02}$	1701^{+20}_{-20}	108^{+1}_{-1}	$1.77^{+0.03}_{-0.03}$	$1.06^{+0.05}_{-0.05}$	< 0.3	0.14
ESO 323-G77	$1.73^{+0.08}_{-0.08}$	$0.75^{+0.10}_{-0.09}$	1925^{+60}_{-57}	213^{+62}_{-33}	$4.38^{+0.07}_{-0.07}$	1.0	$1.16^{+0.37}_{-0.37}$	0.19
ESO 362-G18	$0.245^{+0.003}_{-0.003}$	$0.69^{+0.12}_{-0.10}$	1040^{+21}_{-20}	39^{+1}_{-1}	$1.98^{+0.02}_{-0.02}$	$0.64^{+0.03}_{-0.03}$	< 0.3	0.45
Fairall 51	$1.35^{+0.04}_{-0.04}$	$1.11^{+0.18}_{-0.15}$	1480^{+45}_{-45}	147^{+63}_{-56}	$3.04^{+0.06}_{-0.06}$	1.0	$0.78^{+0.29}_{-0.29}$	0.08
MCG-01.13.025	$1.71^{+0.03}_{-0.03}$	$0.094^{+0.008}_{-0.008}$	1781^{+35}_{-34}	32^{+11}_{-11}	$3.18^{+0.04}_{-0.04}$	1.0	$0.87^{+0.10}_{-0.10}$	0.10
Mrk 1239	$1.20^{+0.04}_{-0.04}$	$1.68^{+0.18}_{-0.16}$	1521^{+31}_{-31}	43^{+70}_{-16}	$1.68^{+0.06}_{-0.06}$	1.0	$0.43^{+0.13}_{-0.12}$	0.04
Mrk 50	$0.425^{+0.007}_{-0.008}$	$0.12^{+0.09}_{-0.06}$	1220^{+137}_{-108}	44^{+11}_{-9}	$1.23^{+0.03}_{-0.03}$	1.0	< 0.3	0.22
Mrk 590	$1.64^{+0.03}_{-0.03}$	$0.019^{+0.002}_{-0.002}$	1816^{+59}_{-63}	78^{+1}_{-1}	$2.02^{+0.03}_{-0.03}$	1.0	$0.61^{+0.05}_{-0.05}$	0.30
NGC 3227	$0.24^{+0.01}_{-0.01}$	$0.50^{+0.06}_{-0.06}$	1607^{+49}_{-49}	41^{+2}_{-2}	$1.99^{+0.04}_{-0.04}$	$0.63^{+0.12}_{-0.12}$	$0.34^{+0.09}_{-0.09}$	0.17
NGC 3783	$0.274^{+0.005}_{-0.005}$	$0.74^{+0.07}_{-0.06}$	1418^{+25}_{-28}	88^{+38}_{-12}	$1.78^{+0.03}_{-0.03}$	$0.44^{+0.20}_{-0.20}$	< 0.3	0.16
NGC 4235	$3.24^{+0.07}_{-0.07}$	$0.39^{+0.06}_{-0.05}$	1506^{+45}_{-45}	45^{+24}_{-19}	$3.31^{+0.05}_{-0.05}$	1.0	$1.04^{+0.17}_{-0.15}$	0.15
NGC 5548	$0.46^{+0.01}_{-0.01}$	$0.64^{+0.1}_{-0.1}$	1391^{+40}_{-40}	79^{+4}_{-4}	$1.50^{+0.02}_{-0.02}$	$0.97^{+0.07}_{-0.07}$	< 0.3	0.13
UGC 3223	$8.0^{+0.2}_{-0.2}$	$0.079^{+0.011}_{-0.010}$	1652^{+47}_{-47}	77^{+27}_{-25}	$3.88^{+0.04}_{-0.04}$	1.0	$1.50^{+0.12}_{-0.12}$	0.06

Object	$C_1 \cdot F_g(0)$ 10^{-13} Wm$^{-2}\mu$m^{-1}	C_2 10^{-18} sr	$\langle T \rangle$ K	τ days	α	ν	B-V	F_{var}[a]
AGN without good delay determination (cf. Section 3.5.2)								
ESO 383-G035	$5.36^{+0.11}_{-0.12}$	$2.2^{+0.5}_{-0.4}$	1264^{+43}_{-42}	-	$3.29^{+0.04}_{-0.04}$	-	$1.25^{+0.13}_{-0.11}$	$\sigma_{g'} < \delta_{g'}$
H 0557-385	$3.01^{+0.03}_{-0.03}$	24^{+5}_{-4}	871^{+19}_{-19}	> 530	$1.59^{+0.02}_{-0.02}$	1.0	$0.69^{+0.05}_{-0.05}$	0.05
H 1934-063	$0.299^{+0.007}_{-0.007}$	$0.69^{+0.15}_{-0.12}$	1338^{+46}_{-47}	-	$1.65^{+0.05}_{-0.04}$	-	< 0.3	$\sigma_{g'} < \delta_{g'}$
H 2107-097	$0.637^{+0.009}_{-0.009}$	$1.35^{+0.16}_{-0.14}$	1164^{+21}_{-21}	> 400	$4.74^{+0.03}_{-0.03}$	1.0	$0.93^{+0.10}_{-0.09}$	0.20
Mrk 704	$0.396^{+0.008}_{-0.009}$	$1.1^{+0.3}_{-0.2}$	1226^{+50}_{-47}	> 60	$1.24^{+0.05}_{-0.05}$	1.0	< 0.3	0.16
NGC 4593	$0.113^{+0.004}_{-0.004}$	$0.24^{+0.02}_{-0.02}$	1517^{+20}_{-19}	-	$3.03^{+0.06}_{-0.06}$	-	< 0.3	0.24
AGN not fitting our model (cf. Section 3.5.2)								
CTSJ 13.12	$0.049^{+0.008}_{-0.007}$	$0.007^{+0.001}_{-0.001}$	2702^{+63}_{-64}	-	$4.0^{+0.2}_{-0.2}$	-	< 0.3	$\sigma_{g'} < \delta_{g'}$
ESO 377-G24	$1.090^{+0.013}_{-0.013}$	-	-	-	$3.81^{+0.02}_{-0.02}$	-	$0.89^{+0.04}_{-0.04}$	$\sigma_{g'} < \delta_{g'}$
HE 1228+013	-	-	-	-	-	-	-	0.26
IC 355	$0.201^{+0.014}_{-0.014}$	$0.0061^{+0.0002}_{-0.0002}$	2405^{+30}_{-29}	> 120	$2.16^{+0.09}_{-0.10}$	$0.28^{+0.15}_{-0.14}$	< 0.3	0.14
NGC 1019	-	-	-	-	-	-	-	-

Notes. For the dust temperature the mean temperature $\langle T \rangle$ was given and not the initial temperature T_0 as the mean temperature will be used in the rest of the chapter. If $\sigma_{g'} < \delta_{g'}$ is given for F_{var} the uncertainty of the photometric measurements are larger than the standard deviation of the AD signal. The AGN were sorted into three groups according to how well our model worked for them. For some delays only lower boundaries could be determined, while other delays could not be determined at all (as well as some other parameters) due to different reasons discussed in Chapter 3.4.

[a] Compare Eq. 3.6 for a definition of F_{var}.

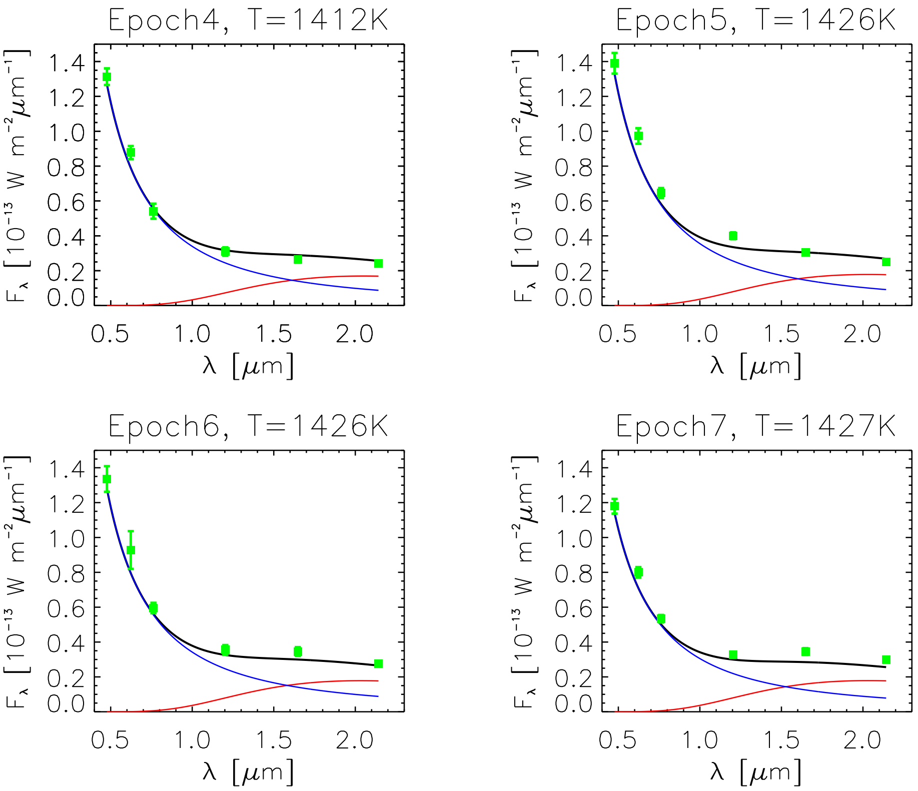

Figure 3.4 Observed fluxes and fit according to our model (compare Eq. 3.1) for epochs four to seven of NGC 3783 as an example for an AGN without reddening due to dust in the host galaxy. Due to the determined dust delay of NGC 3783 around 88 days these are the first epochs in which changes of the dust temperature can be determined. The green squares show the AGN fluxes, the blue line the AD model, the red line the single blackbody dust model, and the black line the combined fit. The temperature of each epoch is given at the top of the corresponding plot.

In many cases the variability factor v cannot be constrained, especially if the number of observations and/or the variability of the AGN is small. For most AGN with less than 15 observations v runs towards unphysical values ($v \leq 0$ or $v \gg 1$). In these cases we assume a value of $v = 1$. While it is unfortunate to be unable to constrain this parameter in most cases, its impact on the results of the other parameters is negligible.

The resulting corner plot for all of our model parameters from Eq. 3.1 can be seen in Fig. 3.5. Correlations between the parameters C_1 and α, and between C_2 and T_0 are seen. These parameters describe the AD radiation and the blackbody radiation of the dust, respectively. For example both T_0 and C_2 decrease or increase the blackbody radiation in our fit and thus a higher dust temperature has to be compensated by a lower value of C_2. There is no such correlation between other parameters. The corner plots for the other AGN in our sample show similar

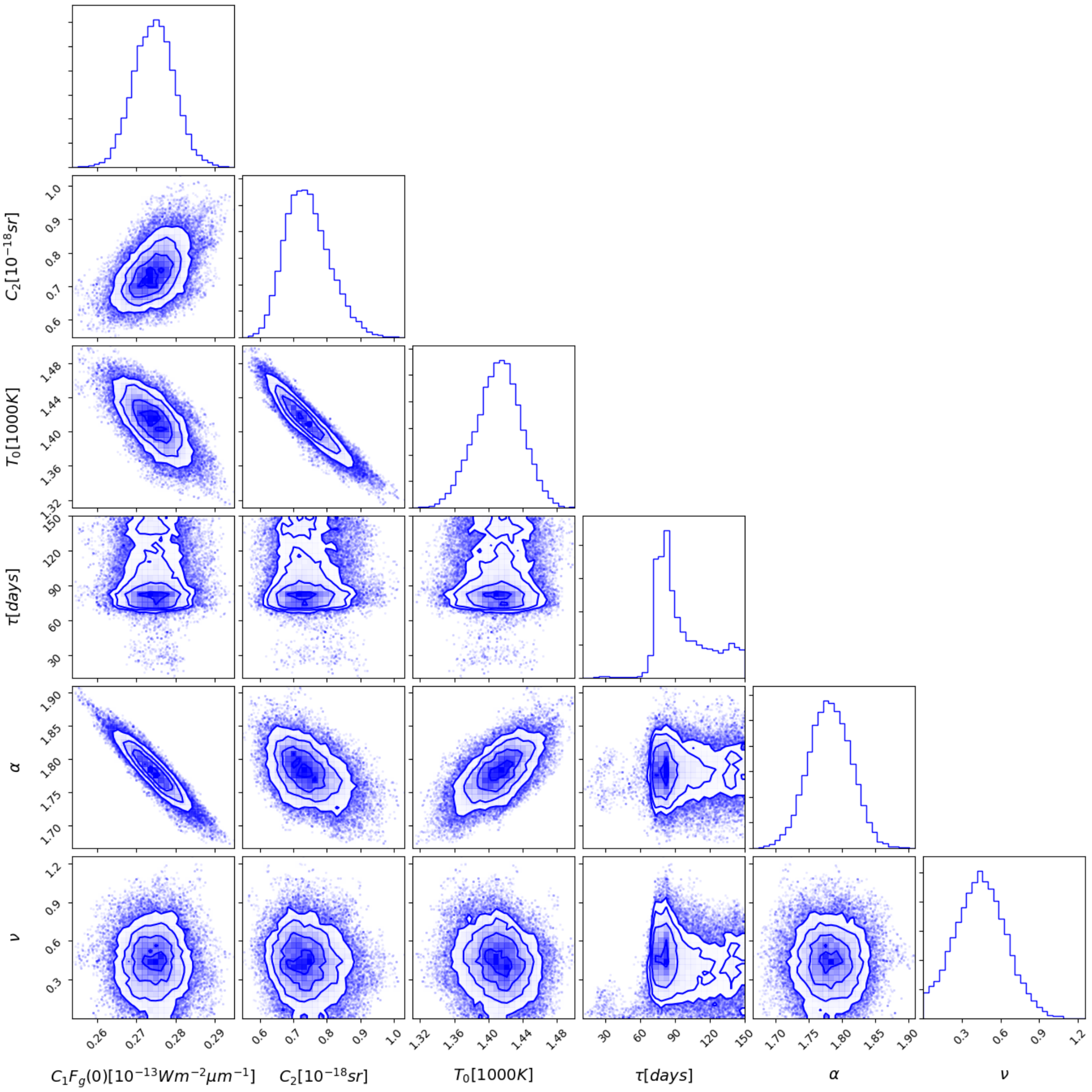

Figure 3.5 Corner plot for model parameters (given in Eq. 3.1) in the case of NGC3783 as an example of an AGN without reddening due to dust in the host galaxy.

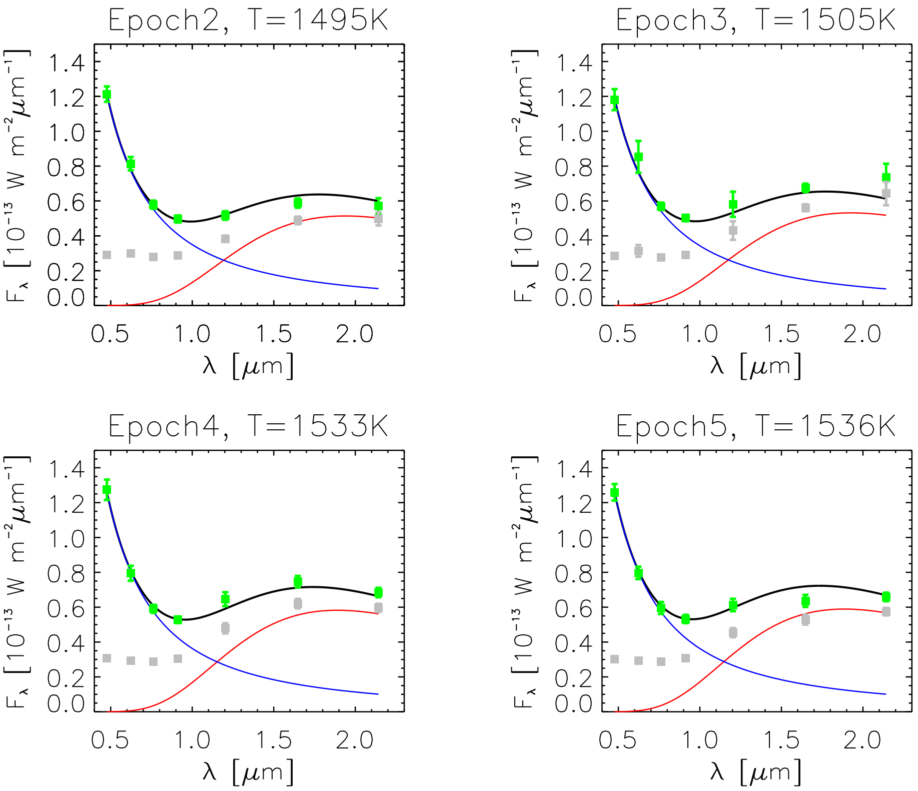

Figure 3.6 Observed fluxes and fit according to our model (compare Eq. 3.1) for the epochs two to five of Mrk 1239 as an example of an AGN with host extinction. The gray squares indicate data reddened by dust in the host galaxy, the green squares show the fluxes with the host extinction correction, the blue line shows the AD model, the red line the single blackbody dust model, and finally the black line the combined fit. The temperature of each epoch is given at the top of the corresponding plot.

correlations. The resulting parameters are presented in Table 3.5.1. In some cases only a lower limit could be determined for τ and this lower limit is added to the table as well.

AGN with host extinction

As mentioned above, we added a reddening correction, if the SED deviated clearly from a power law in the optical. As an example of this the the SEDs of epochs two to five of Mrk 1239 are shown in Fig. 3.6. Before applying the correction, the SEDs are almost flat in the optical (gray squares). The reddening, most likely caused by dust within the host galaxy, determined within our MCMC process in this particular case is $B-V = 0.43^{+0.13}_{-0.12}$. The corrected fluxes are shown with green squares and we now see a power law in the optical as expected from AD radiation.

However due to the wavelength dependence of the reddening correction almost

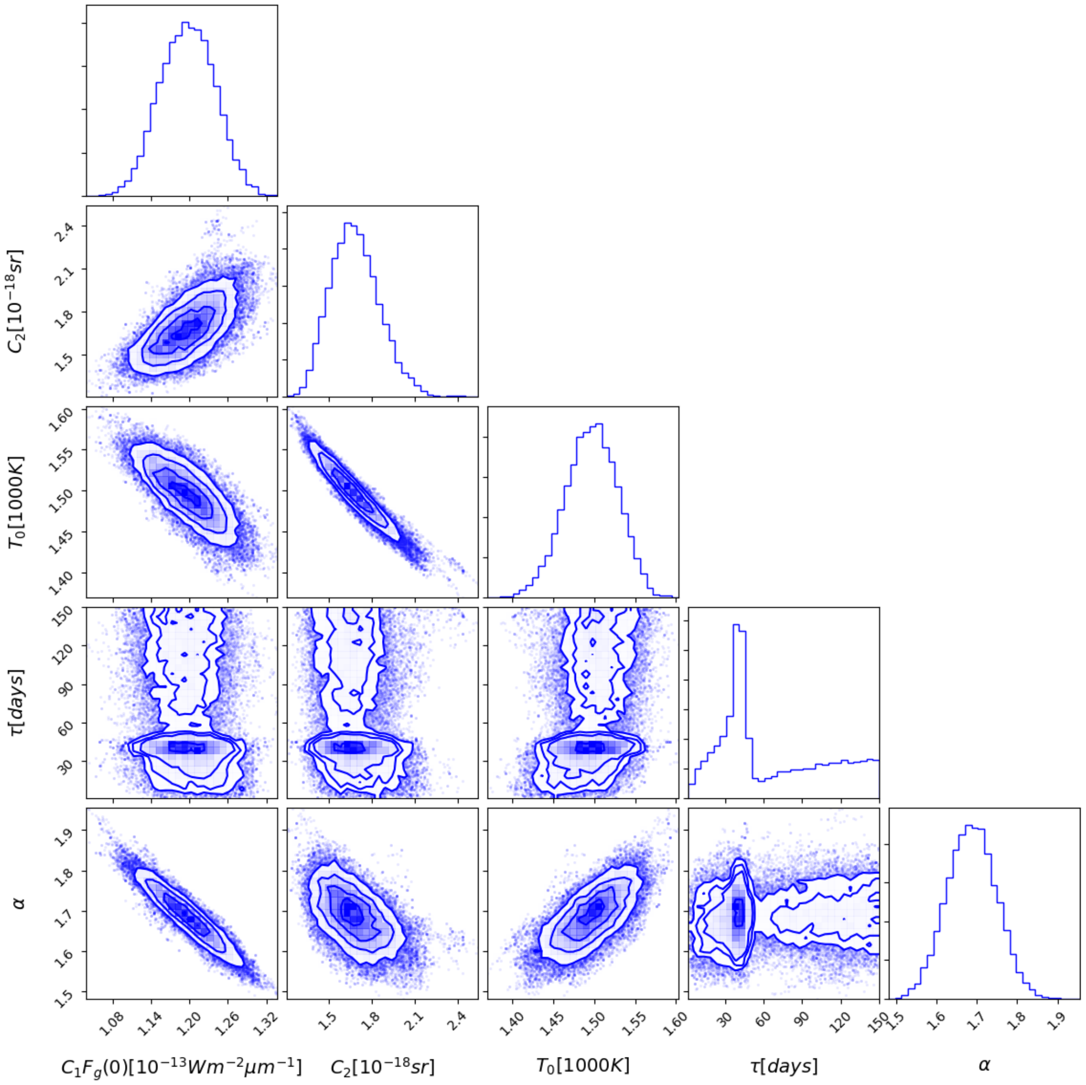

Figure 3.7 Corner plot for model parameters (given in Eq. 3.1) in the case of Mrk 1239 as an example of an AGN with reddening due to dust in the host galaxy.

all other parameters are strongly correlated with B-V, especially α and C_1 as the correction is strongest at optical wavelength. But a higher B-V leads to a higher dust temperature or higher C_2 as well. These correlations lead to extreme uncertainties for the other parameters. Therefore we perform a second MCMC with B-V fixed at its best fit value for every target. Thus the second run is comparable to the modelling the AGN without host extinction.

In Fig. 3.7 we present the corner plot of the second run for the example Mrk 1239. Again correlations can be seen for parameters describing the same AGN component. All of our model parameters are shown along with B-V in Table 3.5.1. Values determined for B-V range from 0.34 to 1.50. This means the optical V-band lumi-

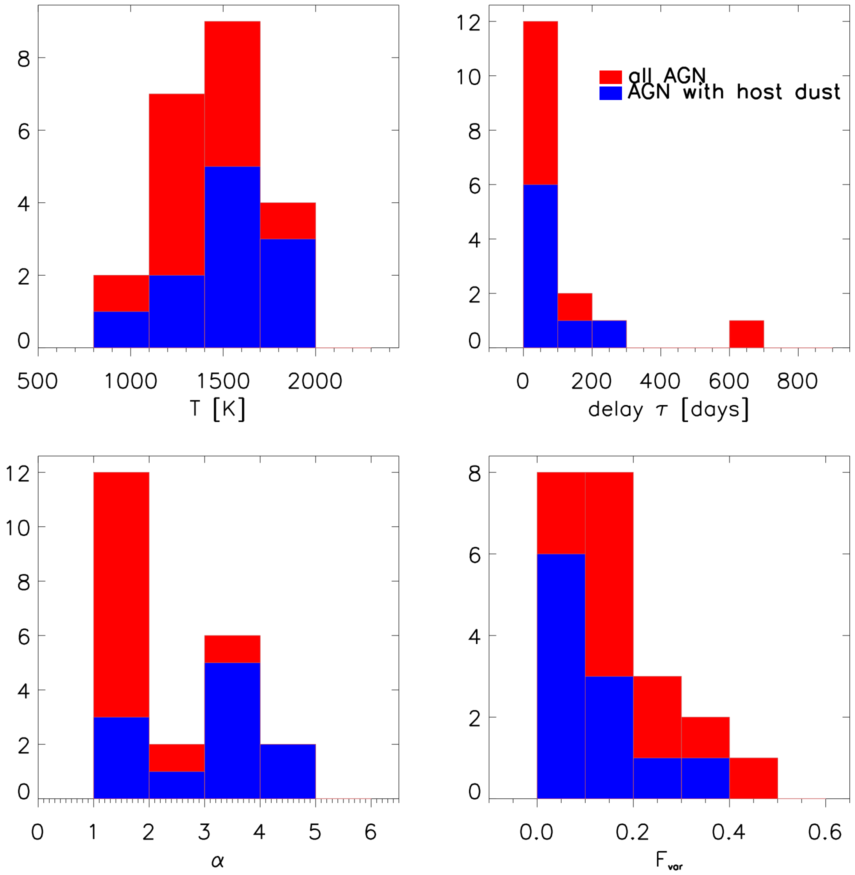

Figure 3.8 Histograms for the model parameters T (upper left panel), τ (upper right panel), α (lower left panel) and F_{var}. The histograms cover all AGN with a complete set of parameters or at least a lower limit for the delay, as can be seen in Table 3.5.1 (red) and for a the subsample of the AGN which show reddening by dust in the host galaxy. Also included, are the results for NGC 4151 from Schnülle et al. (2015). These are 19 and 10 AGN respectively.

nosity L_V (which we will use later) is increased by a factor between 2.5 and 58.

Comparison between AGN with and without host extinction

As mentioned above the B-V parameter in our model affects the other model parameters, mainly the AD parameters in the optical. Unfortunately the number of AGN is too small to derive general differences between these two groups, especially if only considering AGN with a full set of parameters or at least with only the delay missing (11 with host extinction and 11 without, if adding the values for NGC 4151 from Schnülle et al. 2015). However in the histograms in Fig. 3.8 we can see some trends. In all plots the group of AGN with extinction by dust in the host galaxy is shown in blue, while all AGN are shown in red.

The distribution of dust temperatures (upper left panel in Fig 3.8) does not show a significant difference between the two groups. The temperatures of AGN with host extinction tend to be slightly higher. This could be caused by the higher reddening correction at shorter wavelength, however the difference seen in the histogram can be expected for such low numbers. We can see an overall distribution of temperatures around $\sim$ 1500 K and a cutoff for the highest dust temperatures 1900 K. This limitation is in good agreement with the highest sublimation temperatures found for graphite grains around 1900 K (e.g. Salpeter 1977; Guhathakurta & Draine 1989; Laor & Draine 1993) and the findings of Landt et al. (2019) of a graphite dominated dust composition. Dust temperatures below $\sim$ 1000 K, which would we be needed for dust formation at the inner edge of the dust torus, are only rarely found.

There are no major differences between the two groups for the dust delays τ (upper right panel) as well. Looking at the optical variability F_{var} (lower right panel) we see more lower values for AGN with host extinction. However the reddening correction has no effect on the parameter F_{var}. The definition of F_{var} in Eq. 3.6 tells us this might be caused by a higher relative measurement uncertainty $\delta_{g'}$ caused by lower fluxes due to the dust extinction.

The main difference between the two groups is the power law index α of the AD radiation. The AGN with host extinction completely dominate the higher values of α (lower left plot). As α is the parameter most affected by the reddening correction it is most likely to see differences in α. If we look at our example galaxy of this class Mrk 1239 a change of B-V around the errors given for B-V leads to a change of α of 0.5.

Additionally, for the AGN not fitting our model, where dust parameters could not be derived, we determine values of α as high as 4.0 for CTSJ 13.12, showing no signs of dust extinction. This would already reduce the differences between these two groups seen in the histogram because of low number statistics.

However a major aspect, which has to be taken into account here, is that we made the reddening correction only for AGN which showed very clear signs of extinction in their SED (as can be seen in the SED of Mrk 1239 in Fig. 3.6). Hence the smallest value of B-V we find is 0.34 for NGC 3227 leaving a lot of room for smaller values of B-V. There is also the possibility of an overestimation of the reddening correction causing an overestimation of the power law index. In some cases, this could lead to an underestimation of the optical luminosity for the AGN without host extinction and an overestimation of the optical luminosity for AGN with host extinction.

There are no clear indications of a correlation between the amount of AGN showing signs of host reddening and their classification shown in Table 3.2 (from Véron-Cetty & Véron 2010). While the S1.0 type AGN ESO 377-G24, Mrk 590 and NGC 4593 show signs of host reddening (out of seven total AGN of this subclass in our sample), ESO 362-G18, H 1934-063, NGC 3783 and NGC 5548 are classified as S1.5 and show no signs of host reddening (out of eight AGN in this class). Therefore a connection to the viewing angle cannot be verified. Possibly the reddening could be caused by polar dust found in some AGN (e.g. Hönig et al. 2012, 2013; Tristram et al. 2014; López-Gonzaga et al. 2014).

Overall there seem to be no intrinsic differences between AGN with and without host extinction. It is possible that the reddening correction is overestimated for some of our sources. This leads to an overestimation of α and also the optical luminosity. As the underestimation of the optical luminosity without the correction would be more severe and it is not easy to determine a reasonable fixed value of α for these AGN, we will use the fit parameters determined.

3.5.2 Individual sources

For some of our AGN there are problems within the MCMC leading to difficulties for the reverberation mapping. Some of the problems occur regularly others are specific to individual AGN. Generally a low variability of the AD signal is the biggest problem. We follow the definition of the variability of the AD signal from Suganuma et al. (2006):

$$F_{\text{var}} = \frac{\sqrt{\sigma_{g'}^2 - \delta_{g'}^2}}{\langle g' \rangle}, \tag{3.6}$$

where $\sigma_{g'}$ and $\delta_{g'}$ are the standard deviation and the measurement uncertainty of the g' band signal. Especially if the uncertainty is larger than the standard deviation, which is indicated by $\sigma_{g'} < \delta_{g'}$ in the F_{var} column of Table 3.5.1, it is impossible to determine a dust delay.

In the following paragraphs we will shortly discuss some of our AGN:

AGN with complete set of parameters

3C273 3C273 is the AGN with, by far, the highest absolute luminosity and redshift of our AGN sample. Due to the large distance we are not able to resolve galactic components of 3C273 and therefore our fluxes are contaminated by the host galaxy. This contamination is most pronounced in the i' and z' filter which are therefore not considered in our analysis. If the i' and z' filter are not left out, the MCMC gives us a temperature well above 2000 K, higher than the highest sublimation temperatures of dust around 1900 K for graphite (e.g. Salpeter 1977; Guhathakurta & Draine 1989; Laor & Draine 1993), and a dust delay around 250 days far too small for an AGN of this brightness.

NGC 5548 In the case of NGC 5548 the V band lightcurve from the AGN STORM project (Edelson et al. 2015; Fausnaugh et al. 2016), which was observed simultaneous with our observations, was used for the AD signal. The V band was chosen because it has both the biggest overlap with our observations and the cadence is highest for all AGN STORM bands. A couple of years after our observations the dust delay and dust temperature of NGC 5548 was also determined by Landt et al. (2019) in the first spectroscopic dust reverberation mapping program. Their delay is slightly lower than ours (70 and 79 days respectively) while their mean temperature is slightly above ours (1450 K compared to 1400 K).

AGN without good delay determination

H 0557-385 The combination of the lowest dust temperature in our sample and a relatively high absolute luminosity lead to a very high expected dust delay for H 0557-385. In fact this delay is higher than the observational baseline available to us. Additionally the χ^2 for a delay τ larger than the observational baseline (thus we fit a constant temperature) is almost the same as the smallest χ^2 we get for smaller delays (for a delay of $\sim$ 400 days). Therefore the measured delay is likely not reliable and might be significantly higher.

H 2107-097 H 2107-097 is similar to the case of H 0557-385. A low dust temperature combined with a high absolute luminosity leads to an expected dust delay higher than the observational baseline. In this case a solution with delays larger than the observational baseline, and therefore with a constant temperature, lead to a similar χ^2 as the lowest χ^2 of smaller delays (for a delay of $\sim$ 180 days). However, since the AD variability F_{var} is very high, a constant temperature should not work as well. Therefore a lower limit of 400 days is assumed as the best result in this case.

NGC 4593 NGC 4593 is one of the AGN with the lowest absolute luminosity in our sample. Due to this we expect a very low delay (between 10 and 20 days). As

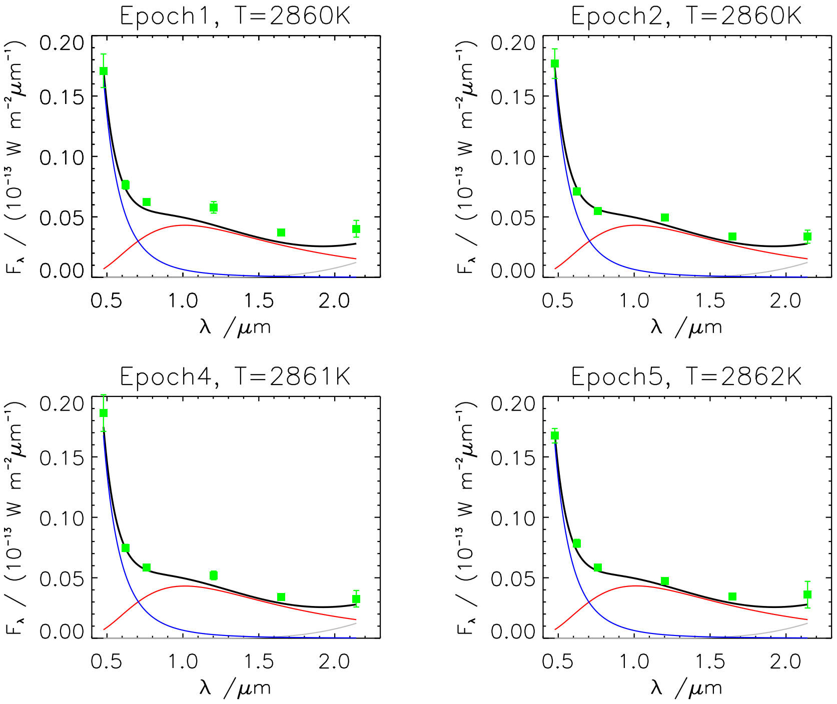

Figure 3.9 Observed fluxes and fit according to our model (compare Eq. 3.1) and an additional blackbody due to the increased flux in the K band. The third epoch is not shown as the flux in the H and K band is not available in this case. The green squares show the fluxes with the host extinction correction, the blue line the AD model, the red line the blackbody of the dust model with the higher temperature (2857^{+65}_{-68} K), the gray line the blackbody of the dust model with the lower temperature (576^{+54}_{-23} K), and the black line the combined fit. The hotter temperature for each epoch is given at the top of the corresponding plot.

we have only six observations spread over almost two years it was not possible to determine a delay despite the high F_{var}.

AGN not fitting our model

CTSJ 13.12 For CTSJ 13.12 we find the highest temperature of our sources (2702^{+63}_{-64} K). Additionally an access of NIR flux especially in the K band can be seen indicating a colder blackbody component. The most likely explanation for the very hot blackbody is a remnant of host dust flux. We therefore adjusted our model and included a second blackbody component (compare Fig. 3.9). The resulting second temperature of 576 K is probably too cold for the innermost dust of an AGN. Additionally the AD variability is too small to measure a reliable dust delay for this source especially for the colder blackbody component. As CTSJ 13.12 is not well fit by our model it was not included in the further analysis.

ESO 377-G24 In the case of ESO 377-G24 a simple power law fits the data very well and no dust component is needed. The most likely reason is an absence of dust with temperatures above roughly 500 K. Dust with temperatures below 500 K can only be observed at wavelength shorter than the K band at low redshift. This is in agreement with the SEDs found for the population of hot dust poor AGN (Hao et al. 2010, 2011; Jun & Im 2013; Lyu et al. 2017).

HE 1228+013 HE 1228+013 shows clear signs of reddening by host dust. Unfortunately the dereddening correction does not work in this case. The most likely reason for this is the large distance compared to the rest of our sample (only 3C273 has a higher redshift). Because of this we are not able to resolve all galactic components with GROND and are thus unable to subtract them. Within our MCMC analysis the reddening parameter B-V is most likely overestimated. Therefore HE 1228+013 has to be left out of the further analysis.

IC 355 For IC 355 a high dust temperature well above 2000 K was found. Within the MCMC the algorithm prefers very low values of ν close to zero. This indicates that the dust is not responding to the AD at all.

NGC 1019 The SED of NGC 1019 shows a completely irregular behaviour. At both optical and NIR wavelength it shows a very high variability in intensity and in shape. Especially the slope in the optical changes from very flat (as seen for the AGN with host extinction) to the power law behaviour expected for AD radiation more than once within the 17 month it was observed. This cannot be explained by contamination by host galaxy flux because this is not expected to vary so strong at such short time scales. NGC 1019 cannot be fitted by our model.

3.5.3 Comparison to results from interferometry

Dust radii in AGN can be measured more directly using interferometry (compare Section 2.2). The GRAVITY Collaboration et al. (2019) used the VLTI/GRAVITY instrument to measure the dust radii of eight AGN, where two of them (3C273 and NGC 3783) are also in our sample and we can compare our delays to their radii, all shown in Table 3.3. For this we correct our delays for time dilation.

For both 3C273 and NGC 3783 our measured delay is slightly smaller than the interferometric measurement. This deviation from reverberation mapping are reported for most of the AGN by GRAVITY Collaboration et al. (2019). It is explained by reverberation mapping results giving the response-time weighted (innermost)

Table 3.3 Comparison of our dust delays for 3C273 and NGC 3783, corrected for time dilation, to the results from GRAVITY Collaboration et al. (2019) using interferometry in the *K* band. For comparison, we also determined the dust delay only using the *K* band in the NIR. All values are given in units of days and lightdays respectively.

	3C273	NGC 3783
Delay this work	606^{+95}_{-90}	87^{+38}_{-12}
Delay this work only K in NIR	-	83^{+15}_{-4}
Radius Gravity 2019	675 ± 126	131 ± 20

radius while interferometry gives a radius weighted dust radius slightly further out, where the radiation from the dust is highest.

As the *K* band was used by GRAVITY Collaboration et al. (2019) we re-analysed our reverberation data using only the *K* band in the NIR (also shown in Table 3.3). This was done to avoid differences as hotter dust might be traced in the *J* and *H* band. For NGC 3783 this did not change the measured delay significantly. In the case of 3C273 we are left with only a few epochs in which the delay can be probed due to the high delay of 3C273. When leaving out the *J* and *H* band we do not get a reliable delay with only the *K* band.

3.6 Discussion

3.6.1 Radius luminosity relation

One of the central outcomes of a reverberation mapping campaign is the plot relating the delay of the dust flux to the AD absolute luminosity. In our case we use the optical flux as a proxy of the AD flux. For better comparison of our results to results in the literature we convert our mean g' band fluxes to flux in the V band, which is used more often in reverberation mapping. To make this conversion we use the power law index α derived in our model:

$$S_V = S_{g'} \left(\frac{\lambda_{g'}}{\lambda_V} \right)^{\alpha} . \tag{3.7}$$

Following this we need to convert our fluxes to absolute luminosity. For this we apply the conversion to L_V from Hogg (1999) given in their Eq. 23:

$$L_V = S_V \cdot 4\pi D_L^2 \cdot (1+z) \cdot \lambda_V . \tag{3.8}$$

Our delays have to be corrected for time dilation with $\tau = \tau/(1+z)$. The resulting plot of τ against L_V is shown in the upper panel of Fig. 3.10. The delays of the AGN with host extinction are indicated by open circles and the results from Schnülle et al. (2015) for NGC 4151 are shown as triangles. The three cases, where only a lower boundary for the delay could be found (H 0557-385, H 2107-097, and IC 355), are indicated by arrows instead of error bars and are not taken into account for the following fits.

Figure 3.10 *(following page)* Dust delay τ plotted against the optical luminosity in the V filter L_V with the dust temperatures indicated by the colors. Filled (open) circles represent AGN without (with) host extinction. Triangles indicate the results for NGC 4151 from Schnülle et al. (2015), which were determined using the same methodology (however without g', r' and i' fluxes available). While in the upper plot we show the delays from Table 3.5.1, in the lower plot the delays were normalized by the dust temperatures also given in Table 3.5.1 to a temperature of 1500 K. The solid red line in both plots indicates a power law fit with a fixed slope of 0.5 with the best fit results $\tau = (4.1 \pm 1.1) \cdot 10^{-17} \mathrm{daysW}^{-0.5} \cdot \mathrm{L}_{\mathrm{V}}^{0.5}$ and $\tau_{\mathrm{norm}} = (4.6 \pm 1.1) \cdot 10^{-17} \mathrm{daysW}^{-0.5} \cdot \mathrm{L}_{\mathrm{V}}^{0.5}$. If the slope is freed the best fit results are $\tau = (28 \pm 3) \cdot 10^{-17} \mathrm{daysW}^{-0.5} \cdot \mathrm{L}_{\mathrm{V}}^{0.37 \pm 0.02}$ and $\tau_{\mathrm{norm}} = (3.9 \pm 0.9) \cdot 10^{-17} \mathrm{daysW}^{-0.5} \cdot \mathrm{L}_{\mathrm{V}}^{0.51 \pm 0.02}$. The gray areas in each plot indicate the scatter of the fits with freed slope. Given in the upper part of each plot is the χ^2 value for each fit with a fixed slope which is significantly smaller in the normalized case.

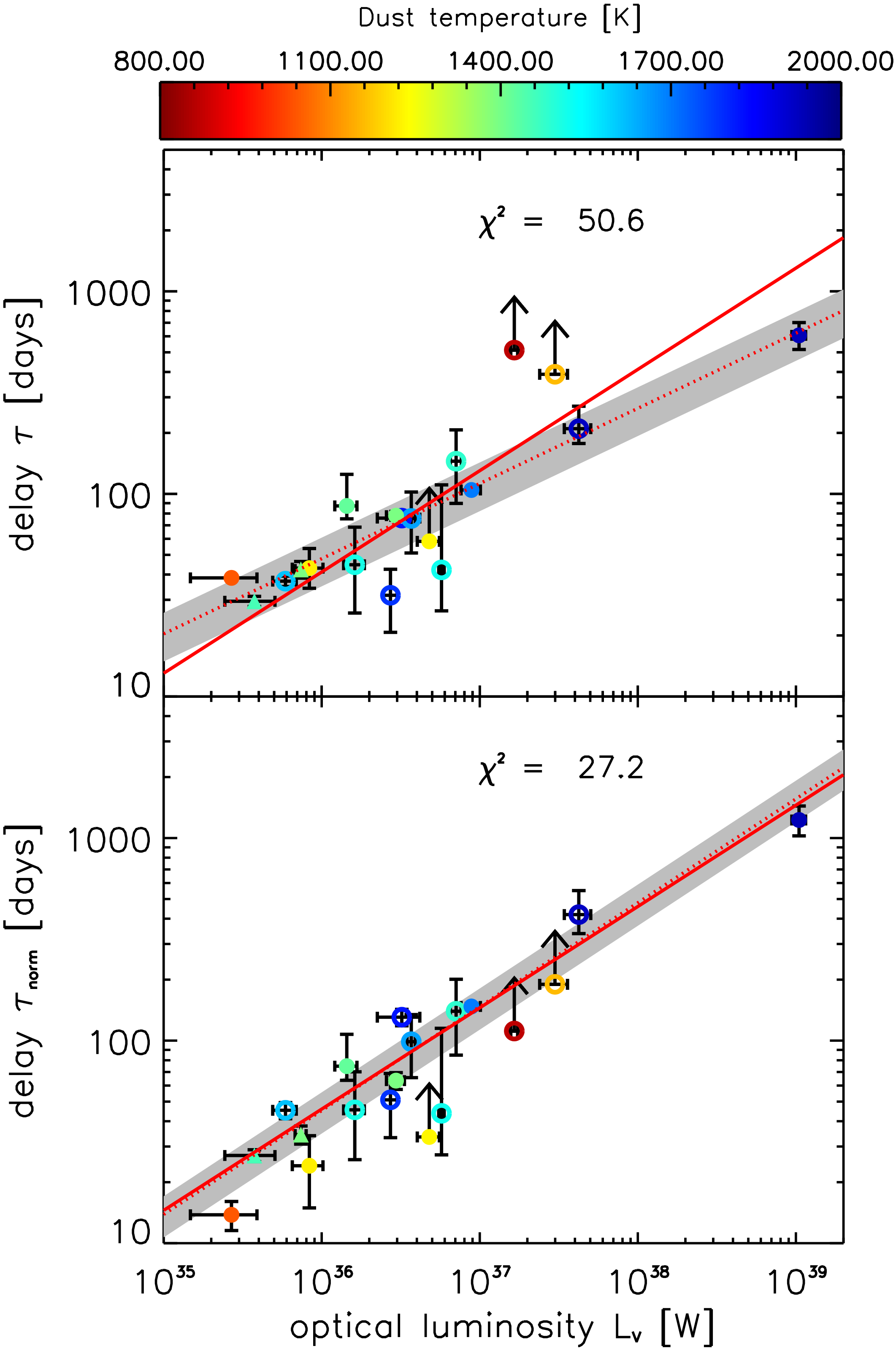
Dust temperature [K]
800.00
1100.00
1400.00
1700.00
2000.00
χ^2 = 50.6
delay τ [days]
10
100
1000
χ^2 = 27.2
delay τ_{norm} [days]
10
100
1000
10^{35}
10^{36}
10^{37}
10^{38}
10^{39}
optical luminosity L_V [W]

We fit two power laws to the data in this plot, using the Interactive Data Language (IDL) routine MPFITEXY (Williams et al. 2010) depending on the MPFIT package (Markwardt 2009), which is also used for all following fits. First we keep the slope fixed at the expected value of 0.5 for the radius luminosity relation (solid red line in Fig. 3.10). The resulting fit is:

$$\tau = (4.1 \pm 1.1) \cdot 10^{-17} \mathrm{days W^{-0.5}} \cdot \mathrm{L_V^{0.5}}. \tag{3.9}$$

Compared to the results published in Suganuma et al. (2006) the mean values agree very well and the scatter in this relation is also very similar (≈ 30 % for Suganuma et al. 2006 and ≈ 27 % in our case). Koshida et al. (2014) find similar results with a comparable scatter as well.

If we select only the AGN with extinction by dust in the host galaxy (compare Section 3.5.1) for this fit (open circles in Fig. 3.10) the best fit intercept is $(4.3 \pm 0.9) \cdot 10^{-17} \mathrm{days W^{-0.5}}$ slightly above our fit to the complete data set. This shows that an over estimation of L_V due to the reddening correction is unlikely.

If we release the slope (dotted red line) we get a significantly smaller value for the slope with

$$\tau = (28 \pm 3) \cdot 10^{-17} \mathrm{days W^{-0.5}} \cdot \mathrm{L_V^{0.37 \pm 0.02}}. \tag{3.10}$$

The main reason for this shallower slope is the delay found for 3C273 which is located far below the fit with a fixed slope at high luminosity. This behaviour is also seen in other studies, to which quasars are added. Minezaki et al. (2019) and GRAVITY Collaboration et al. (2019) find slopes of 0.42 ± 0.03 and 0.40 ± 0.04 respectively in good agreement with our results.

Due to their high delays quasars are usually avoided in reverberation mapping campaigns as very long baselines of observations are needed to determine their delays. Therefore the number of quasars in reverberation mapping campaigns are small. Still the question arises whether high dust temperatures (hence smaller radii) are a common property of quasars leading to the flattened slopes. However single epoch fitting of spectra found dust temperatures of ∼ 1450 K for 3C273 in 2006 (Landt et al. 2011b, 2014).

Another observational bias can occur for low luminosity AGN: A higher cadence of observations is needed to determine dust lags for these sources which are often not achieved in reverberation mapping campaigns. Time lags in the range of only a few light days or less can often not be determined. In our case we were not able to determine the time lag of NGC 4593 with a very short expected delay (compare Table 3.4). On the other hand we were able to determine the lag for ESO 362-G18 likely because the mean temperature is very low in this case with around 1000 K. This increases the expected lag significantly by approximately a factor of three.

This leads to a lack of high luminosity AGN with relatively cold dust and of low luminosity AGN with high dust temperatures. It could be interesting to see whether this is purely an observational bias or an intrinsic difference of AGN with different AD luminosity.

Temperature normalized radius luminosity relation

The distance between heating source and dust relates to the dust temperature as $\tau \propto T^{-2.8}$ and the grain size of the dust as $\tau \propto a^{-0.5}$ (Barvainis 1987; Kishimoto et al. 2007). While a measure of the grain size is not available to us we measure the dust temperature within our model directly. Fortunately the dependence on the temperature is stronger compared to the dependence on the grain size and we can normalize for the proportionality in T with:

$$\tau_{\mathrm{norm}} = \tau \cdot \left(\frac{T}{1500\mathrm{K}}\right)^{2.8}. \tag{3.11}$$

We choose 1500 K as the normalization temperature, as it is a typical temperature of AGN in our sample. After this normalization of the delay we plot the radius luminosity relation again in the lower panel of Fig 3.10 in the same way as in the upper panel. The fit with a slope fixed at 0.5 (solid red line) results in the best fit power law

$$\tau_{\mathrm{norm}} = (4.6 \pm 1.1) \cdot 10^{-17} \mathrm{days W}^{-0.5} \cdot \mathrm{L}_{\mathrm{V}}^{0.5}. \tag{3.12}$$

Changes in the intercept of the fits with τ and τ_{norm} are caused by the choice of the normalization temperature in Eq. 3.11. As we choose a temperature close to the mean value for our AGN the change in the intercept is small. The scatter for τ_{norm} is $\approx$ 23 % and thus smaller than for τ. This improvement is also expressed in the improvement of χ^2 (given for the two fits with fixed slope in Fig. 3.10) by a factor of $\sim$ 2. In the cases of H 0557-385 and H 2107-097 the lower limits of the delay were located well above the radius luminosity relation but due to their low dust temperatures they are moved below the relation after our normalization.

A power law with freed slope (dotted red line) yields a best fit power law

$$\tau_{\mathrm{norm}} = (3.9 \pm 0.9) \cdot 10^{-17} \mathrm{days W}^{-0.5} \cdot \mathrm{L}_{\mathrm{V}}^{0.51 \pm 0.02}. \tag{3.13}$$

After the temperature correction the fit is almost identical to the power law and the slope is in almost perfect agreement with the expected $\tau \propto L^{0.5}$ relation. From

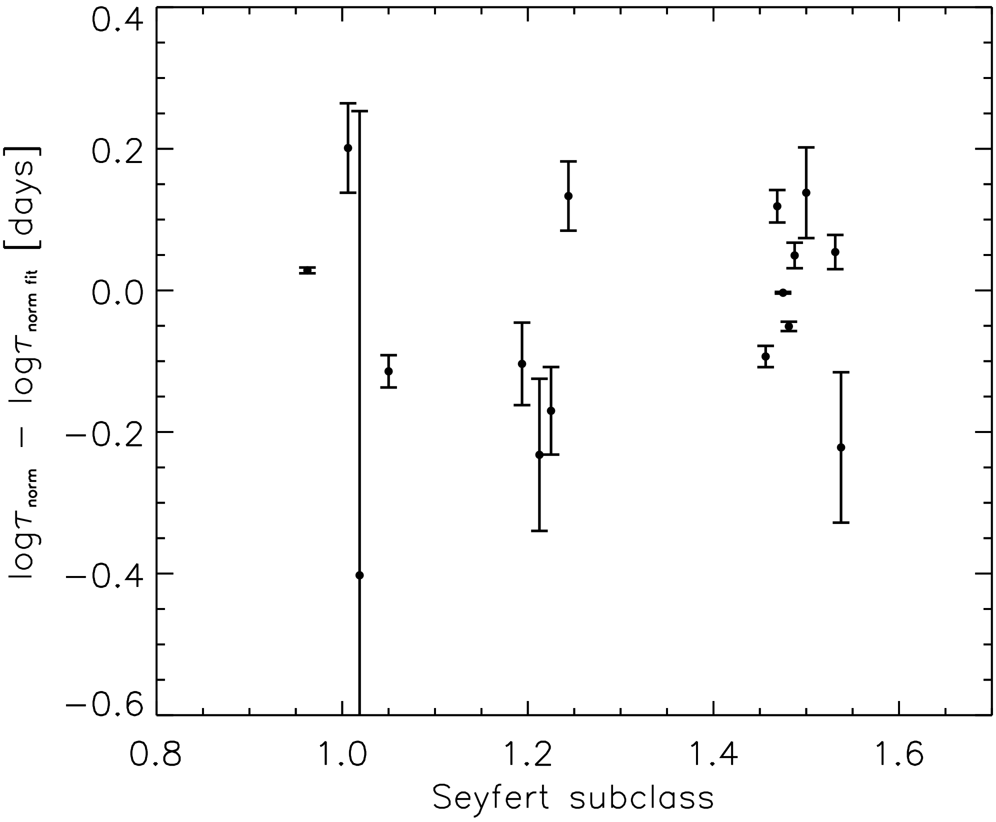

Figure 3.11 Residual between τ_{norm} and the best fit power law from the lower part of Fig. 3.10 against the subclass of the Seyfert type (compare Table 3.2).

eye inspection of Fig. 3.10 the change of the slope is mainly caused by the high dust temperature observed in 3C273 around 1900 K. As mentioned in Section 3.5.2 the fluxes of 3C273 are possibly contaminated by host dust flux. This could lead to an overestimation of the temperature. However even if we reduce the dust temperature of 3C273 to 1700 K (more than 4σ below the estimated temperature) the slope has a best fit value of 0.48 ± 0.02. Not considering 3C273 at all leads to a slope of 0.58 ± 0.04. So the change of slope is not as dependent on 3C273 as it may appear.

Using long-baseline interferometry like VLTI/Gravity it might be possible to fill at least the high luminosity end of the radius luminosity relation and reduce the observational bias there.

Further sources of scatter in the radius luminosity relation

A part of the scatter, remaining in the radius luminosity relation after temperature normalization, could be produced by intrinsic differences of the AGN. One of the differences is the viewing angle. Kawaguchi & Mori (2011) predict an increasing lag with increasing viewing angle. This is caused by self-occultation effects of nearby clouds. These nearby clouds have the smallest apparent lag and, as soon as they are hidden behind other dust clouds, no longer contribute to our measured lag.

In Fig. 3.11 we show the residual between our normalized delay τ_{norm} and its best fit power law against the Seyfert type. The Seyfert types (S1.0, S1.2, and S1.5) of our AGN were taken from Véron-Cetty & Véron (2010) and are given in Table 3.2. For better visibility we shifted the points slightly from their exact subclass. There is no obvious dependence between the residuals and the Seyfert type (as a representation of the viewing angle). We are probably not sensitive enough to see this correlation but there is also the possibility that Seyfert subclasses and viewing angle are not clearly correlated.

It has also been shown that the Eddington ratio of the accretion rate has an effect on the dust lag (e.g. Du et al. 2015, 2016). But this is only significant for AGN with accretion rates around the Eddington rate when we move from thin to thick ADs. In this case, self-occultation of the AD would decrease the illumination of the dust and thus decrease the expected delay (Kawaguchi & Mori 2011; Kawakatu & Ohsuga 2011). The effects of these parameters on the dust lag are discussed in more detail in Section 5 of Koshida et al. (2014). As no AGN with such high accretion rates are present in our sample this effect is not important here.

Additionally if the ratios of the height above the AD to the radius of the dust clouds are different, a scatter could be introduced in the temperature normalization of the radius luminosity relation. Due to the anisotropic radiation field of the AD, AGN with a higher opening angle of the dust torus will have higher dust temperatures compared to AGN with clouds located at lower elevations above the AD. Unfortunately we are not able to test this source of scatter with our data set.

3.6.2 Radiating dust surface area

For some of our AGN we were unable to determine dust radii for reasons mentioned in Section 3.5.2 or we could only infer lower limits. We can use the temperature normalized radius luminosity relation in Eq. 3.12 and the temperature normalization in Eq. 3.11 to estimate dust radii for those AGN as well. These results are included in the following analysis of the surface area of the dust. The resulting dust radii are given in Table 3.4.

Despite the dust temperature we also get an estimate of the solid angle of the dust with our multiwavelength approach to reverberation mapping. In our model

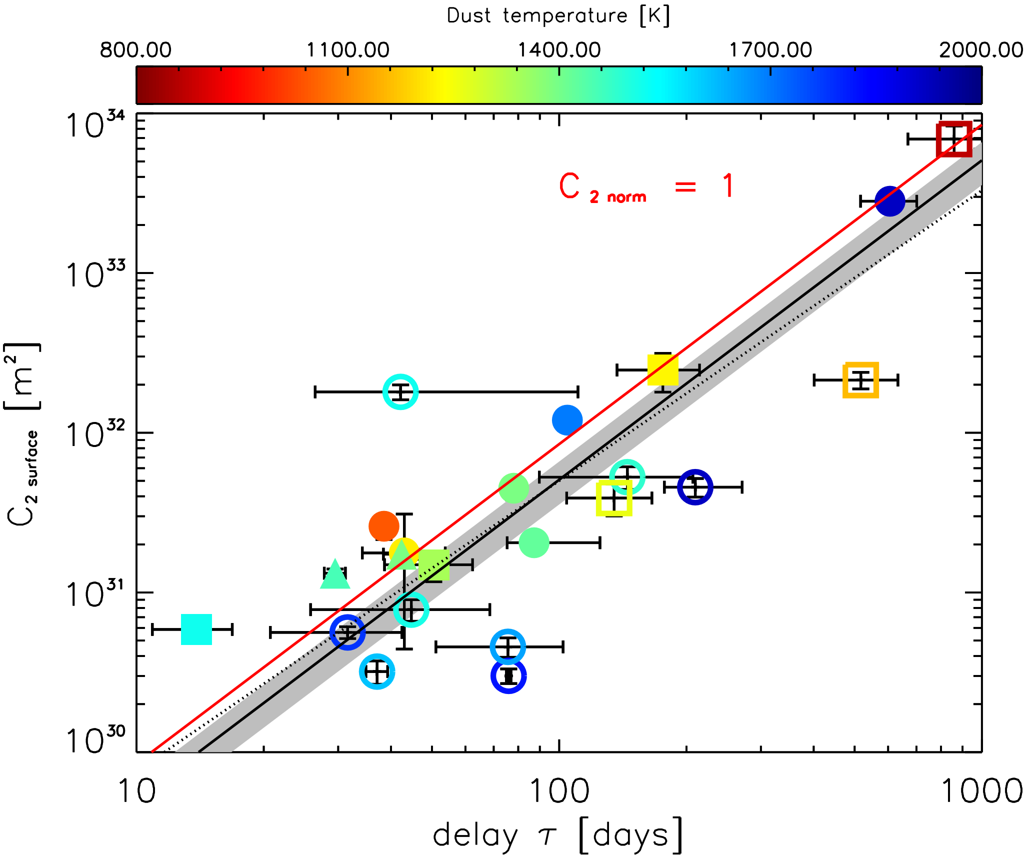

Figure 3.12 Surface area of the dust $C_{2\ \text{surface}}$ plotted against the dust delay τ with the color coding indicating the dust temperatures T. Filled (open) circles represent AGN without (with) host extinction. The squares represent AGN with τ determined using the dust temperature and L_V (compare Table 3.4). Marked with triangles are the results from Schnülle et al. (2015) for NGC 4151. A power law fit of the data is shown by the dotted line and has the form: $C_{2\ \text{surface}} = (1.7 \cdot 10^{28} \pm 1.9 \cdot 10^{28})\text{m}^2 \cdot \tau^{1.71 \pm 0.24}$. A fit with a slope fixed at 2 was added (solid black line). The gray area indicates the scatter of τ found for the fit with freed slope in the upper panel of Fig. 3.10. The red solid line indicates the typical value of $C_{2\ \text{surface}}$ used for the normalization in Eq. 3.17.

Table 3.4 Expected dust delays of the AGN without estimates of delays or only lower limits determined with reverberation mapping but with the dust temperature determined (compare Table 3.5.1). The delays were estimated using the fit to τ_{norm} with a slope fixed at 0.5 (Eq. 3.12) and the temperature normalization (Eq. 3.11). Additionally they were corrected for time dilation. For the uncertainties of the delay the 23 % scatter of that fit was used.

	$\log L_V$	T	τ
	W	K	days
ESO 383-G035	36.52	1264	136 ± 31
H 0557-385	37.22	871	889 ± 198
H 1934-063	35.81	1336	51 ± 12
H 2107-097	37.48	1164	531 ± 119
Mrk 704	36.68	1226	181 ± 40
NGC 4593	35.00	1517	14 ± 3

from Eq. 3.1 this estimate is represented by the parameter C_2. Using the luminosity distance D_L of the AGN we can estimate the surface area of the dust $C_{2\text{ surface}}$:

$$C_{2\text{ surface}} = C_2 \cdot 4\pi D_L^2. \tag{3.14}$$

We plot the surface area of dust against the dust delay in Fig. 3.12 with the dust temperature color coded, including all objects shown in Fig. 3.10 and the objects from Table 3.4. As expected an approximately quadratic trend of larger dust surface with higher delay is clearly visible, although with a large scatter. If we fit a power law, we get a best fit solution of:

$$C_{2\text{ surface}} = (2.1 \pm 2.0) \cdot 10^{28}\text{m}^2 \cdot \tau^{1.70 \pm 0.21}. \tag{3.15}$$

The surface area of the dust for Mrk 590 is extremely small for its dust delay of 78 days (dark blue open circle at the bottom of Fig 3.12), especially considering the small uncertainty of the delay. In fact it is located more than 50 σ from the fit in Fig. 3.12. Likely it is another case of a dust poor AGN and the dust is only observable due to the high temperature. As the uncertainty of the delay is very small for Mrk 590 it has a huge influence on this and the following fits and is therefore not included. Interestingly Mrk 590 is also classified as a "changing-look" AGN[1] in a phase of low BLR emission during our observations (Denney et al. 2014).

---

[1] A "changing-look" AGN shows significant changes of BLR emission and thus AGN subclass. Obscuration of the BLR can be excluded as the reason behind these changes (Hutsemékers et al. 2019).

From geometric consideration the surface area should be proportional to the circumference of the dusty region times (approximately) the radial extend of the dust torus ($\tau_{out} - \tau_{in}$) for a constant cloud filling factor. The circumference of a toroidal dust distribution with radius τ is proportional to τ, while we expect also the radial extent to scale with τ, so the radiating surface area should scale with τ^2. The fit in Eq. 3.15 shows in fact a similar dependency within the uncertainties. Fixing the slope of the relation at 2 (solid line in Fig.3.12) we arrive at

$$C_{2\text{ surface}} = (5.5 \pm 5.5) \cdot 10^{27}\text{m}^2 \cdot \tau^2. \tag{3.16}$$

Comparing the two fits in Fig. 3.12 with the fixed slope we are able to fit the AGN with high dust radii significantly better. Using the radius luminosity relation from above we arrive at $\tau_{out} - \tau_{in} \propto \tau^1 \propto L^{0.5}$. This means the radial extend of the dust torus has a similar dependence on the AD luminosity as the radius itself.

To further investigate the situation, we compare the radiating dust surface area with the dust temperatures. At high temperatures (near the sublimation temperature) systematically smaller surface areas could be expected as small luminosity changes can lead to sublimation of dust and thus changes of the surface area. For this comparison, we define a dust surface area $C_{2\text{ norm}}$, normalized to the typical sample value of $4\pi\tau^2$:

$$C_{2\text{ norm}} = \frac{C_{2\text{ surface}}}{4\pi\tau^2}. \tag{3.17}$$

The resulting $C_{2\text{ norm}}$ for all of our AGN are shown in Table 3.5 and Fig. 3.13. Fitting a power law again we get:

$$C_{2\text{ norm}} \propto T^{-0.9\pm1.3}. \tag{3.18}$$

This dependence between surface area of dust and dust temperature is weak. No dependence is consistent with the error of the correlation slope.

The large scatter in the dust surface correlations with radius and temperature is likely caused by intrinsic differences between the AGN. It seems in excess of the intrinsic scatter of the radius luminosity relation, which is indicated by the gray area in Fig. 3.12. The latter describes the typical location of the hot dust clouds, while the former is a proxy for the amount of radiating hot dust. Thus, the increased scatter of $C_{2\text{ surface}}$ hints to a source dependent amount of dust, likely linked to the dust formation and illumination history of the object.

Very interesting in this context of variable hot dust content are the two values of $C_{2\text{ norm}}$ we get for NGC 4151 from Schnülle et al. (2015). The time lag in these

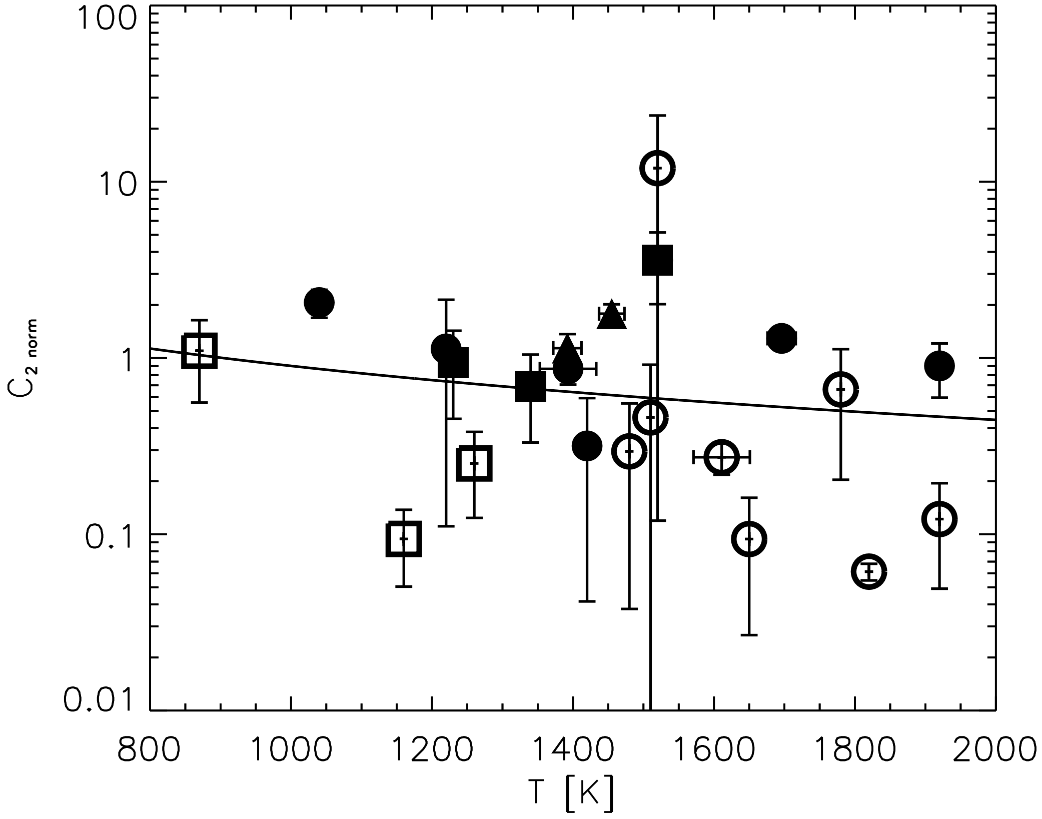

Figure 3.13 Normalized dust surface area $C_{2\ \mathrm{norm}}$ as a function of the dust temperature T. Filled (open) circles represent AGN without (with) host extinction. The squares represent AGN with τ determined using the dust temperature and L_V (compare Table 3.4). Marked with triangles are the results from Schnülle et al. (2015) for NGC 4151. $C_{2\ \mathrm{norm}}$ was determined using Eq. 3.17. The solid line shows the best power law fit in the form of $C_{2\ \mathrm{norm}} \propto T^{-0.9\pm1.3}$.

two epochs are 42.5 ± 4.0 ld and 29.6 ± 1.7 ld, and the epoch with the smaller radius shows increased $C_{2\ \mathrm{norm}}$ dust surface area. Both variations hint to additional clouds and local dust production as origin of the reduced radius and increased surface area. While the measured cloud dust temperatures around 1400 K seem too high, more favorable conditions for dust production are present within the outer parts of the accretion disk at these radii Czerny & Hryniewicz (2011); Czerny et al. (2017).

All values of $C_{2\ \mathrm{surface}}$ significantly below the fit are AGN showing signs of host extinction. A slight overestimation of the dust temperature, as discussed in Section 3.5.1, and thus an underestimation of the surface area is possible. We tested this with a fixed value of $\alpha = 2$. Only in the case of H 2107-097 (dark yellow open

Table 3.5 Radial extend of the dust torus in units of the measured dust radius for each AGN. The measured delay was assumed to coincide with the inner radius of the dust torus for this. The values were calculated using Eq. 3.18.

	3C273	Ark120	ESO 323-G77	ESO362-G18
$C_{2\ \mathrm{norm}}$	0.9 ± 0.3	1.29 ± 0.06	0.12 ± 0.07	2.06 ± 0.37
	ESO383-G035	Fairall 51	H0557-385	H1934-063
$C_{2\ \mathrm{norm}}$	0.25 ± 0.13	0.30 ± 0.26	1.1 ± 0.5	0.7 ± 0.4
	H 2107-097	MCG-01.13.025	Mrk 1239	Mrk 50
$C_{2\ \mathrm{norm}}$	0.09 ± 0.04	0.7 ± 0.5	12 ± 12	1.1 ± 1.0
	Mrk590	Mrk704	NGC3227	NGC 3783
$C_{2\ \mathrm{norm}}$	0.061 ± 0.007	0.9 ± 0.3	0.27 ± 0.06	0.3 ± 0.3
	NGC 4235	NGC 4593	NGC 5548	UGC 3223
$C_{2\ \mathrm{norm}}$	0.5 ± 0.5	3.6 ± 1.6	0.87 ± 0.16	0.09 ± 0.07
		NGC 4151 1	NGC 4151 2	
$C_{2\ \mathrm{norm}}$		1.1 ± 0.2	1.8 ± 0.2	

square in Fig. 3.12), a significant influence on the surface area was found with a factor of three larger surface area. Thus, fixing α to a sample-typical value reduces the $C_{2\ \mathrm{surface}} - \tau$ scatter moderately.

The observed scatter in the $C_{2\ \mathrm{surface}} - \tau$ relation can derive from different viewing angles and cloud filling factors of the toroidal hot dust volume. The extreme cases would be dust poor AGN for which dust is not detectable at all (ESO 377-G24 in our sample) or only barely (e.g. Mrk 590). Similar differences are likely for the BLR clouds as well (compare Chapter 4). In the chapter, we discuss how valuable parallel studies of the hot dust and the BLR are to test the scenario of a common origin of BLR and torus clouds (e.g. in the AD as proposed for the BLR by Czerny & Hryniewicz 2011; Czerny et al. 2017). Studies of the BLR evolution could be helpful to learn more about cloud filling factors because we can get azimuthal information on the distribution of BLR clouds from their velocity distribution (e.g. Gravity Collaboration et al. 2018 and see also Chapter 4). Such source-dependent cloud distributions also can have a significant influence on the determination of BH masses in AGN as they change the f-factor.

3.7 Summary and conclusions

We have used multiwavelength dust reverberation mapping to determine dust time lags with concurrent measurements of the dust temperature and the surface area of the dust for AGN with $z < 0.2$. For 14 out of 25 AGN in the sample we were able to determine reliable time lags and dust temperatures, while for six additional sources, the data only allowed to determine the dust temperature. We used the radius luminosity relation, determined in this work, to calculate their time lag. The mean dust temperatures are in a range between 900 and 1900 K. Such high temperatures suggest graphite-only dust grains in the innermost circumnuclear AGN dust.

We find typical values for the slope and intercept of the radius luminosity relation, including a slope slightly smaller than the expected $\tau \propto L^{0.5}$ towards large radii, corresponding to high-luminosity AGN. The measurements presented in this chapter however can explain this slope as a dust temperature bias effect, independent of the AGN luminosity. The determined dust temperatures allow us to correct for the effect that hotter dust is expected to reside closer to the AD. With a normalization of the form $\tau \propto T^{-2.8}$ the slope of the radius luminosity relation becomes steeper to be in very good agreement with the expected $\tau \propto L^{0.5}$, and its scatter around the relation is reduced by 50% thanks to the simple temperature normalization. Thus, acknowledging the fact that the hot dust in an AGN can have quite a diverse temperature, and that it is not always located at the sublimation radius, it is important to precisely measure the circumnuclear cloud distribution.

While we get a well constraint radius luminosity relation with multiwavelength dust reverberation mapping, the surface area of the hot dust shows significantly larger scatter with the parameters we can determine. This indicates that properties of the hot dust morphology, such as the (probably evolving) cloud filling factor are relevant and change from object to object. We find a number of AGN, which are extremely (hot) dust-poor or even dust-free.

If the source-dependence of the circumnuclear dust cloud distribution is representative for the BLR clouds as well, then the hot dust tori studied in this chapter do not support the picture of a simple, static and typical circumnuclear cloud geometry, which complicates the derivation of BH masses from BLR reverberation datasets. In our sample, Mrk 590 shows very low dust emission. This is accompanied by an underluminous BLR, supporting the notion of a coevolution of BLR and dust torus clouds. Alternatively, the dust content of the clouds might change more rapidly than the gas clouds under the influence of illumination by the accretion disk. In the case of NGC 4151, Schnülle et al. 2015 have found changes in the dust properties on short timescales. While the inner radius of the dust torus decreased, our determination of $C_{2\ \mathrm{norm}}$ increases. This can be best explained with a constant geometry of the outer parts of the hot dust and additional dust appears within the former inner radius. The dust temperatures suggest dust production is taking place in the AD as already mentioned by Schnülle et al. (2015). Dust production above the AD is also disfavored by the dust temperatures in our sample. Only few sources show temperatures around and below 1000 K, needed for this production mechanism.

Only the presented multiwavelength reverberation mapping approach can reliably decouple the effects of temperature and radiating dust surface on the NIR dust SED. Apart from being able to improve the radius luminosity relation by the novel temperature normalization, the ability to constrain the dust temperature and surface area simultaneously can help our understanding of the physical processes in circumnuclear clouds.

CHAPTER 4

Analyzing temporal variations of AGN emission line profiles in the context of (dusty) cloud structure formation in the broad line region

4.1 Introduction

Gas clouds located in the BLR rotate around the black hole at velocities up to a few 10,000 km s^{-1}. Variations of both the overall flux and the shape of the BEL have been reported (e.g., Sulentic et al. 2000; Shapovalova et al. 2010; Ilić et al. 2015). In all the publications mentioned BELs at optical wavelengths were used, but here we have used NIR spectra. This is primarily due to data availability, but it also allows us to compare the shape variations found in the optical by Shapovalova et al. (2010) for NGC 4151 to shape variations in the infrared and prominent BELs such as Paβ are not contaminated by emission lines of other chemical species (Landt et al. 2011a).

The variations of the shape of the broad emission lines can be explained by a changing and non-symmetrical distribution in azimuthal direction of those clouds in the BLR or inflows and outflows of gas clouds. A theoretical description of the relation between cloud distribution in the BLR and the resulting BEL flux is presented in Stern et al. (2015). However Stern et al. (2015) describe an azimuthally averaged temporal mean cloud distribution in radial direction, which we have modified to allow for the localized temporal profile shape variations observed.

In this chapter we describe a possible connection between the variability of the BELs shape of NGC 4151 to the changes of the dust radius found by Koshida et al. (2009). We are unable to get any information on the azimuthal distribution of dust clouds from their emission as long as we are unable to resolve this directly (with interferometry). Therefore it is crucial to know whether changes of dust torus and BLR occur simultaneously. If so it would indicate a common origin and also potentially similar azimuthal cloud distributions of dust torus and BLR, leading to a better understanding of changes of dust radii and dust production in AGN.

In Section 4.2 we describe how the BELs were extracted from the observed spectra for our analysis. This is followed by the description of the BEL profile variability in Section 4.3 and how we can model the observed BELs of NGC 4151 using (and expanding) the simple parametrization of the BLR from Stern et al. (2015) in Section 4.4. In Section 4.5 we discuss what these results suggest about how dust and the BLR is created in the inner AGN region. A summary of our findings will be given in Section 4.6.

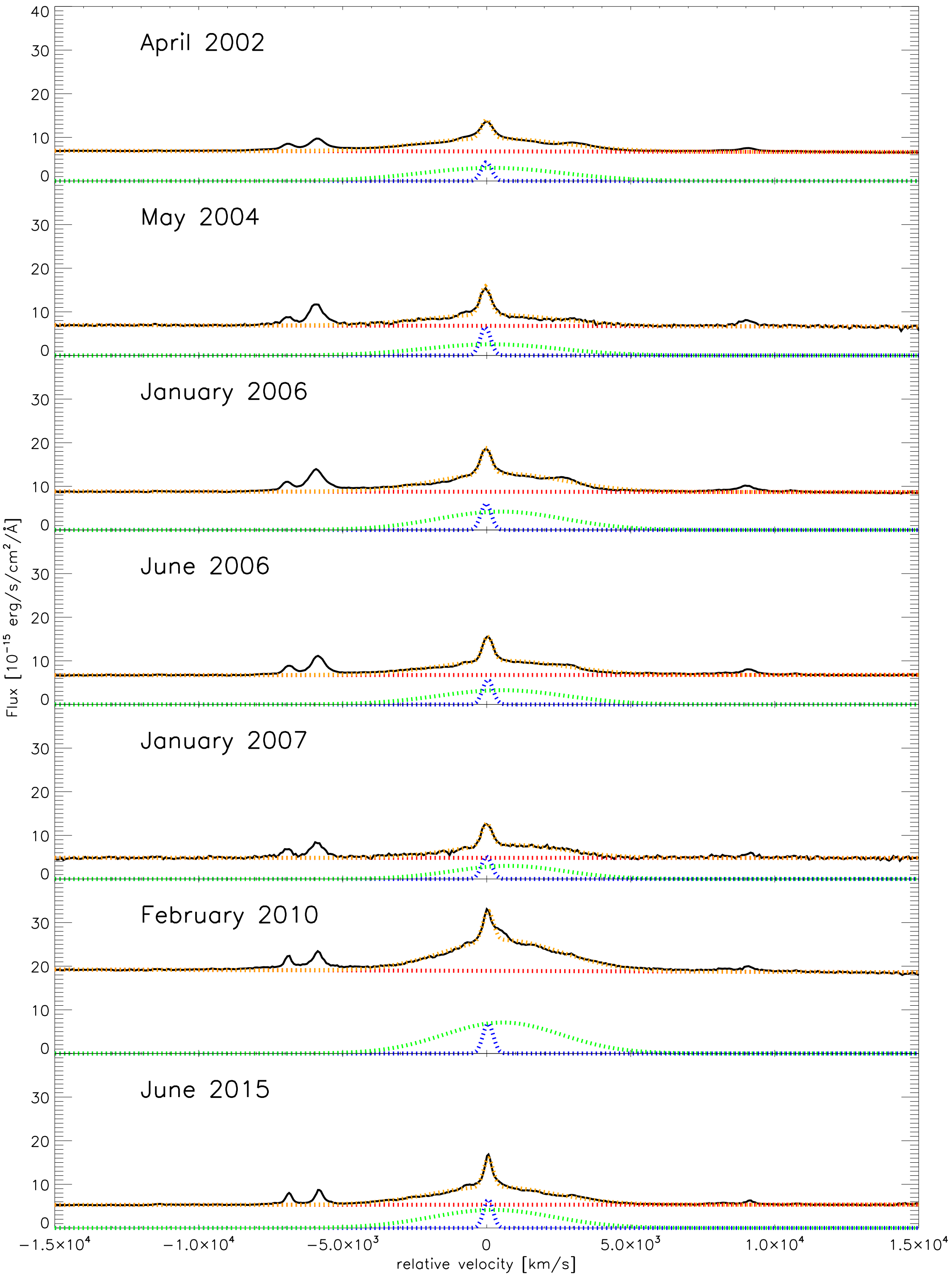

Figure 4.1 Environment around the Paβ line in each spectrum. The data is shown in black along with the NEL fit (blue), BEL fit (green), continuum fit (red) and the sum of those fits (orange).

4.2 Data reduction

All spectra used here were taken with the SpeX spectrograph (Rayner et al. 2003) at the NASA IRTF. They were obtained between April 2002 and June 2015 using the short cross-dispersed (SXD) mode with a wavelength range of 0.8-2.4 μm. All spectra were reduced using Spextool (Cushing et al. 2004). The 2002 spectrum was published by Riffel et al. (2006) and the next four spectra were used by Landt et al. (2008, 2011b). Information about the observations and the resulting spectra are given in Table 4.1. More details and information on the reduction process are provided by Riffel et al. (2006) and Landt et al. (2008). The sixth epoch from February 2010 has already been used by Schnülle et al. (2013). The last spectrum was reduced in the same way as the sixth and both spectra were calibrated as described by Vacca et al. (2003). There is an additional spectrum from February 2015 from Wildy et al. (2016) but not much changes in it compared to the June 2015 spectrum and as the June 2015 spectrum has a much better signal-to-noise ratio (S/N), especially important for weaker BELs, we decided to not include this here.

For the selection of the lines used in this chapter several criteria had to be met: First the BLR flux had to be sufficiently high to assure S/N of at least 30 at the peak of the continuum subtracted BEL to enable us to see the shape variations of the BELs. Furthermore, in order to get a good fit of the continuum flux, a region without any other emission lines had to be located close to the examined emission line. Emission lines with wavelength above 2.4 μm could not be taken into account as only the two newest spectra include this wavelength range. In the end we were left with three emission lines best suited for our analysis which largely fulfilled these requirements. These three lines were Paβ, O I 844 nm and Brγ. However, the mentioned S/N could be reached only for the Paβ line. For the other two lines the S/Ns are below 20. Therefore we largely focus on the Paβ line in this chapter but the other two lines are also mentioned, to point out the similar changes in those lines.

In order to obtain the flux originating from the BLR the continuum flux as well as the flux from the NLR had to be subtracted. In order to get a good approximation of the continuum flux at the particular emission line we apply a linear fit to a region which is free of emission lines from -14,000 to -8000 km s^{-1} and 8000 to 14,000 km s^{-1} from the emission line. In the case of Paβ we can only use a range between ±10,000 and ±14,000 km s^{-1} due to Fe II and S IX emission around 1.26 μm (visible in Fig. 4.1 to the left of the BEL). Flux from the NLR was determined using a Gaussian fit. The results for the FWHM of that fit are shown in row

10 of Table 4.1. The fitted FWHM of the NEL profile is dominated by the effective resolution of the spectra and varies typically by only ±1 pixel around the mean. Only the April 2002 spectrum was an exception to this as the spectral resolution is a bit lower. To minimize the influence of the BLR profile variability onto the NEL fit, we re-fit the spectrum with a NEL Gauss profile of constant width equal to the mean of the individual FWHM fits for all but the 2002 dataset.

In the case of the 2002 spectrum the individually measured FWHM was used. However the NEL flux was not constant for our spectra (most likely due to inaccuracies in the flux calibration) and was therefore left as a free parameter in the fits. The fits for each spectrum are shown for the Paβ line in Fig. 4.1. The resulting BEL plots with NEL and continuum subtracted are shown in Fig. 4.2 (Paβ), Fig. 4.3 (O I 844 nm) and Fig. 4.4 (Brγ). In the velocity range of the NEL small bumps can be seen for each spectrum. In most cases it is hard to confirm whether these bumps are caused by shape variations of the emission lines as they could also be caused by residuals of the NEL fit. Especially in the February 2010 case a shape variation can be seen to the right of the NEL in Fig. 4.1. So while it is possible that there are BEL shape variations around the NEL (i.e., at low velocities), we will concentrate on the variations in the red wings as they are unaffected by the NEL fit.

Table 4.1 Journal of observations for our IRTF SpeX spectra.

Date	MJD - 50,000	Exposure (s)	Airmass	Continuum S/N[a] J	H	K	Mode	slit size	FWHM Paβ NEL[b] km s^{-1}
2002 Apr 23	2387	1800	1.10	189	303	406	SXD	0.8" x 15"	700
2004 May 23	3148	720	1.13	32	45	121	SXD	0.8" x 15"	560
2006 Jan 08	3743	1920	1.07	103	212	345	SXD	0.8" x 15"	490
2006 Jun 12	3898	1200	1.22	109	202	269	SXD	0.8" x 15"	420
2007 Jan 24	4124	960	1.45	15	54	113	SXD	0.8" x 15"	420
2010 Feb 27	5254			182	226	363	SXD	0.3" x 15"	400
2015 Jun 23	7076	2520	1.09	150	163	250	SXD	0.3" x 15"	400

Notes. The columns show the date of observations, the exposure times, the airmass, the S/N at different wavelength, spectrograph mode, the slit size used and the FWHM of the Paβ NEL.

[a] S/N in the continuum over ~ 100 Å measured at the central wavelength of the J, H and K band.

[b] This NEL FWHM was fitted with a Gaussian profile to the individual spectra. Part of the FWHM variation between the epochs is due to cross-talk between the NEL FWHM fit, and the variable BEL profile superposed onto the fixed NEL profile. The mean of the measured FWHM of the 2004 to 2015 spectra is 450 km s^{-1}.

4.3 BEL shape variation

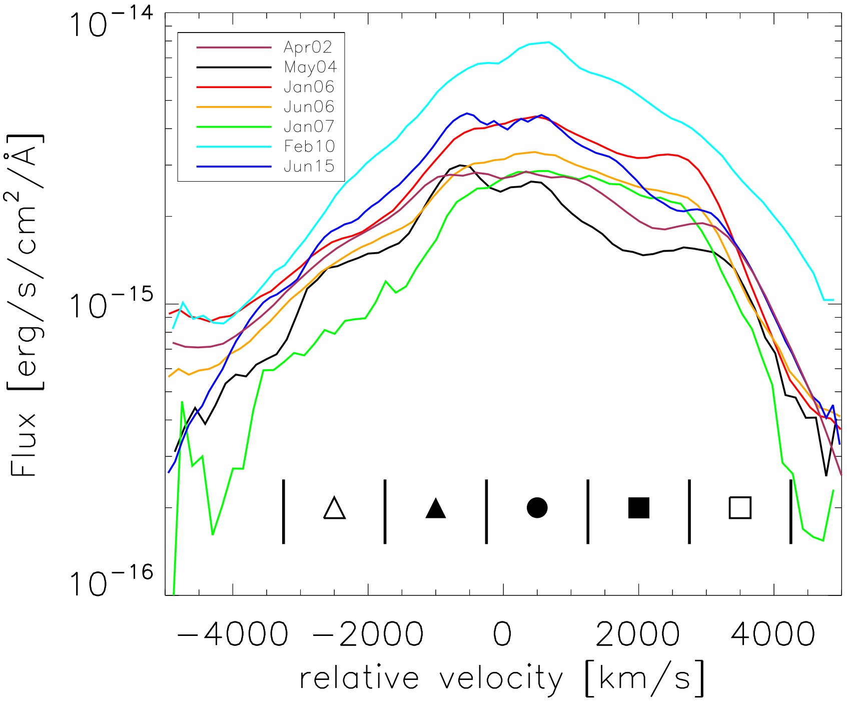

Figure 4.2 Paβ BEL for our seven observation epochs. The color coding for the epochs is shown in the upper left corner of the plot. The subtraction of the NEL and continuum flux are described in Section 4.2. Wiggles can be seen for most epochs approximately at the center of the BEL. We cannot rule out that these are residuals from the NEL subtraction. Therefore it is not possible to tell whether these shape variations originate in the BLR. At the bottom of the figure the velocity bins used for Fig. 4.7 are shown and color coded from blue to red. The strongest shape variations can be seen in the red shifted part of the BEL especially around velocities of 2500 km s^{-1}.

4.3.1 Testing the temporal stability of the BEL profile

The evolution of BEL profiles across the seven epochs are presented in Figs. 4.2 (Paβ), 4.3 (O I 844 nm) and 4.4 (Brγ). Of these BELs, the Paβ line has the highest flux and S/N. The S/N of the O I 844 nm line is further reduced due to the higher continuum flux (so lower line-to-continuum-ratio) at these wavelengths compared to the Paβ line and especially at the Brγ line the continuum flux is much lower. Therefore, the further analysis is done for the Paβ line alone while it is done for the sum of the O I 844 nm and Brγ line to increase the S/N. The general findings are similar.

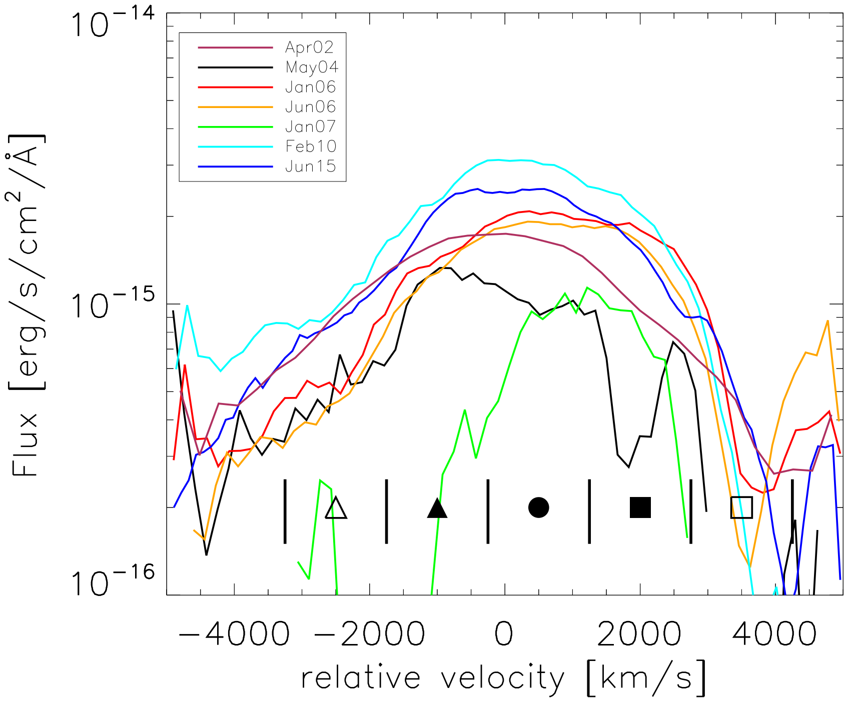

Figure 4.3 Same as Fig. 4.2 for the O I 844 nm BEL.

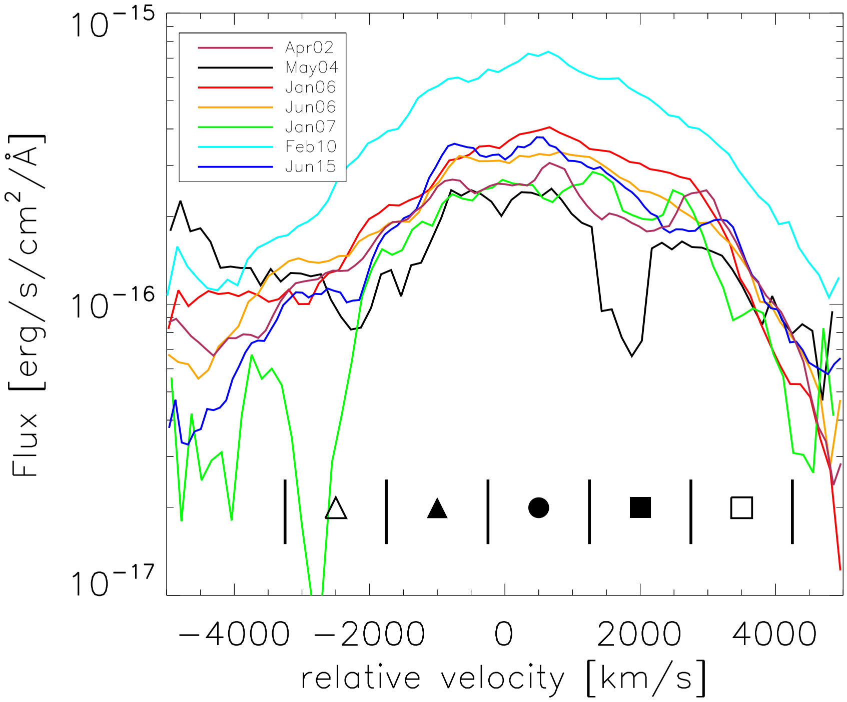

Figure 4.4 Same as Fig. 4.2 for the Brγ BEL.

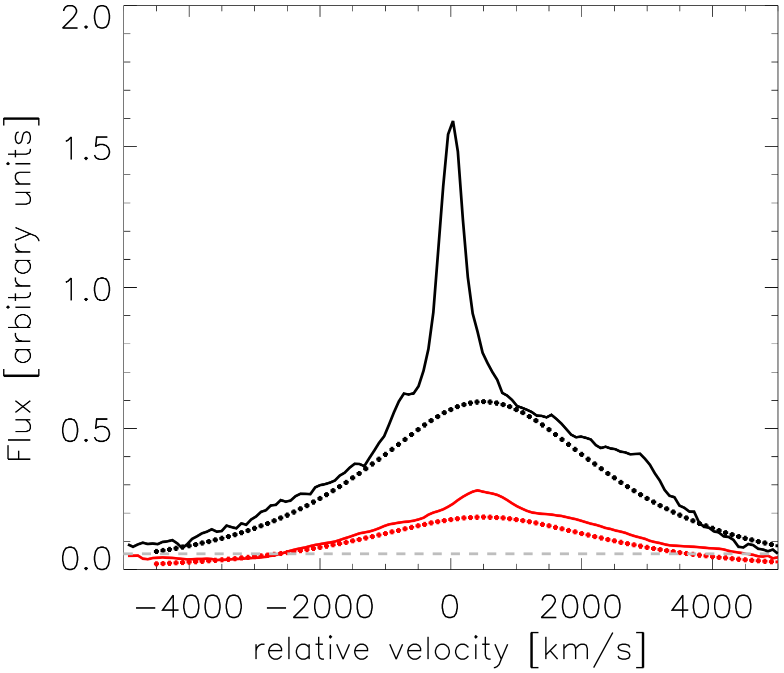

Figure 4.5 Mean (black solid line) and rms (red solid line) profile for the Paβ line of all spectra despite the April 2002 spectrum (which had to be excluded here due to its lower spectral resolution). Along with this a model of a symmetrical BEL was plotted which we develop in Section 4.4 (red and black dotted lines) based on Stern et al. (2015). The gray dashed line shows the median flux error of individual pixels at the Paβ line.

Apart from the overall flux changes a variation of the BEL shape can be seen in the red wings. During the first five epochs (from April 2002 to January 2007) a peak is apparent that flattens out with time and can no longer be seen in the February 2010 epoch. In the June 2015 epoch a similar peak appears again at the red wing. The apparent variations around the center of the BELs were already briefly addressed at the end of Section 4.2 and might be partly caused by residuals from the fit of the NELs. Our data does not sample strong shape variations in the blue wing. Similar emission peaks are found for the Hα and Hβ BELs of NGC 4151 by Shapovalova et al. (2010) at the same time as our IR spectra were taken at the red wings and also at earlier times in the red wings only.

In order to measure the significance of these variations we used the rms profile of our spectra. For the classical rms approach the fitted NEL flux was normalized in order to have a constant NEL flux for all spectra and the April 2002 spectrum had to be excluded due to its lower spectral resolution. The resulting mean and rms profiles are shown in Fig. 4.5 along with a symmetrical BEL model which we develop in Section 4.4, based on the work of Stern et al. (2015). In Fig. 4.5 it becomes apparent that the mean profile of our Paβ emission line shows a significant shape discrepancy from the symmetrical profile in the red wing compared to the blue wing. Additionally the rms profile is slightly stronger in the red wing. If there were no shape variations it would be expected that the rms profile should be similar to the symmetrical profile. Nonetheless this approach of analyzing the rms spectral shape is not ideal to identify shape variations, since it mixes BEL flux variation with line profile shape variation.

As we look for shape variation alone in these profiles we need to normalize the spectra in order to get rid of the overall flux changes of the BELs. For this it is necessary to subtract the constant part of the emission line, namely the NEL, first. We then introduced a fit parameter (which acts as a normalization factor) for each spectrum (p_i) where the fit parameter for the May 2004 spectrum is fixed to 1.0. We then minimized the following rms profile:

$$rms = \frac{\sum_{i=1}^{6}(p_i F_i(\lambda) - \overline{F}(\lambda))/(p_i \sigma_{F,i}(\lambda))^2}{\sum_{i=1}^{6}(1/(p_i \sigma_{F,i}(\lambda)))^2} \tag{4.1}$$

where $F_i(\lambda)$ is the BEL flux and $\sigma_{F,i}$ is the error of the BEL flux. $\overline{F}$ is the weighted mean flux of the seven spectra defined as

$$\overline{F}(\lambda) = \frac{\sum_{i=1}^{6} p_i F_i(\lambda)/(p_i \sigma_{F,i}(\lambda))^2}{\sum_{i=1}^{6}(1/(p_i \sigma_{F,i}(\lambda)))^2} \tag{4.2}$$

At first we determine the rms profile using the complete BELs. The resulting fit parameters p_i are shown in Table 4.2 and the resulting rms (multiplied by a factor of three for better visibility) is shown in the left plot of Fig. 4.6 (dashed gray line) along with the spectra multiplied with their respective fit parameter (solid colored lines as in Fig. 4.2) and the weighted mean Flux (solid gray line). Looking at this rms profile we find two velocity ranges now where the variations are strong. For the first one around 0 km s^{-1} we can not easily tell to what extent these variations are real variations of the BELs or instead residuals from our NEL fit. Therefore we do not discuss them further here. The second peak of the rms profile is located in the region where the bumps discussed before can be seen from 2000 to 3000 km s^{-1}.

In the next step, we excluded those velocity ranges where the rms profile peak and repeat the process determining the rms profile as shown above. We do this as we want to include only the parts of the BELs which do not change their shape in the fitting process to avoid a biased flux normalization. The results of this second iteration are shown in the right plot of Fig. 4.6 and the fit parameters p_i^* are given in Table 4.2. This does not strongly affect our fit parameters however p_i is

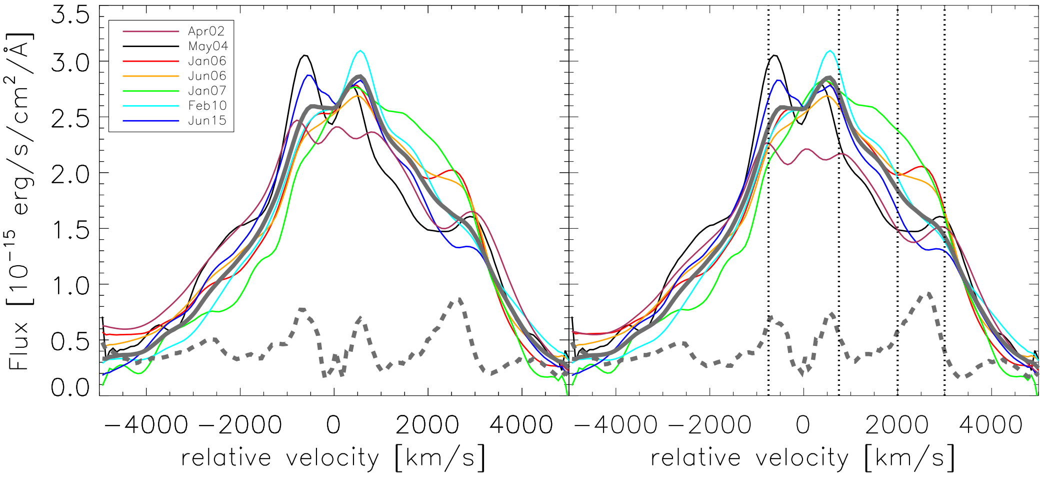

Figure 4.6 Paβ BELs normalized with the fit parameters from the rms minimization (Eq. 4.1) which are given in Table 4.2. The color coding of the BELs is given in the upper left corner. Additionally the mean spectrum (solid gray line) and the rms profile (dashed gray line) are shown. For better visibility the rms profile was multiplied by a factor of three. In the left plot the full BEL was used for the rms minimization. In order to make the minimization less sensitive to the shape variations of the BEL the indicated velocity ranges between -750 to 750 km s^{-1} and 2000 and 3000 km s^{-1} were excluded from the minimization in the right plot as the rms profile is largest in these regions indicating the strongest shape variations.

systematically smaller than p_i^* with the exception of p_0 and with p_4^* having the largest increase. Especially on the blue wing the spectra are pushed together by this change. However at velocities between 0 and 2000 km s^{-1} the normalized flux of the May 2004 BEL (black line) is even further below the mean BEL while the normalized flux of the January 2007 BEL is even higher than the flux of the mean BEL. A similar behavior can be seen for the flux ratios compared to the May 2004 BEL. Excluding the varying parts of the BELs leads to a general increase in the flux ratios which is especially pronounced for the January 2007 BEL (compare rows 4 and 5 of Table 4.2).

We conclude that the BEL profile variation appears to be particularly pronounced between velocities of 2000 and 3000 km s^{-1}.

4.3.2 Time evolution of the BEL profile

We divided our BELs in five equal velocity bins from -3250 to 4250 km s^{-1} (indicated by the symbols at the bottom of Figs. 4.2, 4.3, and 4.4). The bins are not centered around 0 km s^{-1} as the BELs are shifted by approximately 500 km s^{-1}

Table 4.2 Overview of the fit parameters obtained by the minimization of the rms profile (Eq. 4.1) and the flux ratios of the Paβ BELs. In the second column the fit parameters are shown for the complete BEL and in the third column the fit parameters if the velocity range with high rms (compare Fig. 4.6) are excluded. The flux ratios are shown for both of these cases as well with respect to the May 2004 BEL.

Date	p_i	p_i^*	F_1/F_i	F_1^*/F_i^*
2002 Apr	0.81	0.78	0.81	0.81
2004 May	1.00	1.00	1.00	1.00
2006 Jan	0.60	0.63	0.62	0.65
2006 Jun	0.76	0.79	0.78	0.81
2007 Jan	0.89	0.95	0.98	1.08
2010 Feb	0.38	0.38	0.39	0.40
2015 Jun	0.61	0.63	0.63	0.66

with respect to the NELs. This velocity shift of the BELs with respect to the NEL center is also found by Shapovalova et al. (2010). We then integrated the flux in those bins as well as the overall flux from the BEL to get the ratio of those two values. This ratio is plotted in Fig. 4.7 over time for the Paβ BEL. Due to the lower S/N for the O I 844 nm and Brγ BELs we take the average of the ratios of the two lines for the same plot (Fig. 4.8). We decided not to take the sum of the fluxes to then get a combined average here as this would have lead to a higher weighting of the O I 844 nm line due to the higher flux of that BEL. The ratios are indicated by the different symbols which are also given at the bottom of the figures showing the BELs (Fig. 4.2, 4.3, and 4.4).

It can be seen in Fig. 4.7 that the relative flux in the central bin and the bin centered around 2000 km s^{-1} stays approximately constant between April 2002 and May 2004 and than gradually increases from the May 2004 BEL to the January 2007 BEL. The February 2010 BEL on the other hand shows an almost symmetrical BEL again (if 500 km s^{-1} is assumed as the center of the BEL). This supports the result from the rms profile of strong shape variations between May 2004 and January 2007. Additionally it shows that this change does not evolve randomly but the BEL flux in the red wing steadily increases.

Another feature in the BELs appears similar to an absorption of flux at 2000 km s^{-1} in the first period especially for the O I 844 nm and Brγ BEL. For the Paβ line it is not possible to tell whether the impression of a slightly lower flux is caused by the enhanced flux at 3000 km s^{-1}. However as we definitely see this feature in two out of three BELs at the same velocities, this could be a real absorption-like feature. It is also possible that this is caused by a lower emission at these velocities. However

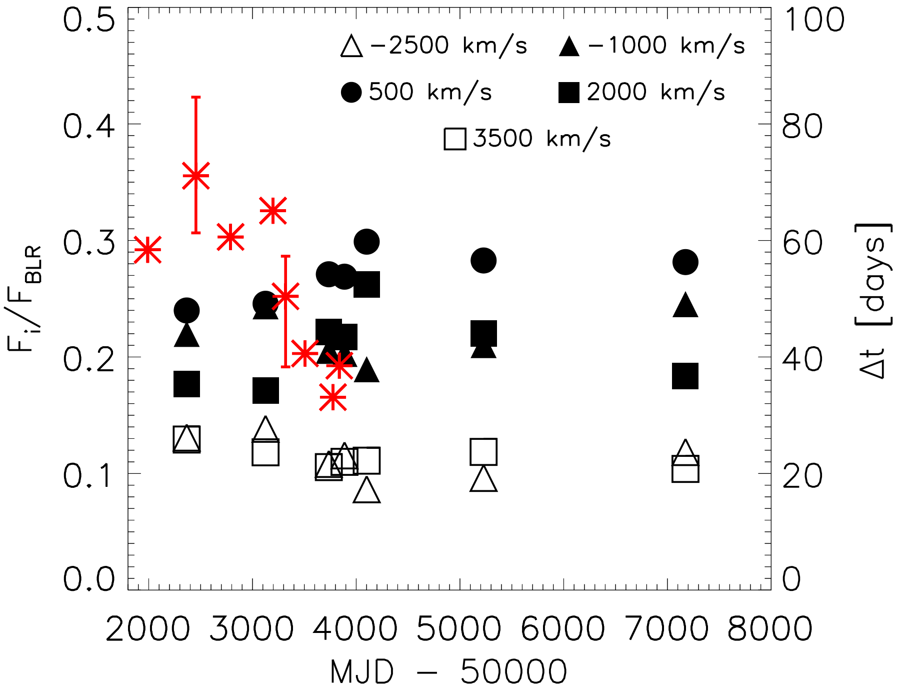

Figure 4.7 Fluxes in different velocity bins (F_{ij}) over the total flux from the Paβ BEL (F_i) over time for the seven spectra. The different symbols indicate the different velocity bins which are also given at the bottom of Fig. 4.2 and their central velocity is given at the top of the plot. The error bars are smaller than the symbols except for two of dust radii where the error bars are given. Indicated with the red stars are the radii of the last five epochs determined by Koshida et al. (2009). For those the reverberation delay in ld is plotted against time. At the same time the radius of the dust torus is reduced by a factor of approximately two, and the relative flux in the bin between 1250 and 2750 km s^{-1} (orange crosses) increases significantly.

the rms is significantly higher above 2000 km s^{-1} (compare Fig. 4.6) and we therefore concentrate on the variations between 2000 and 3000 km s^{-1}. For the same reasons we neglect the slight shape variations in the blue wing. This shows that (slight) BEL shape variations are occurring throughout the BEL but are most significant between 2000 and 3000 km s^{-1}. There are some shape variations around 0 km s^{-1} too, but these could be attributed to the NEL fit. Therefore, we cannot attribute these features cleanly to the BLR and we do not discuss them further in this chapter.

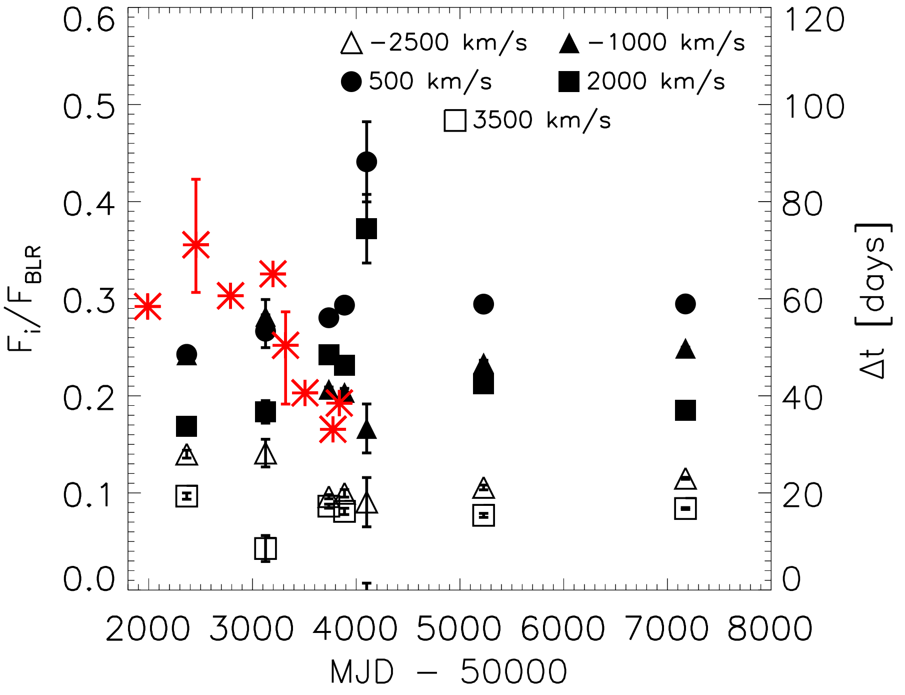

Figure 4.8 Same as Fig. 4.7 but for the sum of the ratios of the O I 844 nm and the Brγ BELs which are shown in Figs. 4.3 and 4.4. We use the sum of the two BELs to increase the S/N as the strength of those lines is much weaker than the Paβ line. A similar increase of the relative flux in the 1250 to 2750 km s^{-1} bin (filled squares) can be seen for the O I 844 nm and Brγ BEL.

4.4 Modeling BELs

Next we want to use the simple geometric parametrization of the BLR intensity distribution as described in Stern et al. (2015) to reproduce our BELs of NGC 4151. For the rest of the section, we have used this approach to model the overall BEL profile, and extend it to realize the secondary peak observed. Of our seven spectra we chose the January 2006 spectrum as it is the highest S/N spectrum taken in the time period showing line profile variability. Additionally it shows a significant bump in the region were the rms profile is the highest (Fig. 4.6) and this spectrum was taken at a time when the radius of the dust torus determined by Koshida et al. (2009) was at a minimum. In total this BEL has the potential to provide the most information. The other BELs from this epoch show a similar overall width and a similar width of the bump (apart from the January 2007 BEL), although the bump intensity and location slightly changes. In order to do this we took Eq. 16 of Stern et al. (2015) describing the flux density of photons per unit velocity (v) that originate from the disk coordinate (r, φ):

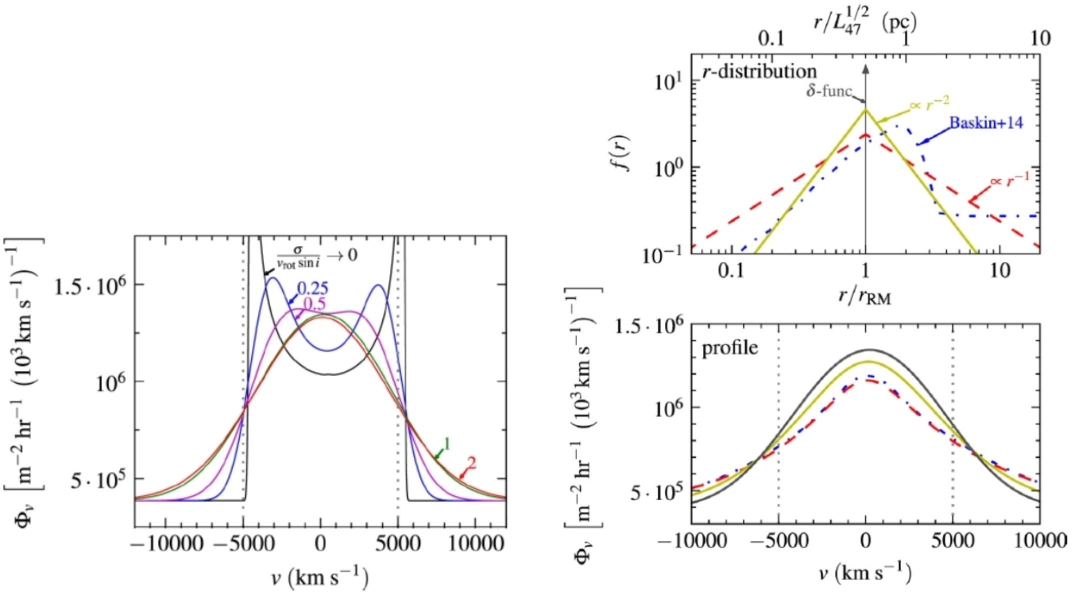

Figure 4.9 Dependence of the shape of BELs on the velocity dispersion σ (left plot) and the radial density profile (right plot) of the BLR clouds. Both plots are taken from Stern et al. (2015).

$$\Phi_v^*(r,\varphi) = \frac{f(r)}{r} e^{-\frac{(v_{\rm rot}\sin i)^2}{2\sigma_v^2}\left(\sin\varphi - \frac{v}{v_{\rm rot}\sin i}\right)^2} . \tag{4.3}$$

In this equation $f(r)$ describes the radial distribution of the line emission while the exponential function describes the local line broadening due to the non-rotational velocity components (σ_v) in the BLR with i being the inclination between the AD and the line of sight and $v_{\rm rot}$ the rotational velocity (which is proportional to $r^{-0.5}$ as the gravitational field is dominated by the central black hole).

In the left plot of Fig. 4.9 the influence of $\sigma_v/(v_{\rm rot}\sin i)$ on the shape of the BEL is shown. For values lower than one, the BEL is double peaked and for values above one the shape becomes single peaked without significant further changes for larger $\sigma_v/(v_{\rm rot}\sin i)$. Double peaked BELs are seen only if the FWHM reaches values above 10,000 km s^{-1} (e.g., Eracleous & Halpern 2003). Therefore we choose $\sigma_v/(v_{\rm rot}\sin i) = 1$. The radial distribution of line emission is described by $f(r) \propto r^1$ for $r < r_{\rm BLR}$ and $f(r) \propto r^{-1}$ for $r > r_{\rm BLR}$, where $r_{\rm BLR}$ is the BLR radius measured with reverberation mapping. The changes of the BELs due to different radial distributions can be seen in the right plot of Fig. 4.9. We choose this distribution as it is the widest of the given distributions in Stern et al. (2015) and reproduces the overall shape of our BELs well. Thus we do not overestimate the rotational velocity of the BLR clouds. Applying a steeper radial profile, for example $f(r) \propto r^{\pm 2}$), requires an increase of the rotational velocity by only 100 km s^{-1}.

The inner and outer radius of the luminous BLR clouds are adopted from Baskin & Laor (2018) with values of $r_{\text{in}} = 0.18\, r_{\text{BLR}}$ and $r_{\text{out}} = 1.6\, r_{\text{BLR}}$. The choice of r_{in} and r_{out} slightly influences the shape of the BEL as well. For example, a larger r_{out} leads to additional relatively slow clouds inducing a narrower BEL hence increasing the necessary rotational velocity to reproduce the width of our BELs. A larger r_{in} has a similar effect because the fastest clouds are removed. The inner and outer radii were determined for a constant AGN luminosity by Baskin & Laor (2018). However, the optical lightcurve of NGC 4151 (e.g., Shapovalova et al. (2008); Koshida et al. (2009)) is not constant at all. Therefore BEL clouds might be present outside those radii depending on the earlier luminosities of NGC 4151 and the timescales on which BEL clouds are created and afterwards stop contributing to the BEL flux (for example by falling back to the AD). As those timescales are not well understood, we use the radii from Baskin & Laor (2018).

This simple description of the BLR reproduces the overall shape of the Paβ lines very well. As the overall shape and width of the Paβ line does not change too much with time (compare Fig. 4.6) we only show the comparison to the January 2006 Paβ line in the upper left plot of Fig. 4.10. Shapovalova et al. (2010) also find that the FWHM of the BELs of NGC 4151 does not show strong changes (the FWHM only becomes smaller for a short time in 2000) despite the significantly reduced flux in a ten year span from 1996 to 2006.

Next we want to reproduce the January 2006 spectrum with a separate peak around 2600 km s^{-1} in addition to the main Gaussian profile. We note that the center of the Paβ BEL is shifted by $v_{\text{shift}} = 500$ km s^{-1} with respect to the center of the narrow line. The modeled flux was normalized to match the maximum observed flux in all plots of Fig. 4.10.

This process should not be understood as a fit to the data, which is difficult to interpret since the parameters are partly correlated. As we will show below, some of the elements of Eq. 4.3 have a similar effect on the BEL shape (e.g., the cloud distribution in r and $v_{\text{rot}} \sin i$). Therefore a fitting process could not distinguish between those parameters any way. Rather we want to explore how the Stern et al. (2015) description of the BLR has to be tweaked in order to reproduce such a narrow bump, to explore the spatial information encoded in the BEL velocities.

Equation 4.3 can well reproduce the BEL beside the bump and at velocities below -3000 km s^{-1} with $v_{\text{rot}} \sin i = 1500$ km s^{-1} (upper left plot of Fig. 4.10). To be able to describe features in the BELs like the peak present at the red part of the January 2006 Paβ line (compare also Fig. 4.2) we need to vary the cloud distribution in azimuthal direction as well, adding a function $g(\varphi)$ to Eq. 4.3:

Table 4.3 Summary of the parameter space of our BEL modeling described in Eq. 4.6. The parameters are given together with the values we used to reproduce Fig. 4.10 and a short description. Some of these parameters were varied in Fig. 4.10.

	BEL cloud distribution	
Label	Best value	Description
$f(r)$	$r^{\pm 1}$	radial distribution of BLR emission
$f_2(r)$	$r^{\pm 2}$	radial distribution of BLR emission for additional clouds
r_{in}	$0.18\ r_{\mathrm{BLR}}$	inner radius of BLR (Baskin & Laor 2018)
r_{out}	$1.6\ r_{\mathrm{BLR}}$	outer radius of BLR (Baskin & Laor 2018)
$g(\varphi)$	Gauss function	azimuthal distribution of BLR emission for additional clouds
$\varphi_{C,2}$	$0.5\ \pi$	center of the Gauss function
$\sigma_{\varphi,2}$	0.45	width of the Gauss function
	BEL cloud velocities	
Label	Best value	Description
v_{rot}	1500 km s^{-1}	rotational velocity of BLR clouds
$\sigma_v/(v_{\mathrm{rot}} \sin i)$	1	velocity dispersion or local line broadening term of BLR clouds
$v_{\mathrm{rot},2}$	2500 km s^{-1}	rotational velocity of additional BLR clouds
$\sigma_{v,2}/(v_{\mathrm{rot},2} \sin i)$	0	velocity dispersion or local line broadening term of additional BLR clouds

$$\Phi_v^*(r,\varphi) = \frac{f(r)}{r}(g(\varphi)+1)e^{-\frac{(v_{\rm rot}\sin i)^2}{2\sigma_v^2}\left(\sin\varphi - \frac{v}{v_{\rm rot}\sin i}\right)^2}. \tag{4.4}$$

We chose a Gaussian distribution centered around $\varphi_{C,2} = 0.5\,\pi$ with its width denoted by $\sigma_{\varphi,2}$ from hereon:

$$g(\varphi) \propto e^{-\frac{(\varphi-0.5\pi)^2}{2\sigma_{\varphi,2}^2}}. \tag{4.5}$$

The distribution in φ is shown in Fig. 4.11 for the different widths used in the lower left plot of Fig. 4.10. Apart from the lower left plot we always choose the width of the additional bump to be $\sigma_{\varphi,2}^2 = 0.2$ rad^2 in Fig. 4.10.

However the local line broadening acts as a convolution on $g(\varphi)$. Therefore however small we choose the region in φ, where gas clouds in addition to the symmetric distribution are located, the contribution to the overall flux extends over a larger range of velocities compared to the January 2006 peak. This effect is shown in the middle left plot of Fig. 4.10. For values of $\sigma_{v,2}/(v_{\rm rot,2}\ \sin\ i)$= 0.25 and 1 (dotted line and dashed line) the additional flux extends over a large velocity range. Only if $\sigma_{v,2}/(v_{\rm rot,2}\ \sin\ i)$ goes to zero we can reproduce the bump properly. Hence we have to change the local line broadening term for the clouds described in $g(\varphi)$:

$$\begin{aligned}\Phi_v^*(r,\varphi) = {} & \frac{f(r)}{r}e^{-\frac{(v_{\rm rot}\sin i)^2}{2\sigma_v^2}\left(\sin\varphi - \frac{v}{v_{\rm rot}\sin i}\right)^2} \\ & + \frac{f_2(r)}{r}g(\varphi)\delta\left(\sin\varphi - \frac{v}{v_{\rm rot,2}\sin i}\right).\end{aligned} \tag{4.6}$$

A summary of the parameter space of this equation is given in Table 4.3.

The local line broadening does not have to vanish altogether. In fact the width of the peak depends as well on the distribution of clouds in radial and azimuthal direction. But with the delta function we get an upper limit on the volume of the additional clouds in φ. With the same argument, we changed the distribution in r to a steeper distribution with $f_2(r) \propto r^2$ for $r < r_{\rm BLR}$ and $f_2(r) \propto r^{-2}$ for $r > r_{\rm BLR}$. The radial distribution of line emission is shown in Fig. 4.12 for f, f_2 and the sum of the two components at $\varphi_{C,2}$. The flux originating from this additional bump is responsible for about 5 % of the total BEL flux.

Even if we chose these clouds to be located at $\varphi_{C,2} = 0.5\,\pi$ where $v_{\rm rot}\ \sin\ i$ is directed exactly away from us (the unprojected velocity is proportional to $\sin\varphi$) we would not be able to reach velocities above 1500 km s^{-1}. However the peak can be best reproduced with a velocity of 2500 km s^{-1} as shown in middle right plot of

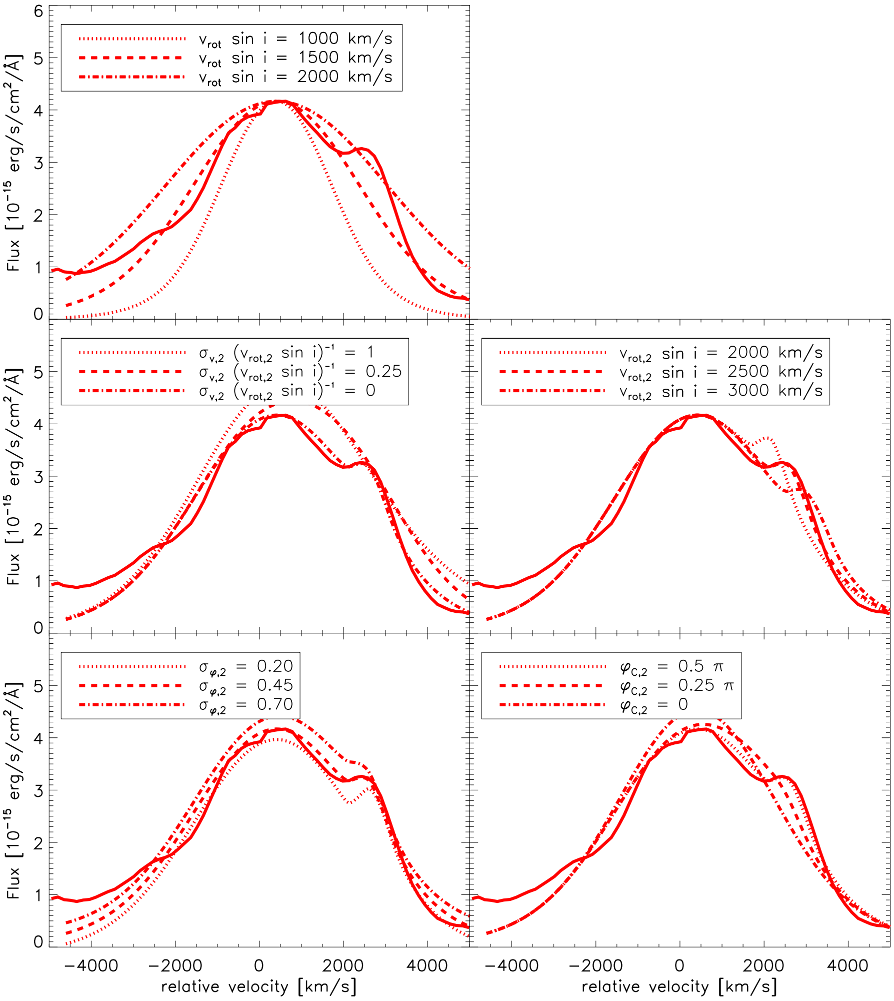

Figure 4.10 Influence of some of the parameter space of Eq. 4.6 on the shape of the BEL in comparison to the observed January 2006 Paβ line (solid lines). In all plots the BEL was modeled with the parameters which reproduce the Paβ line best. These are $v_{\text{rot}} = 1500$ km s^{-1}, $\sigma_{v,2}\ (v_{\text{rot}}\ \sin\ i)^{-1} = 0$, $v_{\text{rot},2} = 2500$ km s^{-1}, $\sigma^2_{\varphi,2} = 0.45$ rad and $\varphi_{C,2} = 0.5\ \pi$. The parameters varied are shown in the legends at the top of each plot. In the upper left plot the changes due to different rotational velocities are shown. The middle left plot illustrates how increasing the local line broadening leads to a wider bump. A visualization of the influence of a changing rotational velocity of the additional clouds is given in the right plot in the middle. In the lower left plot different widths of $g(\varphi)$ are shown. We note that the dotted line is shifted down and the dashed dotted line is shifted up by 0.2×10^{-15} erg/(s cm^2 Å) for better visibility. Finally in the lower left plot the center of the additional clouds ($\varphi_{C,2}$) is varied. These plots are not to be understood as fits to the data. Rather we want to explore how different parameters change the modeled BEL.

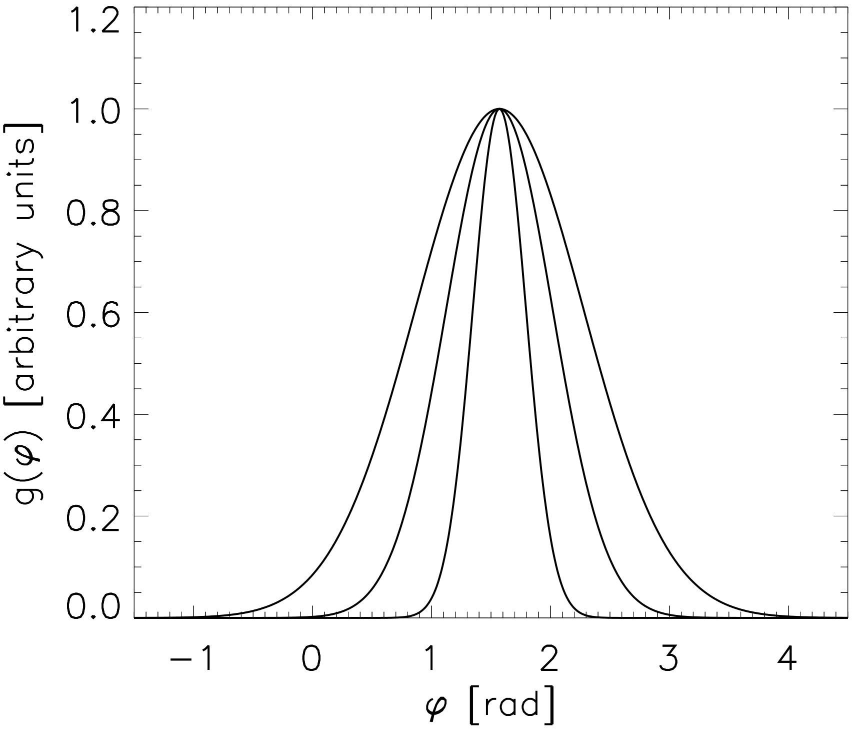

Figure 4.11 Distribution of additional clouds in the BLR introduced by $g(\varphi)$ in Eq. 4.4 and 4.6 in azimuthal direction. These additional clouds are needed to reproduce the bump in the January 2006 spectrum in Fig. 4.2 (red line). They are modeled as a Gaussian distribution with a width of $\sigma_{\varphi,2} = 0.20, 0.45$ and 0.70 rad and centered around $\varphi_{C,2} = 0.5\,\pi$.

Fig. 4.10. Therefore the additional clouds responsible for the bump emission need to be located closer to the black hole than $r_{\rm BLR}$ as a rotational velocity of at least $v_{\rm rot} \sin i = 2500$ km s^{-1} is needed to create a peak at this velocity. Therefore, a second velocity must be introduced in Eq. 4.6 ($v_{\rm rot,2}$) which is the velocity of the additional clouds added with $g(\varphi)$.

In the lower left plot of Fig. 4.10, we show how changes of the width of $g(\varphi)$ changes the appearance of our bump. Apart from the peak becoming slightly wider with increasing width it does not change too strongly. The reason for this is the non-existing local line broadening. As long as the local line broadening is turned off, a constant cloud distribution in azimuthal direction leads to a double peaked BEL. This means the distinct peak around $v_{\rm rot,2} \sin i$ will not show major changes to its width however big we choose $\sigma^2_{\varphi,2}$. Yet $\sigma_{\varphi,2} \approx 0.45$ rad gives us the best resulting peak and if the additional clouds would be extended throughout the AD there should be a second peak at the blue shifted wing of the BEL.

The results for a varying $\varphi_{C,2}$ is shown in the lower right plot. Moving the

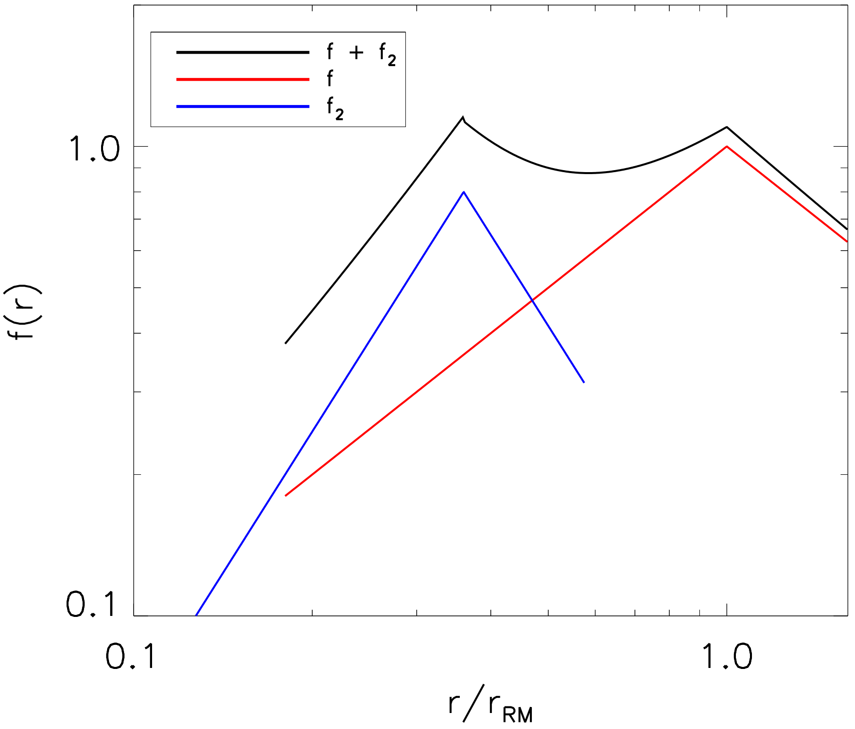

Figure 4.12 Radial distribution of line emission as used in Eq. 4.6 for f (red line), f_2 (blue line) and the sum of the two components at $\varphi = 0.5\,\pi$ (where we put the additional clouds in azimuthal direction). r_{rm} is the center of the overall BLR and the additional clouds are shifted inwards according to the ratio of v_{rot} and $v_{\mathrm{rot},2}$ squared. Together with the distribution in azimuthal direction (compare Fig. 4.11) the additional clouds are responsible for approximately 5 % of the total BEL flux.

center towards 0 has two effects: The resulting peak widens and the center of the peak moves towards lower velocities. But unless $\sigma_{\varphi,2}$ is not very small the velocity change of the peak is smaller than sin $\varphi_{C,2}$ would suggest due to the convolution with the local line broadening term. However if we choose $\sigma_{\varphi,2}$ too small it can be hard to explain how to produce 5 % of the BEL flux in such a small space on timescales of at most two years. For $\varphi_{C,2} < 0$ the same peaks appear on the blue wing of the BEL.

There are three effects which could lead to the subsequent flattening of the peak in June 2006 and January 2007: The clouds rotating away from $\varphi_{C,2} = 0.5\,\pi$ (which would take longer than one year at these rotational velocities), turning on the local line broadening again (the clouds of $g(\varphi)$ no longer move with a common velocity) and additional similar events at lower projected velocities or a combination of these two effects. A further extend of the clouds in azimuthal direction can not explain this broadening alone as the small local line broadening always leads to a peak around $v_{\mathrm{rot},2}\ \sin\ i$ (compare the lower right plot of Fig. 4.10). The enhanced flux in January 2007 extends to around the center of the BEL. As we can see in the upper right plot of Fig. 4.10 this can be realized with $\sigma^2_{\varphi,2} = 0.2\ \mathrm{rad}^2$ and local line broadening term of $\sigma_{v,2}\ (v_{\mathrm{rot}}\ \sin\ i)^{-1} = 0.25$.

4.5 Discussion

In this section, we explore if the so far purely phenomenological description of BEL profile variability in NGC 4151 matches our understanding of physical processes occurring in that very central region around the SMBH.

4.5.1 Dust production

In Fig. 4.7, we show the dust radii of NGC 4151 (red stars) determined by Koshida et al. (2009) along with the increasing relative flux in the red wing of the BELs. This parallel change of BEL shape and dust radius in NGC 4151 raises the question whether this is coincidental or is caused by a connection between the BLR and the dust torus and what this can tell us about dust occurrence and creation in AGN. An important property for the dust creation is the temperature of the dust torus. Only below a certain temperature dust can be created. This limiting temperature is usually assumed to be around 1000 K (e.g., Czerny & Hryniewicz 2011) as this temperature was found for dust production in outflows of evolved stars where similar conditions are present as in BLR clouds (Groenewegen et al. 2009). Unfortunately Koshida et al. (2009) could not measure the temperature directly as they only had single band infrared fluxes in the K band. However applying Eq. 1.15 from Section 1.6 the dust temperature can be connected to the dust radius ($R_{\mathrm{sub,theo}}$), the UV luminosity (L_{UV}), the sublimation temperature (T_{sub}) and the grain size of the dust (a):

$$R_{\mathrm{sub,theo}} = 1.3\sqrt{\frac{L_{\mathrm{UV}}}{10^{46}\mathrm{erg/s}}}\left(\frac{T_{\mathrm{sub}}}{1500\mathrm{K}}\right)^{-2.8}\left(\frac{a}{0.05\mu\mathrm{m}}\right)^{-0.5}\ \mathrm{pc}. \tag{4.7}$$

Assuming a constant dust grain size and sublimation temperature for NGC 4151 we can calculate mean dust temperatures at different radii if we assume certain temperatures in one of the periods from Koshida et al. (2009). Our chosen period is the third one, as its luminosity is the highest while the dust radius is comparable to the first period where the luminosity is much lower. Therefore we can assume that the dust temperature should not be very low in the third period. We want to see which temperature a dust cloud at the smallest dust radius found by Koshida et al. (2009) (33 ld) would have during all periods:

$$T_{33\mathrm{ld}} = T_3\left(\frac{R_{\mathrm{sub,theo,3}}}{33\ \mathrm{ld}}\right)^{1/2.8}\left(\frac{L_i}{L_3}\right)^{1/5.6}. \tag{4.8}$$

In this equation T_3 is the assumed mean temperature in the third period, $R_{\mathrm{sub,theo,3}}$ is the sublimation radius during the third period and L_i is the mean

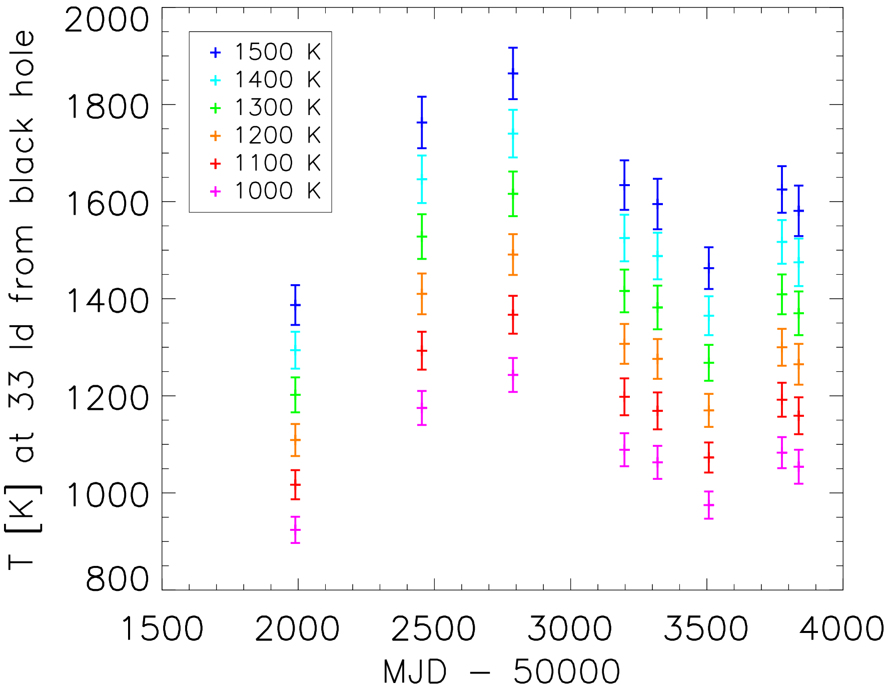

Figure 4.13 Different dust temperatures for NGC 4151 at a distance of 33 ld from the black hole assuming mean temperatures between 1000 and 1500 K during the third epoch of the NGC 4151 dust reverberation campaign from Koshida et al. (2009). The temperatures were calculated using Eq. 4.8 with the assumption of a constant dust grain size. The color coding for the assumed mean temperatures during the third reverberation period is shown in the upper left corner of the plot. This shows that it is very hard to reach temperatures below 1000 K at a distance of 33 ld from the black hole, which are needed for dust production above the AD.

luminosity in different epochs. With Eq. 4.8 we get the temperature at different times at a distance of 33 ld to the black hole.

The result of this line of thought is shown in Fig. 4.13 for T_3 between 1000 and 1500 K. During the second period Landt et al. (2015) measured a dust temperature of 1316 K. During the third epoch the luminosity is higher while the dust radius stays almost the same. Therefore dust temperatures should be higher than 1300 K. Additionally the temperatures measured by Schnülle et al. (2015) and Landt et al. (2015) for NGC 4151 never drop below 1200 K. Baskin & Laor (2018) show that depending on especially gas density, grain size, and dust type T_{sub} can reach temperatures as high as 2000 K. Therefore the temperature T_3 can be assumed to be at least higher than 1300 K.

This means it is very hard to create dust above the AD at the radii where dust reverberation finds it. In Fig. 4.13 it can be seen that a temperature below 1000 K can only be reached if T_3 is as low as ~ 1000 K and only in the sixth period (apart from the first period). Otherwise the temperatures are well above this threshold for dust production at a distance of 33 ld from the black hole. If T_3 is indeed higher than 1300 K the mean temperatures at this distance to the black hole can not be much smaller than 1200 K. Therefore it is only possible to form the dust above the AD if dust formation can happen on very short timescales when the temperature is (significantly) below the mean temperature. If the dust were to be produced by stars outside the AGN as proposed by Schartmann et al. (2010) in NGC 1068 the decrease of the dust radius of ~ 30 ld in ~ 600 days would suggest a velocity of the dusty gas clouds towards the black hole of approximately 5 % of the speed of light. This seems to be too high for an inflow as only ultra fast outflows from AGN have been observed in this velocity range. Velocities in a range up to 30 % the speed of light peaking around 0.1 % the speed of light were reported for these outflows (e.g., Chartas et al. 2003; Tombesi et al. 2010).

A solution to this problem (finding dust where it is too hot to form it) is provided by the model of the outer BLR formation from Czerny & Hryniewicz (2011). The dust is formed inside the AD where the radiation from the inner AD is blocked by the AD and therefore temperatures can be lower than above the AD where the clouds are directly exposed to the AD. The dusty clouds are than pushed above the AD where the clouds are directly exposed to the radiation from the inner AD and subsequently destroyed by the radiation if the clouds are heated above the sublimation temperature. If the dust is indeed destroyed the gas clouds can become visible as part of the BEL.

This relates to the changes of the dust radius and the shape of the BEL as follows. Dust clouds are produced within a range of radii in the the AD smaller than the previously smallest dust radius (sublimation radius) above the AD due to the additional radiation shielding inside the disk. Of these emerged dusty clouds the innermost clouds will loose their dust due to sublimation quickly and appear as addition to the BLR, while the dusty clouds will survive longer at small radii. If the amount of dust clouds is high enough, or the AD luminosity drops at the same time these dusty clouds will lead to a reduced time lag of the dust reverberation radius as seen by Koshida et al. (2009). Thus the same cloud formation process in a radiation driven wind can add both to the BLR gas clouds, and the dusty clouds contributing to the torus.

4.5.2 Kinematic features and possible origin of additional clouds

The results from our BEL modeling (compare with Section 4.4) support the view discussed above. The radius at which the shape of the BEL changes has to be at least two times smaller than r_{BLR} of the overall BEL because of the velocities of the overall BEL and the additional peak. This is comparable to the changes in dust radius found by Koshida et al. (2009). The enhanced flux can only be seen around 2100 km s^{-1} in the BELs while the overall shape of the BELs does not change much with rotational velocities of around v_{rot} sin i = 1500 km s^{-1}. An explanation for this is that the BEL changes only in a confined area in azimuthal direction of the AD and the overall distribution changes take much longer. It could be possible to explain the enhanced BEL gas density by an inflow of gas clouds, but in this case the changes in the shape on timescales of half a year from January 2006 to June 2006 and January 2007 are hard to explain.

The overall distribution of BEL clouds would not be symmetrical under these assumptions. In Fig. 4.10 we showed that a broader distribution of additional clouds still leads to a distinct peak as long as the local line broadening term is negligible. Therefore it is hard to pinpoint how broad the distribution of additional clouds is as the width in flux of the additional peak is not very sensitive to this distribution. Nonetheless a width of $\sigma_{\varphi,2} \approx 0.45$ rad can best reproduce the peak found in the January 2006 BEL and if we increase the local line broadening term again we can reproduce a wider additional flux without changing $\sigma_{\varphi,2}$ as seen in the January 2007 Paβ BEL. In 2010 the bump vanished completely which can be caused by a combination of two effects: a further increase of the local line broadening term and a dispersion of clouds in azimuthal direction due to interactions with other BLR clouds. While there is no chance to get this azimuthal information of the distribution of dust clouds Schnülle et al. (2015) found indications of a radial extend of the inner edge of the dust torus as well in NGC 4151 (although not at the same time). It could be interesting to see whether simulations can reproduce the changes in dust radius even if the 'new' dust has only a similarly small extend in azimuthal direction.

We can also infer an absolute value of r_{BLR} for the two velocities we got from our modeling using the black hole mass determined by Grier et al. (2013a) of $M_{\mathrm{BH}} = 3.62^{+0.39}_{-0.22} \times 10^{7}$ $\mathrm{M}_{\odot}$. This leads to $r_{BLR,2} = 30^{+3}_{-2}$ ld $\sin^2$ i for $v_{\mathrm{rot},2}$ sin i = 2500 km s^{-1} and $r_{\mathrm{BLR}} = 83^{+9}_{-6}$ ld $\sin^2$ i for v_{rot} sin i = 1500 km s^{-1}. In the literature the inclination is given as 45° with an error around 10° (e.g., Das et al. 2005;

Müller-Sánchez et al. 2011) and thus $\sin^2 i$ leads to a factor of 0.5 and hence radii of the BLR around 15 and 40 ld. These radii lie well within the range in which Shapovalova et al. (2008) found emitting gas (1 to 50 ld) between 1996 and 2006.

According to Baskin & Laor (2018) the outer radius of the BLR is located at 1.6 r_{BLR}. This leads to an outer radius of the BLR or inner dust radii of 66 ± 15 ld and 24 ± 5 ld. Both of these values are slightly lower than the largest and smallest dust radius found by Koshida et al. (2009) (71 and 33 ld). However, Schnülle et al. (2013) showed that the determined dust radius depends on the infrared wavelength used for the dust reverberation mapping. As Koshida et al. (2009) used the K band they will not have picked up this innermost dust radius. Therefore our determined r_{BLR} is not in contradiction with their dust radius. The flux present in the peak is responsible for about 5 % of the total BEL flux and the area in which this flux is produced (with a width of $\sigma_{\varphi,2} \approx 0.45$ rad and at a smaller radius) is also in the range of 5 % the area in which the overall BEL was produced. This shows that the area should be large enough to produce the additional flux.

With this radius we can also determine a temperature inside the AD following the line of argument of Czerny & Hryniewicz (2011) using the monochromatic luminosity at 5100 Å. We can take this luminosity from Shapovalova et al. (2008) and get a disk temperature of around 450 K at r_{in}. However looking at the optical lightcurve in both Shapovalova et al. (2008) and Koshida et al. (2009) of NGC 4151, the optical flux was significantly higher in December 2005 (with no data until June 2005). As the clouds are produced before becoming visible as part of the BEL we can get to temperatures of approximately 600 K easily considering an increased monochromatic luminosity (or potentially even higher if the optical flux would have been even higher between June and December 2005). This temperature is consistent with the dispersion of temperatures found by Czerny & Hryniewicz (2011), who published a similar temperature of 550 K for NGC 4151. To summarize, while at the centro-nuclear radii, where we locate the clouds responsible for the BLR shape variation, the temperatures above the AD appear too high for in-situ dust formation, they drop to values allowing to form dust inside the AD of NGC 4151 at the same radii.

4.6 Summary and conclusions

We connected BEL shape variability to the decrease of the dust radius in NGC 4151 between May 2004 and January 2006 in this chapter. The results we obtain are:

The simultaneous decrease of the dust radius and BEL shape variability point to a connection between the BLR and the dust torus. Additionally the velocity, at which the shape variability occurs, indicates a similar decrease of dust radius and BLR radius.

The dust needed for the reduced dust radius is presumably produced in the AD as the temperatures above the AD hardly reach temperatures low enough for dust production. Inflows are also unlikely as a reason for the change of dust radius due to the short timescales of the changes of dust radius. This leaves us with dust production in the AD described in dust inflated AD models. The indications for a similar decrease in radius of both the clouds of the dust torus and BLR provide evidence that the dust and BLR clouds share a similar origin.

The correlated changes in the BEL discussed occur in only a small range of velocities (visible as transient bump). This indicates missing broadening via velocity dispersion of the fresh clouds which can be naturally explained by the here favored formation scenario in an AD wind. We cannot significantly constrain the azimuthal extension of the cloud formation zone but can rule out a completely symmetrical distribution all around the nucleus. If the dust torus and BLR are indeed similar in their production mechanism it is possible that the dust torus shows a similar distribution of clouds. The location of peaks in BELs can give us information of the radial position of the BLR. In particular if the peak is well defined and sharp the probability is high that the additional clouds are located close to $\varphi = \pm 0.5\,\pi$. For azimuthal angles with lower projected velocities the peak would be broadened and a much smaller extend in azimuthal direction of the additional clouds would be needed. This explains why similar cloud formation events are less observable if occurring at different azimuthal angles.

As this is only one occasion where we were able to observe the described scenario, we cannot (and do not want to) rule out other dust production outside of the AD in other objects, at other times or at higher radii than those investigated here. For the same reason we cannot speculate what might cause the changes in dust production or if these are just statistical variations. In contrast, our analysis of combined datasets shows evidence supporting dust production in the AD and a similar production mechanism of the dust torus and BLR.

CHAPTER 5

Summary and Outlook

In this chapter we briefly summarize the results (Section 5.1) and give some ideas for future projects (Section 5.2), which are most promising to improve our understanding of the inner structure of AGN, based on our results.

5.1 Summary

In this thesis, the structure of the dust torus and BLR of AGN were investigated. This included a multiwavelength dust reverberation mapping campaign in Chapter 3 and the analysis of shape variations of BELs in Chapter 4. The main results of these two projects are:

- Our multiwavelength approach to reverberation mapping of the dust torus enabled the simultaneous determination of dust radius and temperature. We found a wide range of dust temperatures, indicating that the dust is not always located at its sublimation radius. The dust temperatures often exceeds the nominal sublimation temperature of silicate grains ($\approx$ 1400 K) in most of the AGN in our sample. Thus the dust composition of the inner parts of the dust torus should be dominated by graphite grains.
- Furthermore, we were able to introduce a new temperature normalization of the radius luminosity relation. This normalization reduces the scatter of the relation significantly and brings its slope into agreement with theoretical predictions. These improvements of the radius luminosity relation are especially important for the use as a cosmological standard candle. Only a good understanding of the radius luminosity relation of nearby AGN, allows the expansion to higher redshifts.
- With the dust temperatures we can also infer the surface area of the dust. The wide scatter of the surface area implies a wide range of dust torus morphologies. For most AGN in our sample, we find the surface area to be proportional to the dust radius squared. However some of the AGN have significantly smaller surface areas of dust or the dust is not detectable by our means.
- Both projects provide evidence of similarities between the dust torus and the rotation dominated, low-ionization part of the BLR. Mrk 590 has a very small surface area of dust and only very weak BELs, indicative of a very low amount of clouds in both regions. The shape variations of the BELs of NGC 4151 take place at the same time as a significant decrease of the radius

of the dust torus. Apart from the simultaneity of the two events, we find, that the newly formed BLR clouds have to be created at a smaller radius than the main part of the BLR. Furthermore, the change of radius of the dust torus and BLR are similar.

- Additionally, the creation of the newly formed clouds has to take place in a very confined area in azimuthal direction. This shows that the BLR is not continuously filled and can be rather patchy. The large scatter of surface areas of dust, suggest that this patchiness is also found in the dust torus and can vary strongly between sources. These differences in appearance have to be taken into account for the determination of BH masses, as the geometry of the BLR has an influence on the f-factor used for BH mass determinations.
- The creation of dust clouds above the AD is disfavored by our approximation of the temperature at the smallest dust radii found for NGC 4151. Temperatures below 1000 K, required for dust formation in this environment, can not be reached well above the AD. This is also the case for the dust temperatures determined in our reverberation mapping project. Only very few sources have dust temperatures sufficiently low for this channel of dust production. Therefore our findings support failed radiatively accelerated outflow models as the source of torus and BLR cloud production. In these models dust is produced within the AD and lifted above the AD by radiation pressure. Depending on the radius of the clouds, the dust either sublimates and the clouds become a part of the BLR or the clouds become part of the dusty torus.

5.2 Outlook

The results presented in this thesis, improve our understanding of the inner structure of AGN. Essentially there are two paths possible for future projects: A continuation of reverberation mapping projects, while improving the methodology and using interferometry, with the potential to image the inner structure more directly.

5.2.1 Improvements to reverberation mapping campaigns

The main source of systematic uncertainties in our reverberation mapping project (Chapter 3) was the determination of the host reddening parameter. A possible overestimation of the optical luminosity cannot be ruled out for the sources showing signs of host reddening. It is possible that the remaining scatter in the radius luminosity relation is partly caused by this overestimation. At least one parallel spectroscopic observations enables us to measure the host reddening independently using absorption line properties.

For a better understanding of the connection between the dust torus and the BLR concurrent reverberation mapping projects of both structures are desirable. Landt et al. (2019) were able to determine a dust time lag with NIR spectroscopy extending to 0.7 μm using the SpeX spectrograph at IRTF. Thus simultaneous additional optical spectroscopy can be omitted. However extremely-wide-band spectrographs, delivering optical-near-infrared in one shot (like the Very Large Telescope (VLT) x-Shooter), are better suited for these studies, as the optical emission gives better estimates of the AD luminosity.

A byproduct of these studies would be a better time sampling of BEL shape variations, as described in Chapter 4. In our case the radial location of the additional clouds had to be inferred from their velocity. Increasing the cadence of observations enables the determination of that radius using velocity resolved reverberation mapping. Furthermore it would have been possible to directly compare torus and BLR radii and show whether these two are correlated.

In order to better understand physical processes involved in the dusty torus and BLR changes of radii in reverberation mapping can be invaluable. It is important to know in which conditions dust is formed or sublimates. It is desirable to get to know when "new" dust forms and how. It is completely unclear whether the formation of clouds forming the torus and BLR is a constantly ongoing process or happens in concrete events on relatively short timescales. From sublimation events conclusions can be drawn on the sublimation temperature and thus also on the grain sizes of the dust, as shown by Schnülle (2017). In the sample presented in this thesis only few AGN were observed on timescales long enough and with a sufficient cadence of observations to infer changes of dust radius. In most cases only the determination of a single radius was possible. If there were enough observations on a source ($\gtrsim 8$) only two sources showed indications of a changing dust radius, indicating how rare these events seem to be. In summary reverberation mapping projects have to be conducted on longer timescales and with higher cadence when aiming at understanding formation and destruction mechanisms of dust.

5.2.2 Direct imaging of BLR and dust torus with interferometry

The angular resolution of the NIR interferometers with the largest baselines (e.g. the VLTI with (2 mas) is not sufficient to directly resolve typical angular sizes of dust tori or BLRs (< 1 mas). Still it is possible to infer information about the structure from either fitting models to the partially resolved signal or the photocenter offsets at different wavelength. Centroiding a PSF to the signal at different wavelength can give spatial information beyond the angular resolution (by a factor of 10 to 100, depending on the S/N). This way, velocity dependent photocenters can be determined for the BELs and BLR radii can be constrained. This was demonstrated by Gravity Collaboration et al. (2018) with a resolution of 0.01 mas for the BLR of 3C273. 3C273 is the brightest quasar on the sky, thus the achieved resolution should be the highest possible for VLTI. Unfortunately, due to technical limitations, it is not yet possible to use interfermoters in the optical. Thus the determination of the photocenter of the AD and thus a very good estimate of the location of the SMBH is not possible. Still it is possible to study the structure of the torus and BLR and a few of these possibilities to accompany reverberation mapping studies will be outlined here.

A major issue of reverberation mapping campaigns is finding delays for high luminosity AGN (above $\approx 10^{38}$ W). The campaigns have to last longer than the delay to have a chance of measuring this delay. Therefore the radius luminosity relation is not well constrained at high luminosities, as only very few delays are determined in this luminosity range. Both the high luminosity and the large radii are advantages for interferometric observations and should simplify (partially) resolving the inner structure. However, AGN with such high luminosity are rare, especially in the local universe. Yet, adding these to the radius luminosity relation is invaluable to understand the AGN at higher redshift, where only the sources with high luminosity can be observed. As we showed in this thesis the temperature normalization of the radius luminosity relation is essential. Therefore the interferometric observations of dust tori should be accompanied by spectroscopic observations to determine the temperature of the innermost dust.

The direct observation of the azimuthal structure of the dust torus or BLR with interferometry is difficult due to the resolution limit of existing interferometers. But it is possible to measure the velocity-resolved photocenter shift in the NIR emission lines with adequate sub-mas resolution. Furthermore, in AGN with low dust content, the NIR continuum photocenter is dominated by the AD, and can be compared to the BLR photocenter. Such differential photocenter shifts between BLR and continuum can indicate inhomogeneous cloud distributions varying with azimuthal angle. Therefore, a time-resolved interferometric study of the BLR photocenter can further constrain the morphological stability of the BLR, and detect variations in the cloud content.

In a nutshell simultaneous dust and BLR reverberation mapping campaigns combined with interferometric observations have the largest potential to significantly improve our understanding of the inner structure of AGN. While reverberation mapping enables us to determine average inner radii of the dust and BLR very well, interferometry offers the opportunity to learn more about the azimuthal and radial cloud distribution. Additionally the torus BLR connection is only poorly understood, as the two components are usually studied individually. For example it is unclear whether low dust and BLR emission systematically correlate. This would give further evidence of common physical conditions and cloud production mechanisms in the torus and BLR.

Glossary

2MASS Two Micros All Sky Survey

AD accretion disk

AGB asymptotic giant branch

AGN Active Galactic Nucleus

BEL broad emission line

BH black hole

BLR broad line region

CF covering factor

ELT Extremely Large Telescope

EW Equivalent Width

FWHM Full Width Half Maximum

GROND Gamma-Ray Optical and Near-Infrared Detector

IDL Interactive Data Language

IR infra-red

IRTF InfraRed Telescope Facility

mas milliarcsecond

MCMC Markov Chain Monte Carlo

MIR mid infra-red

NEL narrow emission line

NIR near infra-red

NLR narrow line region

PSF point spread function

QSO quasi-stellar object

RLQ radio-loud quasar

RQQ radio-quiet quasar

S/N signal-to-noise ratio

SDSS Sloan Digital Sky Survey

SED spectral energy distribution

SMBH supermassive black hole

SXD short cross-dispersed

UV ultraviolet

VLT Very Large Telescope

VLTI Very Large Telescope Interferometer

Publications of J. Esser

Parts of the work presented in this thesis have previously appeared in the following articles:

- **J. Esser**, J.-U. Pott, H. Landt, W. D. Vacca (2019), *Analyzing temporal variations of AGN emission line profiles in the context of (dusty) cloud structure formation in the broad line region*, Astronomy & Astrophysics, 621, A46
- **J. Esser**, J.-U. Pott, K. Schnülle, H.-W. Rix,, H. Landt, F. Bosco, F. Pozo Nuñez J. Greiner, R. Lachaume (subm.), *Multiwavelength dust reverberation mapping of nearby Active Galactic Nuclei*, Astronomy & Astrophysics

Other publications including J. Esser (as first author or co-author):

- H. Landt, M. J. Ward, D. Kynoch, C. Packham, G. J. Ferland, A. Lawrence, J.-U. Pott, **J. Esser**, K. Horne, D. A. Starkey, D. Malhotra, M. M. Fausnaugh, B. M. Peterson, R. J. Wilman, R. A. Riffel, T. Storchi-Bergmann, A. J. Barth, C. Villforth, H. Winkler, *The first spectroscopic dust reverberation programme on active galactic nuclei: the torus in NGC 5548*, Monthly Notices of the Royal Astronomic Society, 489, 1572-1589
- F. Pozo Nuñez, N. Gianniotis, J. Blex, T. Lisow, R. Chini, K. L. Polsterer, J.-U. Pott, **J. Esser**, G. Pietrzyński (2019), *Optical continuum photometric reverberation mapping of the Seyfert-1 galaxy Mrk509*, Monthly Notices of the Royal Astronomic Society, 490, 3936-3951
- S. D. Kügler, K. Nilsson, J. Heidt, **J. Esser**, T. Schultz (2014), *Properties of optically selected BL Lacertae candidates from the SDSS*, Astronomy & Astrophysics, 569, A95
- S. D. Kügler, K. Nilsson, J. Heidt, **J. Esser**, T. Schultz (2014), *VizieR Online Data Catalog: SDSS optically selected BL Lac candidates (Kuegler+, 2014)*, VizieR Online Data Catalog: SDSS optically selected BL Lac candidates (Kuegler+, 2014)

Bibliography

Abramowicz, M. A., Calvani, M., & Nobili, L. 1980, ApJ, 242, 772

Abramowicz, M. A., Chen, X. M., Granath, M., & Lasota, J. P. 1996, ApJ, 471, 762

Alam, S., Albareti, F. D., Allende Prieto, C., et al. 2015, ApJS, 219, 12

Antonucci, R. 1993, ARA&A, 31, 473

Antonucci, R. R. J. 1984, ApJ, 278, 499

Antonucci, R. R. J., & Miller, J. S. 1985, ApJ, 297, 621

Asmus, D., Hönig, S. F., & Gandhi, P. 2016, ApJ, 822, 109

Bardeen, J. M., Press, W. H., & Teukolsky, S. A. 1972, ApJ, 178, 347

Barvainis, R. 1987, ApJ, 320, 537

Baskin, A., & Laor, A. 2018, MNRAS, 474, 1970

Baskin, A., Laor, A., & Stern, J. 2014, MNRAS, 438, 604

Bentz, M. C., Walsh, J. L., Barth, A. J., et al. 2008, ApJL, 689, L21

Bentz, M. C., Denney, K. D., Grier, C. J., et al. 2013, ApJ, 767, 149

Bianchi, S., Corral, A., Panessa, F., et al. 2008, MNRAS, 385, 195

Blandford, R., Netzer, H., Woltjer, L., Courvoisier, T. J.-L., & Mayor, M. 1990, Active Galactic Nuclei, 97

Bolton, J. G., Stanley, G. J., & Slee, O. B. 1949, Nature, 164, 101

Bon, E., Popović, L. Č., Gavrilović, N., La Mura, G., & Mediavilla, E. 2009, MNRAS, 400, 924

Burtscher, L., Jaffe, W., Raban, D., et al. 2009, ApJL, 705, L53

Cameron, M., Storey, J. W. V., Rotaciuc, V., et al. 1993, ApJ, 419, 136

Chartas, G., Brandt, W. N., & Gallagher, S. C. 2003, ApJ, 595, 85

Chartas, G., Rhea, C., Kochanek, C., et al. 2016, Astronomische Nachrichten, 337, 356

Clavel, J., Reichert, G. A., Alloin, D., et al. 1991, ApJ, 366, 64

Cohen, R. D., Rudy, R. J., Puetter, R. C., Ake, T. B., & Foltz, C. B. 1986, ApJ, 311, 135

Collier, S. J., Horne, K., Kaspi, S., et al. 1998, ApJ, 500, 162

Cushing, M. C., Vacca, W. D., & Rayner, J. T. 2004, PASP, 116, 362

Czerny, B., & Hryniewicz, K. 2011, A&A, 525, L8

Czerny, B., Hryniewicz, K., Maity, I., et al. 2013, A&A, 556, A97

Czerny, B., Li, Y.-R., Hryniewicz, K., et al. 2017, ApJ, 846, 154

Das, V., Crenshaw, D. M., Hutchings, J. B., et al. 2005, AJ, 130, 945

Davies, R. I., Müller Sánchez, F., Genzel, R., et al. 2007, ApJ, 671, 1388

Denney, K. D., Peterson, B. M., Pogge, R. W., et al. 2009, ApJL, 704, L80

Denney, K. D., De Rosa, G., Croxall, K., et al. 2014, ApJ, 796, 134

Dietrich, M., Kollatschny, W., Peterson, B. M., et al. 1993, ApJ, 408, 416

Du, P., Hu, C., Lu, K.-X., et al. 2015, ApJ, 806, 22

Du, P., Lu, K.-X., Hu, C., et al. 2016, ApJ, 820, 27

Edelson, R., Gelbord, J. M., Horne, K., et al. 2015, ApJ, 806, 129

Eracleous, M., & Halpern, J. P. 2003, ApJ, 599, 886

Esser, J., Pott, J. U., Landt, H., & Vacca, W. D. 2019, A&A, 621, A46

Esser, J., Pott, J. U., Schnülle, K., et al. subm., A&A

Evans, D. W., Riello, M., De Angeli, F., et al. 2018, A&A, 616, A4

Event Horizon Telescope Collaboration, Akiyama, K., Alberdi, A., et al. 2019, ApJL, 875, L1

Fath, E. A. 1909, Lick Observatory Bulletin, 149, 71

Fausnaugh, M. M., Denney, K. D., Barth, A. J., et al. 2016, ApJ, 821, 56

Gaia Collaboration, Prusti, T., de Bruijne, J. H. J., et al. 2016, A&A, 595, A1

Gaia Collaboration, Brown, A. G. A., Vallenari, A., et al. 2018, A&A, 616, A1

Gravity Collaboration, Sturm, E., Dexter, J., et al. 2018, Nature, 563, 657

GRAVITY Collaboration, Dexter, J., Shangguan, J., et al. 2019, arXiv e-prints, arXiv:1910.00593

Gravity Collaboration, Pfuhl, O., Davies, R., et al. 2020, A&A, 634, A1

Greiner, J., Bornemann, W., Clemens, C., et al. 2008, PASP, 120, 405

Grier, C. J., Martini, P., Watson, L. C., et al. 2013a, ApJ, 773, 90

Grier, C. J., Peterson, B. M., Horne, K., et al. 2013b, ApJ, 764, 47

Groenewegen, M. A. T., Sloan, G. C., Soszyński, I., & Petersen, E. A. 2009, A&A, 506, 1277

Guhathakurta, P., & Draine, B. T. 1989, ApJ, 345, 230

Hao, H., Elvis, M., Civano, F., & Lawrence, A. 2011, ApJ, 733, 108

Hao, H., Elvis, M., Civano, F., et al. 2010, ApJL, 724, L59

Hogg, D. W. 1999, arXiv e-prints, astro

Hönig, S. F., & Kishimoto, M. 2010a, A&A, 523, A27

Hönig, S. F., & Kishimoto, M. 2010b, A&A, 523, A27

Hönig, S. F., & Kishimoto, M. 2011, A&A, 534, A121

Hönig, S. F., Kishimoto, M., Antonucci, R., et al. 2012, ApJ, 755, 149

Hönig, S. F., Kishimoto, M., Tristram, K. R. W., et al. 2013, ApJ, 771, 87

Hönig, S. F., Watson, D., Kishimoto, M., et al. 2017, MNRAS, 464, 1693

Hutsemékers, D., Agís González, B., Marin, F., et al. 2019, A&A, 625, A54

Ilić, D., Popović, L. Č., Bon, E., Mediavilla, E. G., & Chavushyan, V. H. 2006, MNRAS, 371, 1610

Ilić, D., Popović, L. Č., Shapovalova, A. I., et al. 2015, Journal of Astrophysics and Astronomy, 36, 433

Jaffe, W., Meisenheimer, K., Röttgering, H. J. A., et al. 2004, Nature, 429, 47

Jiang, L., Fan, X., Brandt, W. N., et al. 2010, Nature, 464, 380

Jones, D. O., Rodney, S. A., Riess, A. G., et al. 2013, ApJ, 768, 166

Jun, H. D., & Im, M. 2013, ApJ, 779, 104

Kawaguchi, T., & Mori, M. 2010, ApJL, 724, L183

Kawaguchi, T., & Mori, M. 2011, ApJ, 737, 105

Kawakatu, N., & Ohsuga, K. 2011, MNRAS, 417, 2562

King, A. L., Davis, T. M., Denney, K. D., Vestergaard, M., & Watson, D. 2014, MNRAS, 441, 3454

Kishimoto, M., Hönig, S. F., Antonucci, R., et al. 2011, A&A, 527, A121

Kishimoto, M., Hönig, S. F., Antonucci, R., et al. 2009, A&A, 507, L57

Kishimoto, M., Hönig, S. F., Beckert, T., & Weigelt, G. 2007, A&A, 476, 713

Koratkar, A. P., & Gaskell, C. M. 1989, ApJ, 345, 637

Koratkar, A. P., & Gaskell, C. M. 1991, ApJS, 75, 719

Korista, K., Baldwin, J., Ferland, G., & Verner, D. 1997, ApJS, 108, 401

Koshida, S., Yoshii, Y., Kobayashi, Y., et al. 2009, ApJL, 700, L109

Koshida, S., Minezaki, T., Yoshii, Y., et al. 2014, ApJ, 788, 159

Koski, A. T. 1978, ApJ, 223, 56

Krolik, J. H., & Begelman, M. C. 1988, ApJ, 329, 702

LaMassa, S. M., Cales, S., Moran, E. C., et al. 2015, ApJ, 800, 144

Landt, H., Bentz, M. C., Peterson, B. M., et al. 2011a, MNRAS, 413, L106

Landt, H., Bentz, M. C., Ward, M. J., et al. 2008, ApJS, 174, 282

Landt, H., Elvis, M., Ward, M. J., et al. 2011b, MNRAS, 414, 218

Landt, H., Ward, M. J., Elvis, M., & Karovska, M. 2014, MNRAS, 439, 1051

Landt, H., Ward, M. J., Steenbrugge, K. C., & Ferland, G. J. 2015, MNRAS, 449, 3795

Landt, H., Ward, M. J., Kynoch, D., et al. 2019, MNRAS, 489, 1572

Laor, A., & Draine, B. T. 1993, ApJ, 402, 441

Laor, A., & Netzer, H. 1989, MNRAS, 238, 897

Lira, P., Botti, I., Kaspi, S., & Netzer, H. 2018, ArXiv e-prints, arXiv:1801.03866

Lira, P., Videla, L., Wu, Y., et al. 2013, ApJ, 764, 159

López-Gonzaga, N., Jaffe, W., Burtscher, L., Tristram, K. R. W., & Meisenheimer, K. 2014, A&A, 565, A71

Lynden-Bell, D. 1969, Nature, 223, 690

Lyu, J., Rieke, G. H., & Shi, Y. 2017, ApJ, 835, 257

Maiolino, R., Salvati, M., Marconi, A., & Antonucci, R. R. J. 2001, A&A, 375, 25

Maoz, D., Netzer, H., Peterson, B. M., et al. 1993, ApJ, 404, 576

Markwardt, C. B. 2009, Astronomical Society of the Pacific Conference Series, Vol. 411, Non-linear Least-squares Fitting in IDL with MPFIT, ed. D. A. Bohlender, D. Durand, & P. Dowler, 251

Martínez-Sansigre, A., Rawlings, S., Garn, T., et al. 2006a, MNRAS, 373, L80

Martínez-Sansigre, A., Rawlings, S., Lacy, M., et al. 2006b, MNRAS, 370, 1479

McElroy, R. E., Husemann, B., Croom, S. M., et al. 2016, A&A, 593, L8

Michelson, A. A. 1891, Nature, 45, 160

Michelson, A. A., & Pease, F. G. 1921, ApJ, 53, 249

Minezaki, T., Yoshii, Y., Kobayashi, Y., et al. 2019, ApJ, 886, 150

Monnier, J. D. 2003, Reports on Progress in Physics, 66, 789

Mor, R., & Netzer, H. 2012, MNRAS, 420, 526

Mor, R., & Trakhtenbrot, B. 2011, ApJL, 737, L36

Morgan, C. W., Kochanek, C. S., Morgan, N. D., & Falco, E. E. 2010, ApJ, 712, 1129

Morganson, E., De Rosa, G., Decarli, R., et al. 2012, AJ, 143, 142

Müller-Sánchez, F., Prieto, M. A., Hicks, E. K. S., et al. 2011, ApJ, 739, 69

Nandra, K., & Pounds, K. A. 1994, MNRAS, 268, 405

Narayan, R. 2005, Ap&SS, 300, 177

Narayan, R., & Yi, I. 1994, ApJL, 428, L13

Nenkova, M., Sirocky, M. M., Ivezić, Ž., & Elitzur, M. 2008a, ApJ, 685, 147

Nenkova, M., Sirocky, M. M., Nikutta, R., Ivezić, Ž., & Elitzur, M. 2008b, ApJ, 685, 160

Netzer, H. 2006, Active Galactic Nuclei: Basic Physics and Main Components, ed. D. Alloin, Vol. 693, 1

Nicastro, F., Martocchia, A., & Matt, G. 2003, ApJL, 589, L13

Osterbrock, D. E. 1977, ApJ, 215, 733

Osterbrock, D. E., & Koski, A. T. 1976, MNRAS, 176, 61P

Paczyńsky, B., & Wiita, P. J. 1980, A&A, 500, 203

Peng, C. Y., Ho, L. C., Impey, C. D., & Rix, H.-W. 2002, AJ, 124, 266

Peterson, B. M. 1993, PASP, 105, 247

Peterson, B. M. 1997, An Introduction to Active Galactic Nuclei

Peterson, B. M. 2006, The Broad-Line Region in Active Galactic Nuclei, ed. D. Alloin, Vol. 693, 77

Peterson, B. M., Balonek, T. J., Barker, E. S., et al. 1991, ApJ, 368, 119

Pier, E. A., & Krolik, J. H. 1992, ApJ, 401, 99

Pier, E. A., & Krolik, J. H. 1993, ApJ, 418, 673

Planck Collaboration, Ade, P. A. R., Aghanim, N., et al. 2016, A&A, 594, A13

Pooley, D., Blackburne, J. A., Rappaport, S., & Schechter, P. L. 2007, ApJ, 661, 19

Pooley, D., Blackburne, J. A., Rappaport, S., Schechter, P. L., & Fong, W.-f. 2006, ApJ, 648, 67

Popović, L. Č., Mediavilla, E., Bon, E., & Ilić, D. 2004, A&A, 423, 909

Pott, J.-U., Malkan, M. A., Elitzur, M., et al. 2010, ApJ, 715, 736

Pozo Nuñez, F., Chelouche, D., Kaspi, S., & Niv, S. 2017, PASP, 129, 094101

Pozo Nuñez, F., Haas, M., Chini, R., et al. 2014, A&A, 561, L8

Pozo Nuñez, F., Gianniotis, N., Blex, J., et al. 2019, MNRAS, 490, 3936

Press, W. H., Rybicki, G. B., & Hewitt, J. N. 1992, ApJ, 385, 404

Ramos Almeida, C., & Ricci, C. 2017, Nature Astronomy, 1, 679

Ramos Almeida, C., Levenson, N. A., Alonso-Herrero, A., et al. 2011, ApJ, 731, 92

Rayner, J. T., Toomey, D. W., Onaka, P. M., et al. 2003, PASP, 115, 362

Ricci, C., Bauer, F. E., Arevalo, P., et al. 2016, ApJ, 820, 5

Riffel, R., Rodríguez-Ardila, A., & Pastoriza, M. G. 2006, A&A, 457, 61

Rowan-Robinson, M. 1977, ApJ, 213, 635

Ruff, A. J., Floyd, D. J. E., Webster, R. L., Korista, K. T., & Landt, H. 2012, ApJ, 754, 18

Rybicki, G. B., & Press, W. H. 1992, ApJ, 398, 169

Salpeter, E. E. 1964, ApJ, 140, 796

Salpeter, E. E. 1977, ARA&A, 15, 267

Schartmann, M., Burkert, A., Krause, M., et al. 2010, MNRAS, 403, 1801

Schartmann, M., Meisenheimer, K., Camenzind, M., Wolf, S., & Henning, T. 2005, A&A, 437, 861

Schartmann, M., Meisenheimer, K., Camenzind, M., et al. 2008, A&A, 482, 67

Schlafly, E. F., & Finkbeiner, D. P. 2011, ApJ, 737, 103

Schlegel, D. J., Finkbeiner, D. P., & Davis, M. 1998, ApJ, 500, 525

Schmidt, M. 1963, Nature, 197, 1040

Schnülle, K. 2017, PhD thesis, International Max Planck Research School for Astronomy and Cosmic Physics at the University of Heidelberg

Schnülle, K., Pott, J.-U., Rix, H.-W., et al. 2013, A&A, 557, L13

Schnülle, K., Pott, J.-U., Rix, H.-W., et al. 2015, A&A, 578, A57

Seyfert, C. K. 1943, ApJ, 97, 28

Shakura, N. I., & Sunyaev, R. A. 1973, A&A, 500, 33

Shapovalova, A. I., Popović, L. Č., Burenkov, A. N., et al. 2010, A&A, 509, A106

Shapovalova, A. I., Popović, L. Č., Collin, S., et al. 2008, A&A, 486, 99

Siebenmorgen, R., Heymann, F., & Efstathiou, A. 2015, A&A, 583, A120

Sikora, M., Stawarz, Ł., & Lasota, J.-P. 2007, ApJ, 658, 815

Skrutskie, M. F., Cutri, R. M., Stiening, R., et al. 2006, AJ, 131, 1163

Smith, E. P., Heckman, T. M., Bothun, G. D., Romanishin, W., & Balick, B. 1986, ApJ, 306, 64

Stalevski, M., Fritz, J., Baes, M., Nakos, T., & Popović, L. Č. 2012, MNRAS, 420, 2756

Stern, J., Hennawi, J. F., & Pott, J.-U. 2015, ApJ, 804, 57

Storchi-Bergmann, T., Mulchaey, J. S., & Wilson, A. S. 1992, ApJL, 395, L73

Suganuma, M., Yoshii, Y., Kobayashi, Y., et al. 2006, ApJ, 639, 46

Sulentic, J. W., Marziani, P., & Dultzin-Hacyan, D. 2000, ARA&A, 38, 521

Swain, M., Vasisht, G., Akeson, R., et al. 2003, ApJL, 596, L163

Ter Braak, C. J. F. 2006, Statistics and Computing, 16, 239

Tombesi, F., Cappi, M., Reeves, J. N., et al. 2010, A&A, 521, A57

Tran, H. D. 2001, ApJL, 554, L19

Tristram, K. R. W., Burtscher, L., Jaffe, W., et al. 2014, A&A, 563, A82

Tristram, K. R. W., Meisenheimer, K., Jaffe, W., et al. 2007, A&A, 474, 837

Urry, C. M., & Padovani, P. 1995, PASP, 107, 803

Vacca, W. D., Cushing, M. C., & Rayner, J. T. 2003, PASP, 115, 389

Veilleux, S., Goodrich, R. W., & Hill, G. J. 1997, ApJ, 477, 631

Véron-Cetty, M. P., & Véron, P. 2010, A&A, 518, A10

Wada, K. 2012, ApJ, 758, 66

Wada, K., & Norman, C. A. 2002, ApJL, 566, L21

Wada, K., Schartmann, M., & Meijerink, R. 2016, ApJL, 828, L19

Wanders, I., Peterson, B. M., Alloin, D., et al. 1997, ApJS, 113, 69

Watson, D., Denney, K. D., Vestergaard, M., & Davis, T. M. 2011, ApJL, 740, L49

Weigelt, G., Hofmann, K. H., Kishimoto, M., et al. 2012, A&A, 541, L9

Wildy, C., Landt, H., Goad, M. R., Ward, M., & Collinson, J. S. 2016, MNRAS, 461, 2085

Williams, M. J., Bureau, M., & Cappellari, M. 2010, MNRAS, 409, 1330

Wilson, A. S., & Colbert, E. J. M. 1995, ApJ, 438, 62

Wolf, C., Bian, F., Onken, C. A., et al. 2018, PASA, 35, e024

Zel'dovich, Y. B. 1964, Soviet Physics Doklady, 9, 195

Acknowledgements

I am very thankful to Jörg-Uwe for providing me with the opportunity to do my PhD at MPIA. The many fruitful and nice discussions and the support, whenever I needed it, were very enjoyable and helped me through all parts of the work involved in this thesis.

I would like to thank Hans-Walter Rix and Jochen Heidt, who agreed to referee my thesis. Furthermore I am grateful that Christian Fendt and Björn Malte Schäfer agreed to be part of my PhD committee.

I cannot thank Kirsten enough for explaining and easing the way into the painful reduction of the GROND data. Thank you for your patience and the groundwork you did for this thesis.

Thank you Hermine, for so much helpful feedback throughout this project.

A huge thank you also goes to the observers at the MPG 2.2m telescopes at La Silla responsible for many hours of GROND observations.

Thanks you Christina and Felix for proof reading parts of the thesis.

I am happy I was able to meet so many new friends at MPIA making the 4.5 years very enjoyable. Especially Christina, Sven and Tobi for extremely enjoyable lunch breaks and so many other fantastic experience. You were missed the last few month.

Danke an meine Schwiegereltern Jutta und Peter, dass ihr uns so viel unterstützt und so viel auf Paula aufgepasst habt. Ohne euch wäre die Zeit zum Schreiben dieser Arbeit deutlich knapper geworden. Ich bin unendlich froh, dass sich Paula so wohl fühlt bei euch!

Mama und Papa, danke, dass ihr mich immer in jedweder Form unterstützt habt und immer hinter mir gestanden habt. Ohne euch wäre mir so vieles nicht möglich gewesen. Danke, dass ihr mir immer erlaubt und ermöglicht habt, meine Ziele zu erreichen oder zumindest zu verfolgen.

Zuletzt noch Laura und Paula: Danke, dass ihr immer für mich da seid, mir immer ermöglicht jeden Stress zu vergessen und diesen sogar in ein Lächeln verwandelt. Danke, für eure Geduld mit mir und eure uneingeschränkte Unterstützung. Ich freue mich unendlich euch in meinem Leben zu haben.

Statement

This thesis is my own work and I have only used the sources indicated. Where the work of others has been quoted or reproduced, the source is always given.

Heidelberg, March 9, 2020 ....